Investigations on the Preparation of Highly Efficient Ti-, Mo-, and Cr-Oxide Based Photocatalysts and Their Photocatalytic Reactivities

Investigations on the Preparation of Highly Efficient Ti-, Mo-, and Cr-Oxide Based Photocatalysts and Their Photocatalytic Reactivities

（高効率な Ti-, Mo-, Cr- 酸化物系光触媒の調製と

光触媒反応性に関する研究）

Tae-Ho KIM

金　兌鎬

February 2010

Doctoral Thesis at Osaka Prefecture University

Contents

Chapter 1

General Introduction

In recent years, global environmental pollution and the lack of natural energy resources have become urgent problems which hinder sustainable development and amenable living space for future generations. The development of industries and cont emporary lifestyles have all led to accelerated energy consumption and the discharge of toxic agents into the air and water, leading to averse effects such as pollution-related diseases and global warming. In this regard, the design of new catalysts and catalytic processes are the focus of much attention as promising and effective chemical technologies that are totally clean, safe and efficient, and thus, environmentally-harmonious. Among such new advances and materials, the utilization of photocatalysis in many chemical processes is of special interest since it can be applied for the removal of toxic agents in air and water using clean and abundant solar energy so that photocatalytic technologies are now considered especially promising [1-5].

Since the photosplitting of water into H_2 and O_2 using an electrochemical cell consisting of a Pt electrode and TiO_2 electrode was first reported by Honda and Fujishima in 1972 [6], a large number of applications using various semiconductor materials in photocatalytic technology have been investigated for their potential in the conversion of light energy into useful chemical energy [7-13]. Under UV light irradiation, electrons can be excited from the valence band of the semiconductor catalysts to the conduction band, leaving photo-generated holes in the valence band, as shown in Fig. 1.1. These photo-generated electrons and holes play an important role in the photocatalytic degradation of pollutants. Photocatalytic reactions proceed under mild conditions at room temperature, normal atmospheric pressure and under light irradiation, making photocatalysis a much-desired ecologically clean chemical process for the removal of pollutants in our environment.

In such photocatalytic reactions, TiO_2 photocatalysts are widely used since TiO_2 semiconducting materials show good catalytic properties, high stability, high reactivity,

non-toxicity, are cost-efficient and environmentally-harmonious. In fact, TiO_2 photocatalysts are presently the most actively and widely investigated for applications that can effectively address environmental pollution [14-18]. However, TiO_2 photocatalysts operate only under UV light of wavelengths shorter than 400 nm which means only 3–5 % of the solar light that reaches the earth can be utilized. Recently, many studies have been devoted to the modification of TiO_2 photocatalysts by the substitutional doping of metals or nonmetals in order to extend their absorption edge into the visible light region and to improve their photocatalytic activity [19-24]. Although metal ions chemically doped into TiO_2 can induce visible light response, most of these catalysts do not show long-term stability nor have sufficiently high reactivity for a wide range of applications. When metal ions or oxides are incorporated into the TiO_2 by a chemical doping method, impurity energy levels in the band gap of TiO_2 are formed and may cause an increase in the recombination between the photogenerated electrons and holes [20].

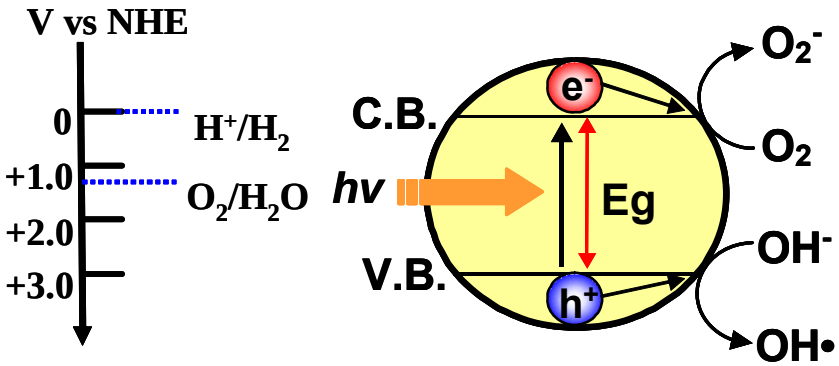

Figure 1.1. Processes of photocatalysis on semiconductor particles.

This thesis deals with the application of a radio frequency magnetron sputtering (RF-MS) deposition method for the development of visible light-responsive TiO_2 thin film photocatalysts [25-28]. Various spectroscopic analyses have revealed that a decrease in the O/Ti ratio from the surface (O/Ti = 2.00) to the bottom (O/Ti = 1.93)

may play a significant role in the modification of the electronic properties of these TiO_2 thin films, enabling them to absorb and operate under visible light irradiation [29].

In addition to the development of visible light-responsive TiO_2 photocatalysts, a unique photoelectrochemical circuit system (TE-SSC-PE) consisting of a rod-type TiO_2 electrode (TE), Pt counter electrode (PE) and silicon solar cell (SSC) was constructed. The effect of the external bias on the photocatalytic activity of this TE-SSC-PE system has been investigated in detail in order to achieve an efficient photocatalytic system for the oxidation of various kinds of toxic or odorous organic compounds.

Single-Site Photocatalysts

It has been reported that single-site photocatalysts constructed within zeolites or mesoporous silica materials show fascinating photocatalytic activity with high selectivity which cannot be realized on bulk semiconducting photocatalysts. In these catalytic systems, transition metal oxides (titanium oxide, vanadium oxide and chromium oxide) are considered to be highly dispersed at the atomic level as well-defined catalysts which exist in the specific structure of the zeolite or mesoporous silica framework [30-46]. Single-site photocatalysts can initiate the direct decomposition of NOx (NO, N_2O) into N_2 and O_2 [43,44], CO_2 reduction with H_2O into methanol [40,42] and the partial oxidation of hydrocarbons [40,46] with high efficiency and high selectivity. These unique reactivities are attributed to the ligand to metal charge transfer excited state of the isolated metal oxide species under UV-light irradiation (Fig. 1.2) [30]. The high reactivity of these ligand to metal charge transfer excited states or electron-hole pair states, which are localized in close proximity as compared to those in semiconductors, enables various photocatalytic reactions with a high efficiency that is not possible on bulk semiconductor photocatalysts. This thesis deals with the development of highly active and selective single-site photocatalysis using transition metal oxide-containing zeolites and mesoporous molecular sieves. Special attention

has been focused on the differences in the reaction dynamics as well as the reactivity between single-site photocatalysts and semi-conducting bulk photocatalysts in their photoexcited states.

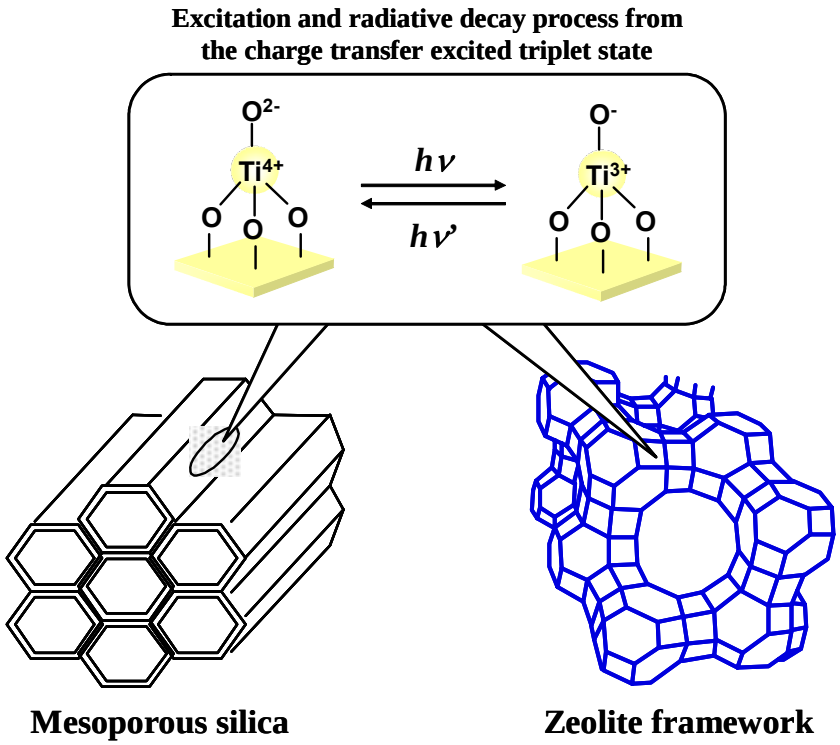

Figure 1.2. Single-site Ti-oxide photocatalysts

In addition to these transition metal oxide single-site photocatalysts, inorganic-organic hybrid mesoporous materials (HMM) incorporating organometalcarbonyl complexes within their silica frameworks have been developed. A simple chemical vapor deposition (CVD) treatment with various metal carbonyls ($M(CO)_6$ (M = Cr,Mo,W)) of phenylene-bridged hybrid mesoporous materials (HMM-ph) enabled the efficient incorporation of $phM(CO)_3$ complexes within their silica frameworks (HMM-$phM(CO)_3$). This work also deals with the thermal stability of HMM-$phM(CO)_3$ as well as their unique photocatalytic activity for the metathesis reaction of propylene to yield ethylene and butadiene [47].

Outline

This thesis details the research devoted to the preparation of highly active visible-light responsive semiconducting TiO_2 photocatalysts by a RF magnetron sputtering deposition method. The photocatalytic reactivity of these TiO_2 photocatalysts has been investigated by the oxidation of various organic compounds into CO_2 under UV and visible light irradiation. Furthermore, the unique photocatalytic oxidation of benzyl alcohol into benzaldehyde with high conversion and selectivity on TiO_2 photocatalysts under visible light irradiation is also discussed. To achieve an enhancement in the photocatalytic activity of these TiO_2 photocatalysts, photoelectrochemical circuit systems consisting of a rod-type TiO_2 electrode, Pt electrode and silicon solar cells have also been constructed and their activity for the decomposition of ethanethiol in water has been investigated.

The preparation of highly active zeolites and mesoporous materials containing highly dispersed isolated transition metal oxides species (Ti, Mo, Cr) or organometal carbonyl complexes as single-site photocatalysts by various preparation methods such as ion-exchange, hydrothermal synthesis, or CVD method is also introduced here. The application of these photocatalysts for highly selective reactions has been discussed. Special attention has been focused on the effect of the local structure of the active sites on the photocatalytic reactivity as well as on a clarification of the reaction mechanisms. Moreover, detailed and comprehensive characterizations of these photocatalysts have been undertaken by such spectroscopic techniques as UV-vis, XAFS, XRD, XPS, SEM, TPD, FT-IR, and photoluminescence analyses.

This thesis contains 6 chapters, the first being an overall introduction of the research objectives with outlines of the succeeding chapters summarized as follows:

Chapter 2

In this chapter, an RF magnetron sputtering deposition method has been applied for

the development of visible light-responsive TiO_2 thin films and their photocatalytic reactivity has been investigated. The visible light-responsive TiO_2 thin film and nanoparticles of Pt were deposited on the non-woven fabric of a Ti-metal substrate (Pt-Vis-TiO_2/N-Titanystar) by a radio-frequency magnetron sputtering deposition method. Pt-Vis-TiO_2/N-Titanystar was shown to oxidize various organic compounds into CO_2 as well as decompose ammonia gas into N_2 in the presence of O_2 even under visible light ($\lambda > 420$ nm) at 293 K. It was also found that methanol vapor was photocatalytically oxidized into CO_2 on Pt-Vis-TiO_2/N-Titanystar even under a flow system, while the oxidation rate of the methanol vapor into CO_2 varies greatly depending on the UV light intensity from the LED lamp ($\lambda = 375$ nm).

Chapter 3

In this chapter, a unique photoelectrochemical circuit system was constructed and its photocatalytic activity for the decomposition of ethanethiol in water was investigated. Chapter 3.1 focuses on the effect of the external bias as well as the calcination temperature of a rod-type TiO_2 electrode on the oxidation rate of ethanethiol. The rod-type TiO_2 electrodes were prepared by the calcination of a metal Ti rod at various temperatures. Spectroscopic investigations have revealed that a dense and thick stoichiometric TiO_2 layer was formed at 1073 K which shows the highest activity for the decomposition of ethanethiol. Photoelectrochemical circuit systems were constructed by connecting the rod-type TiO_2 electrode and rod-type Pt electrode through a silicon solar cell. The photoelectrochemical circuit system efficiently oxidized the ethanethiol in water into CO_2, while the reaction rate strongly depended on the calcination temperature of the rod-type TiO_2 electrode. Furthermore, it was found that a negative bias applied to the rod-type TiO_2 electrode by a silicon solar cell enhances the oxidation rate of the ethanethiol in water. Chapter 3.2 focuses on the effect of the various treatments of the rod-type TiO_2 electrode, such as calcination in NH_3 or in vacuum, on the photocatalytic activities. The calcination treatment in NH_3 at 773 K of

the rod-type electrode was particularly effective in increasing the photoelectrochemical performance and photocatalytic activity of the photoelectrochemical circuit system.

Chapter 4

In this chapter, the effects of the calcination temperature and HF treatment of TiO_2 on the reaction rate of the selective photocatalytic oxidation of benzylalchol were investigated. The selective photocatalytic oxidation of benzyl alcohol into benzaldehyde proceeded at high conversion and selectivity on a TiO_2 photocatalyst suspended in acetonitrile solution in the presence of O_2 under visible light irradiation. It was found that the photocatalytic activity for the formation of benzaldehyde decreases when the number of surface OH groups of TiO_2 decrease by calcination treatment at high temperature. It was also confirmed that the interaction of benzyl alcohol with both the coordinately unsaturated Ti sites and surface OH groups gives the unique surface complex, which shows an absorption band in the visible region. Visible light irradiation of the absorption band was found to induce a charge separation of the holes and electrons and initiate the selective photocatalytic reaction of benzyl alcohol into benzaldehyde.

Chapter 5

In this chapter, various zeolites or silicious mesoporous materials containing transition metal ions have been prepared by using various preparation methods and applied for highly selective photocatalytic reactions. Chapter 5.1 deals with the incorporation of transition metal oxides (Ti, Mo, Cr) within the framework of the zeolites and their high and unique photocatalytic reactivity as single-site heterogeneous catalysts for significant reactions such as the decomposition of NOx (NO, N_2O) and metathesis reaction of alkenes. In-situ spectroscopic investigations of these photofunctional systems by photoluminescence, XAFS (XANES and FT-EXAFS), ESR

and FT-IR revealed that the photo-excited states of the transition metal oxides play a vital role in realizing the photocatalytic reactions. The high photocatalytic efficiency and selectivity of these single-site catalysts for the reactions, which could not be observed with semiconducting bulk photocatalysts, were found to depend strongly on the unique reactivity of the photo-excited state of the single-site transition metal oxide species. Chapter 5.2 discusses the preparation of HMM-ph incorporating arenetricarbonyl complexes (HMM-ph$M(CO)_3$ (M=Cr, Mo, W)) by CVD treatment of HMM-ph with $M(CO)_6$. Various spectroscopic investigations have elucidated that the ph$M(CO)_3$ complexes within HMM-ph are thermally stable even under thermovacuum treatment at 473 K. The catalytic activity of HMM-ph$M(CO)_3$ for the metathesis reaction of propylene was also investigated in a gas phase reaction. It was found that UV light irradiation of HMM-ph$M(CO)_3$ in the presence of propylene induces the methathesis reaction of propylene to form ethane and butane even at 293 K.

Chapter 6

The results and conclusions obtained in the various investigations covered in this thesis have been summarized in this final chapter.

References

[1] M. Anpo, *Catal. Surveys. Jpn.*, **1**, 169 (1997).

[2] M. Anpo (Ed.), *Surface Photochemistry*, Wiley, London (1995).

[3] M. Anpo, H. Yamashita, In: M. Schiavello (Ed.), *Heterogeneous Photocatalysis*, Wiley, London (1997).

[4] M. Anpo, In: I. Okura, M. Kaneko (Eds.), *Photocatalysis*, Kodanshya Scientific Publishers, Tokyo (2002).

[5] M. Anpo, In: P. Tundo, P. Anatase (Eds.), *Green Chemistry*, Oxford University Press, **1** (2000).

[6] K. Honda, A. Fujishima, *Nature*, **286**, 37 (1972) ; *Bull. Chem. Soc. Jpn.*, **44**, 1148 (1971).

[7] T. Inoue, A. Fujishima, S. Konishi, K. Honda, *Nature*, **277**, 637 (1979).

[8] T. Kawai, T. Sakata, *Nature*, **286**, 31 (1980).

[9] S. Sato, J.M. White, *J. Am. Chem. Soc.*, **102**, 7206 (1980).

[10] A. Heller, A.A. Shalom, W.A. Bonner, B. Miller, *J. Am. Chem. Soc.*, **104**, 1688 (1982).

[11] M.A. Fox, *Acc. Chem. Res.*, **16**, 314 (1983).

[12] M.A. Fox, M.T. Dulay, *Chem. Rev.*, **93**, 341 (1993).

[13] M. Anpo, M. Takeuchi, H. Yamashita, S. Kishiguchi, In: V. Ramamurthy, K.S. Schanze (Ed.), *Molecular and Supramolecular Photochemistry: Semiconductor Photochemistry and Photophysics*, Dekker, New York, **10**, 283 (2003).

[14] M. R. Hoffmann, S. T. Martin, W. Choi, D. W. Bahnemann, *Chem. Rev*. **95**, 69 (1995).

[15] A. Heller, *Acc. Chem. Res*., **14**, 154 (1981).

[16] Y. Kubokawa, M. Anpo, K. Honda, K. Ito, in *Hikari-shokubai (Photocatalysis)*, Eds., Y. Kubokawa, K. Honda, Y. Saito, Asakura-shoten, Tokyo (1988).

[17] M. Anpo, Y. Kubokawa, *Res. Chem. Intermed*., **8**, 105 (1987).

[18] A. Fujishima, T. N. Rao, D. A. Tryk, *J. Photochem. Photobiol. C: Photochem. Rev.*, **1**, 1 (2000).

[19] E. Borgarello, J. Kiwi, M. Grätzel, E. Pelizzetti, M. Visca, *J. Am. Chem. Soc.,* **104**, 2996 (1982).

[20] W.Y. Choi, A. Termin, M. R. Hoffmann, *J. Phys. Chem.*, **98**, 13669 (1994).

[21] R. Asahi, T. Morikawa, T. Ohwaki, A. Aoki, Y. Taga, *Science*, **293**, 269 (2001).

[22] T. Umebayashi, T. Yamaki, H. Ito, K. Asai, *Appl. Phys. Lett.*, **81**, 454 (2002).

[23] H. Irie, Y. Watanabe, K. Hashimoto, *Chem. Lett.*, **32**, 772 (2003).

[24] T. Ohno, T. Tsubota, M. Toyofuku, R. Inaba, *Catal. Lett.*, **98**, 255 (2004).

[25] M. Takeuchi, M. Anpo, T. Hirao, N. Itoh, N. Iwamoto, *Surf. Sci. Jpn.,* **22**, 561 (2001).

[26] M. Kitano, M. Takeuchi, M. Matsuoka, J.M. Thomas, M. Anpo, *Chem. Lett.*, **34**, 616 (2005).

[27] M. Matsuoka, M. Kitano, M. Takeuchi, M. Anpo, J.M. Thomas, *Top. Catal.*, **35**, 305 (2005).

[28] H. Kikuchi, M. Kitano, M. Takeuchi, M. Matsuoka, M. Anpo, P.V. Kamat, *J. Phys. Chem. B*, **110**, 5537 (2006).

[29] M. Matsuoka, M. Kitano, M. Takeuchi, M. Anpo, J.M. Thomas, *Top. Catal.*, **35**, 305 (2005).

[30] M. Anpo, M. Che. *Adv. Catal.* **44**, 119 (1999).

[31] M. Anpo, J.M. Thomas. *Chem. Commun.*, 3273 (2006).

[32] H. Yamashita, M. Anpo, *Curr. Opin. Solid State Mater. Sci.*, **7**, 471 (2004).

[33] H. Yamashita, Y. Miura, K. Mori, S. Shironita, Y. Masui, N. Miura, T. Ohmichi, T. Sakata, H. Mori, *Pure Appl. Chem.*, **79**, 11, 2095 (2007).

[34] H. Yamashita, K. Mori, *Chem. Lett.*, **36**, 348 (2007).

[35] M. Anpo, M. Kondo, Y. Kubokawa, C. Louis, M. Che, *J. Chem. Soc. Faraday Trans.*, 84, 2771 (1988).

[36] M. Anpo, M. Kondo, S. Coluccia, C. Louis, M. Che, *J. Am. Chem. Soc.*, **111**, 8791 (1989).

[37] M. Anpo, I. Tanahashi, Y. Kubokawa, *J. Phys. Chem.*, **84**, 3440 (1980).

[38] A.M. Gritscov, V.A. Shvets, V.B. Kazansky, *Chem. Phys. Lett.*, **35**, 511 (1975).

[39] J.M. Thomas, G. Sanker, *Acc. Chem. Res.*, **34**, 571 (2001).

[40] K. Ikeue, H. Yamashita, M. Anpo, T. Takewaki, *J. Phys. Chem. B*, **105**, 8250 (2001).

[41] Y. Hu, S. Higashimoto, S. Takenaka, Y. Nagai, *Catal. Lett.*, **100**, 35 (2005).

[42] H. Yamashita, Y. Fujii, Y. Ichihashi, S.G. Zhang, K. Ikeue, D.R. Park, K. Koyama, T. Tatsumi, M. Anpo, *Catal. Today*, **45**, 221 (1998).

[43] H. Yamashita, Y. Ichihashi, M. Anpo, M. Hashimoto, C. Louis, M. Che, *J. Phys. Chem.*, **100**, 16041 (1996).

[44] J. Zhang, M. Minagawa, T. Ayusawa, S. Natarajan, H. Yamashita, M. Matsuoka, M. Anpo, *J. Phys. Chem. B*, **104**, 11501 (2000).

[45] A. Corma, *Chem. Rev.*, **97**, 2373 (1997).

[46] F. Amano, T. Yamaguchi, T. Tanaka, *J. Phys. Chem. B*, **110**, 281 (2006).

[47] A. Korda, R. Giezynski, S. Krycinski, *J. Mol Catal.*, **9**, 51 (1980).

Chapter 2

Preparation of Visible Light-Responsive TiO_2 Thin Films by an RF Magnetron Sputtering Deposition Method and Their Photocatalytic Reactivity

2.1. Introduction

Recently, various TiO_2 photocatalysts have been applied for various reactions such as the purification of water, air and soil polluted with organic compounds [1,2,4] as well as the photocatalytic decomposition of water into H_2 and O_2 [3]. However, TiO_2 photocatalysts operate only under UV light irradiation of wavelengths shorter than 400 nm and utilize only 3-4 % of solar beams that reach the earth. It is, therefore, necessary to develop a photocatalytic system which can work even under visible light irradiation [5]. Many studies have been devoted to the modification of TiO_2 photocatalysts by the substitutional doping of metals or nonmetals in order to extend their absorption edge into the visible light region and improve their photocatalytic efficiency [6-8]. We have previously reported that a radio-frequency magnetron sputtering (RF-MS) deposition method in pure Ar gas atmosphere using a TiO_2 target enables the preparation of a visible light-responsive TiO_2 (Vis-TiO_2) thin film by precise control of the substrate temperature during the deposition process [9-11].

In the present work, Vis-TiO_2 thin film have been deposited on two different kinds of anodized Ti-metal substrates, i. e., plate-type Titanystar (P-Titanystar) or non-woven fabric Titanystar (N-Titanystar), by a RF-MS deposition method. These two kinds of Vis-TiO_2 thin film photocatalysts (Vis-TiO_2/P-Titanystar and Vis-TiO_2/N-Titanystar) were then applied for the oxidation of various organic compounds in the gas phase or in water under UV or visible light irradiation. Special attention was focused on how the photocatalytic activity of the Vis-TiO_2 thin film photocatalysts is affected by the kinds of substrates as well as the Pt deposition. Moreover, we have evaluated the photocatalytic activity of Pt-loaded Vis-TiO_2/N-Titanystar (Pt-Vis-TiO_2/N-Titanystar) for the oxidation of methanol gas in a flow system under UV light irradiation from a LED lamp (80 W).

2.2. Experimental

Two kinds of Titanystar (Yield CO., Kyoto, Japan) were prepared by the anodization treatment (100 V for 1500 s) of a plate-type Ti-metal (P-Ti) in an electrolyte containing an mixture of organic acids and the non-woven fabric of Ti-metal (N-Ti) in an electrolyte containing an mixture of organic acids followed by calcination at 773 K for 1 h in air, and these were denoted as P-Titanystar and N-Titanystar, respectively.

After anodization and calcination treatment, the top surfaces of P-Ti and N-Ti were oxidized into TiO_2. The TiO_2 thin films were then deposited on various substrates by a radio-frequency magnetron sputtering (RF-MS) deposition method using a TiO_2 plate (High Purity Chemicals Lab., Corp., Grade: 99.99 %) as the source material and Ar gas (99.995 %) as the sputtering gas. Prior to the introduction of Ar gas, the chamber was evacuated to less than 5.0×10^{-4} Pa, followed by the introduction of Ar at 2.0 Pa. Visible light-responsive TiO_2 (Vis-TiO_2) thin films were then deposited on three kinds of substrates (P-Titanystar, N-Titanystar, N-Ti; 50 x 50 mm^2) by inducing a radio-frequency power of 300 W with the substrate temperature (Ts) held at 873 K. The Vis-TiO_2 thin film photocatalysts were denoted as Vis-TiO_2/P-Titanystar, Vis-TiO_2/N-Titanystar and Vis-TiO_2/N-Ti. Nanoparticles of Pt were deposited on Vis-TiO_2/N-Titanystar by a RF-MS method using a Pt plate as the source material with an RF power of 70 W at Ts = 298 K and this thin film photocatalyst was denoted as Pt-Vis-TiO_2/N-Titanystar. The crystal structures of the Vis-TiO_2 thin film photocatalysts were determined by X-ray diffraction (XRD: Shimadzu, XRD-6100) analysis using a CuKα line (λ = 1.5406 Å). The photocatalytic activities of the Vis-TiO_2 thin film photocatalysts were investigated by the oxidation of 2-propanol in water under UV light irradiation at 293 K. The concentration of an aqueous solution of 2-propanol was adjusted to 6.5×10^{-3} mol/L. The various Vis-TiO_2 thin film photocatalysts were placed in a quartz glass cell with an aqueous solution of 2-propanol (10 ml). UV irradiation was carried out with a full arc from a 500 W high pressure Hg lamp. The

reaction products were analyzed by a gas chromatograph (GC-14A, Shimazu).

The flow reactor for the photocatalytic oxidation of methanol vapor was constructed by an aluminium frame (150 mm(W) X 200 mm(D) X 5 mm(H)) equipped with a quartz glass window (150 mm(W) X 200 mm(D), 2 mm thickness) where 12 sheets of Pt-Vis-TiO_2/N-Titanystar were placed. He-balanced methanol (CH_3OH (1000 ppm)/He) was used for the reactant gas. The photocatalytic oxidation reactions of methanol vapor was performed by using a flow reactor under light irradiation from a LED lamp (80 W, 375 nm) at 298 K with various light intensities (5, 10, 20 mW/cm^2). The light intensity was varied by changing the distance between the LED lamp and flow reactor. The flow rates of He-balanced methanol (CH_3OH (1000 ppm)/He) and O_2 (99.99 %) introduced into the reactor were adjusted to 25 and 5 ml/min, respectively. The reaction products were analyzed by gas chromatography (Shimadzu GC-14B) with a Porapak-Q packed column. Photocatalytic oxidation reactions of various organic compounds in the gas phase with O_2 were carried out in a closed system using a quartz reactor under visible light irradiation ($\lambda > 420$ nm) at 293 K. The gas pressure of the reactant gas and O_2 were both adjusted to 1013.25 Pa. The reaction products were analyzed by gas chromatography (Shimadzu GC-7A) with a Porapak-Q packed column.

2.3. Results and Discussion

Figure 2.1 shows the activities of the various Vis-TiO_2 thin film photocatalysts for the oxidation of 2-propanol in water under UV light irradiation at 293 K. First, the photocatalytic activity was compared for these three kinds of Vis-TiO_2 thin film photocatalysts (Vis-TiO_2/P-Titanystar, Vis-TiO_2/N-Ti and Vis-TiO_2/N-Titanystar). Vis-TiO_2/N-Titanystar was observed to show higher activity than Vis-TiO_2/P-Titanystar.

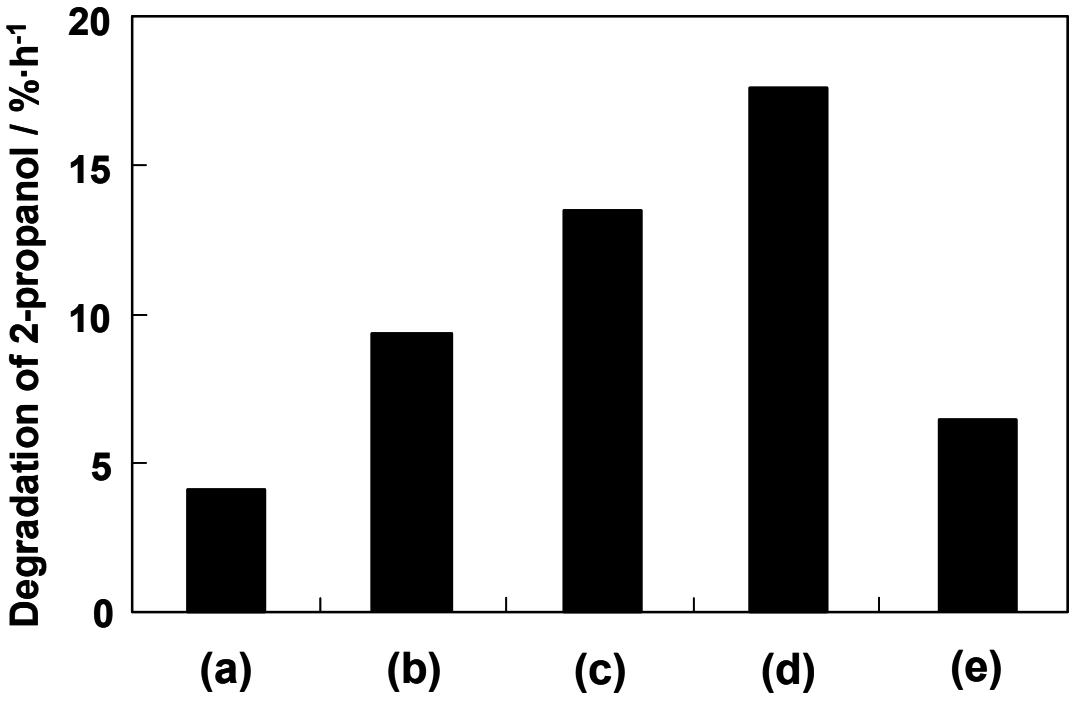

Figure 2.1. Photocatalytic oxidation of 2-propanol in water under UV light irradiation on: (a) Vis-TiO_2/P-Titanystar, (b) Vis-TiO_2/N-Ti, (c) Vis-TiO_2/N-Titanystar, (d) Pt-Vis-TiO_2/N-Titanystar, and (e) N-Titanystar at 293 K.

The high activity of Vis-TiO_2/N-Titanystar can be attributed to the higher active surface area of N-Titanystar (non-woven fabric type) than that of P-Titanystar (plate type), showing the advantage of N-Titanystar as the substrate against P-Titanystar. Furthermore, Vis-TiO_2/N-Titanystar showed higher photocatalytic activity than Vis-TiO_2/N-Ti, indicating that the anodization of N-Ti (non-woven fabric of Ti-metal) to produce the surface TiO_2 layer is indispensable in realizing Vis-TiO_2 thin film photocatalysts with high activity and performance. It should be noted that N-Titanystar as a substrate (without the deposition of the Vis-TiO_2 thin film) shows lower activity than Vis-TiO_2/N-Titanystar, showing that the deposition of Vis-TiO_2 on N-Titanystar is essential in preparing a highly active photocatalyst. It was also found that the photocatalytic activity of Vis-TiO_2/N-Titanystar was remarkably enhanced by the deposition of Pt on the surface of Vis-TiO_2/N-Titanystar (Pt-Vis-TiO_2/N-Titanystar). This enhancement of the photocatalytic activity was considered to be caused by the increase in the efficiency of the charge-separation resulting from the electron transfer from the Vis-TiO_2 thin film to the deposited Pt particles [12]. These results clearly indicate that deposition of both Pt particles and Vis-TiO_2 on N-Titanystar by the RF-MS deposition method is an effective way to prepare highly active TiO_2 photocatalysts.

Figure 2.2 shows the XRD patterns of N-Titanystar and Pt-Vis-TiO_2/N-Titanystar prepared by the RF-MS method. N-Titanystar shows typical diffraction peaks due to the Ti metal substrate (2θ = 35.0, 38.7, 40.2, 53.0) while exhibiting no diffraction peaks due to the TiO_2 phase, showing that the TiO_2 layer formed on the top surface of N-Ti (non-woven fabric of Ti-metal) by anodization treatment is too thin to be detected by XRD measurement. On the other hand, Pt-Vis-TiO_2/N-Titanystar exhibited diffraction peaks due to the rutile phase of TiO_2 (2θ = 27.4, 44.3, 54.4, 56.9), while the intensities of the diffraction peaks due to the Ti metal substrate were remarkably decreased. These results clearly suggest that the surface of N-Titanystar is covered by a Vis-TiO_2 layer having a rutile TiO_2 phase.

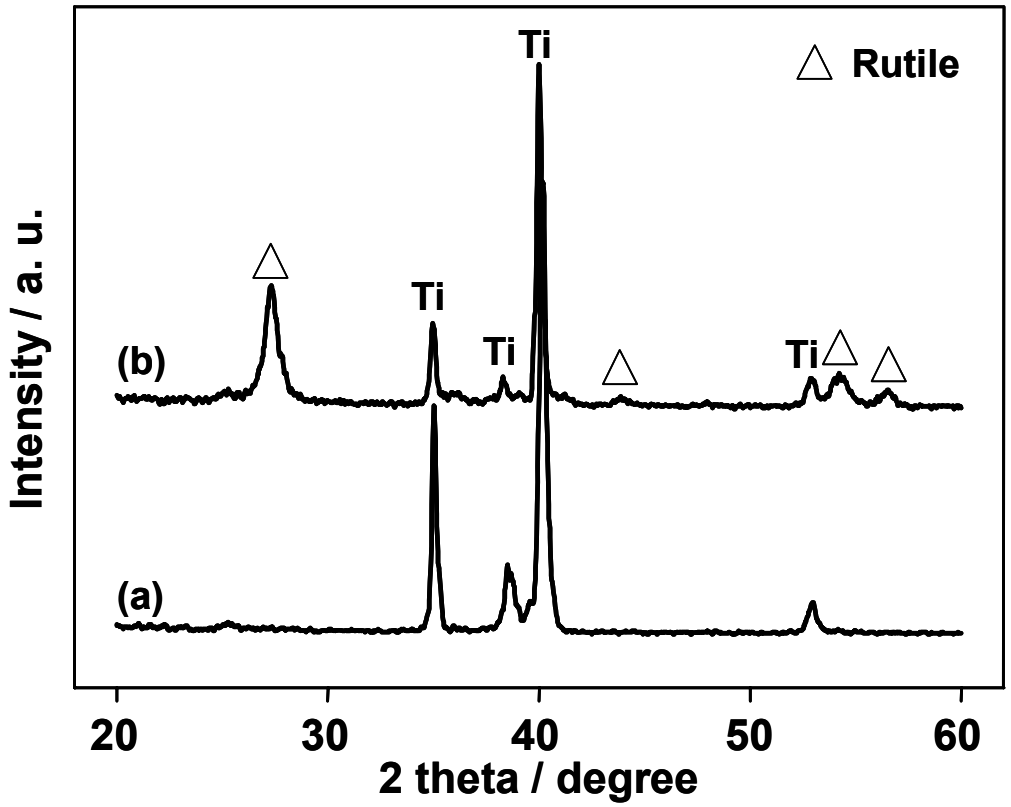

Figure 2.2. XRD patterns of (a) N-Titanystar and (b) Pt-Vis-TiO_2/N-Titanystar.

The photoctalytic oxidation of methanol vapor was then investigated on Pt-Vis-TiO_2/N-Titanystar using a flow reactor, as shown in Fig. 2.3. The flow reactor was constructed by an aluminium frame equipped with a quartz glass window where 12 sheets of Pt-Vis-TiO_2/N-Titanystar were placed. A mixture of He-balanced methanol (CH_3OH/He) and O_2 was introduced from one side of the flow reactor at atmospheric pressure, while the outlet of the reactor on the other side was connected to a gas chromatographer where the outlet concentrations of methanol and CO_2 were monitored. Figure 2.4 shows the effect of the light intensity on the reaction time profiles of the photocatalytic oxidation of methanol on Pt-Vis-TiO_2/N-Titanystar. Independent of the light intensity, the concentration of methanol vapor decreased to around 1/4 – 1/2 of its initial concentration under UV light irradiation, while the concentration gradually increased to its initial level after UV light was discontinued. These results suggest that Pt-Vis-TiO_2/N-Titanystar is an effective photocatalyst in reducing the vapor pressure of methanol under LED light irradiation even under flow conditions. In the case of a UV light intensity of 20 mW/cm^2, CO_2 evolution as a reaction product can be observed immediately after UV light is turned on and its evolution was continuously observed under UV light irradiation. These results clearly show that methanol vapor is photocatalytically oxidized into CO_2. However, the concentration of the CO_2 evolved under UV irradiation decreases with a decrease in the UV light intensity and CO_2 evolution was not observed in the gas phase in the case of a UV light intensity of 5 mW/cm^2. These results suggest that partially oxidized products of methanol such as formaldehyde and formic acid were accumulated on the surface of Pt-Vis-TiO_2/N-Titanystar under the reaction conditions of low UV light intensity.

Finally, the visible light response of Pt-Vis-TiO_2/N-Titanystar was investigated by the oxidation reaction of organic compounds in the gas phase under visible light irradiation (λ > 420 nm) at 293 K. Figure 2.5 shows the CO_2 yields in the photocatalytic oxidation of various organic compounds in the gas phase with O_2.

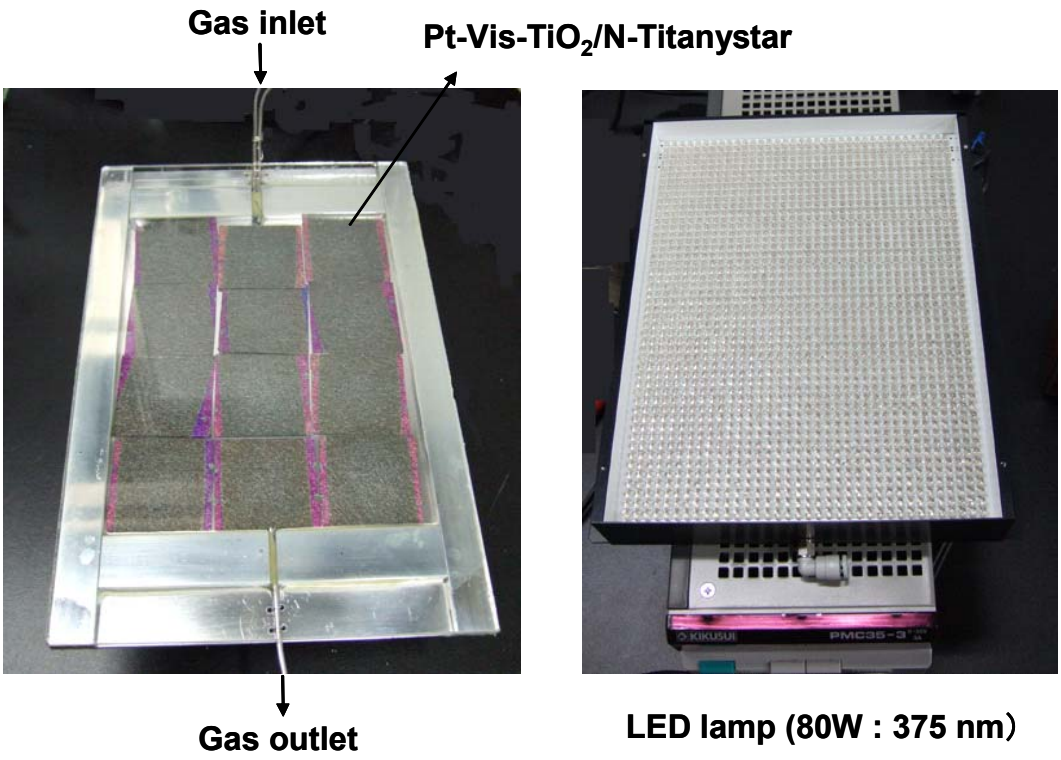

Figure 2.3. Flow reactor for the photocatalytic oxidation of methanol vapor on Pt-Vis-TiO_2/N-Titanystar

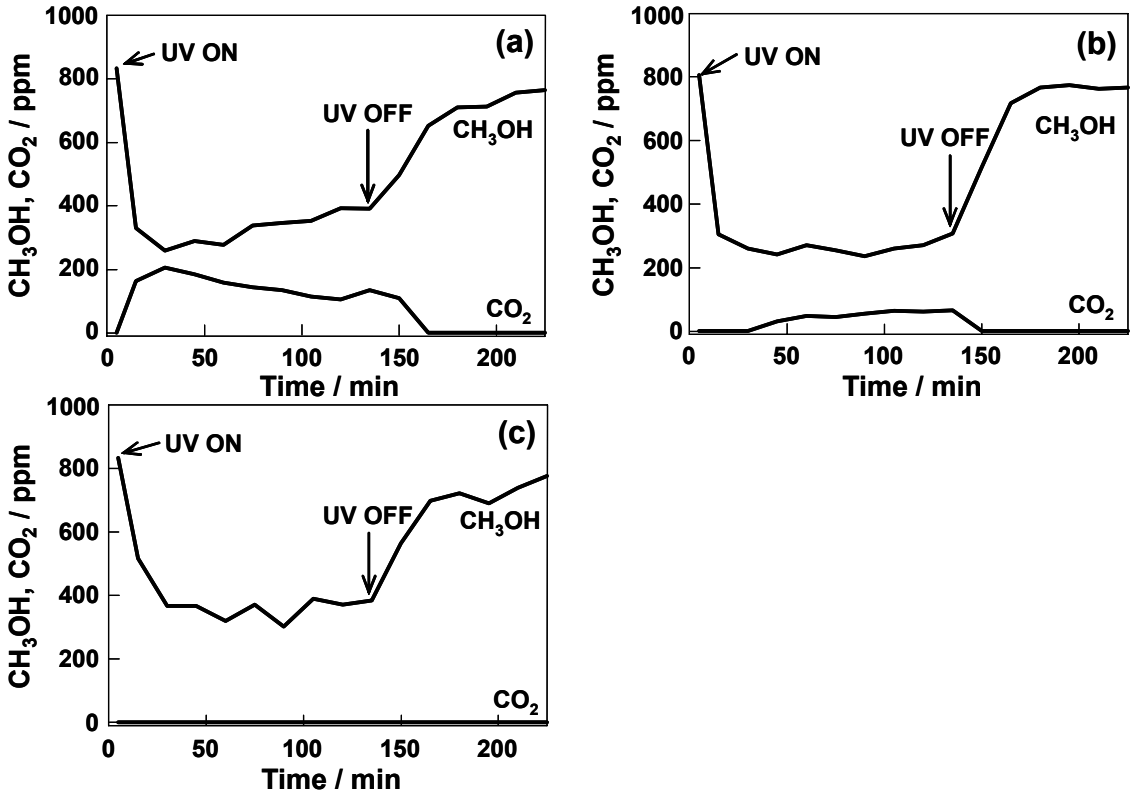

Figure 2.4. Effect of the light intensity on the reaction time profiles of the photocatalytic oxidation of methanol vapor on Pt -Vis-TiO_2/N-Titanystar under UV light irradiation.

Light source: LED lamp (80 W, 375 nm)

Intensity of radiation (mW/cm^2): (a) 20, (b) 10, (c) 5

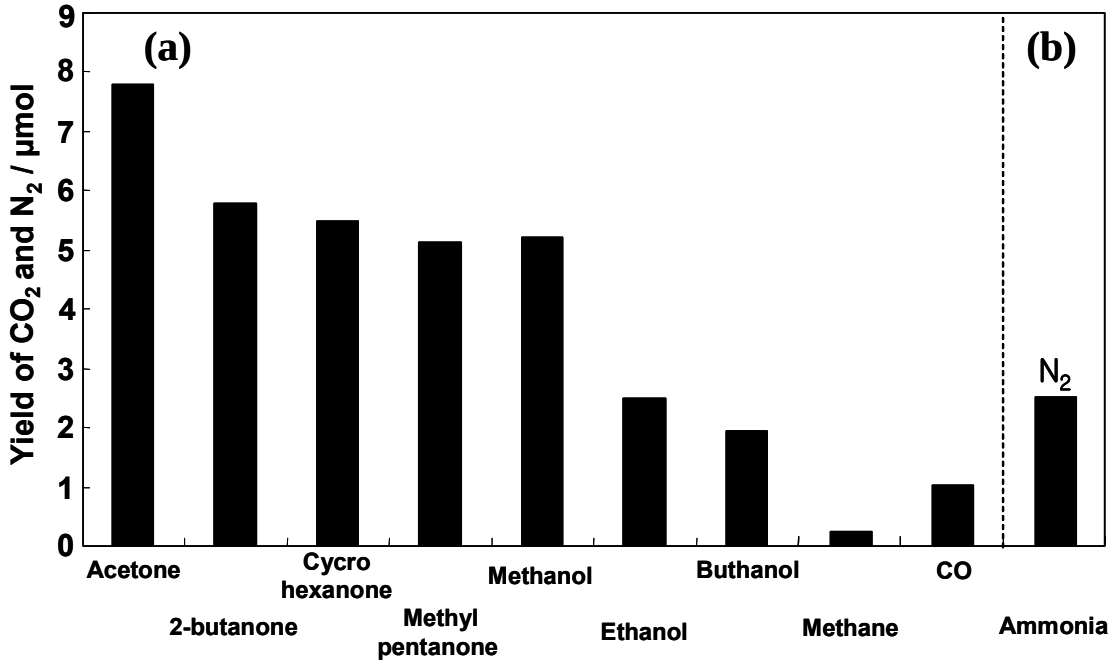

Figure 2.5. (a) Yields of CO_2 in the oxidation of various organic compounds in the gas phase, and (b) yield of N_2 in the oxidation of ammonia in the gas phase on Pt-Vis-TiO_2/N-Titanystar (1 cm x 1 cm) under visible light irradiation (λ > 420 nm, 80mW/cm^2).

Reaction time: 12 hrs

Light source: Xenon lamp with L-420 cut filter (HOYA)

Reactant: 1013.25 Pa, O_2: 1013.25 Pa

All of the organic compounds in the gas phase could be oxidized into CO_2 and the highest CO_2 formation rate was observed with acetone. The yields of CO_2 greatly depended on the kinds of organic compounds while it is clear that Pt-Vis-TiO_2/N-Titanystar can oxidize various organic compounds into CO_2 even under visible light irradiation ($\lambda > 420$ nm) at 293 K. Moreover, ammonia was found to oxidize to yield N_2 as a reaction product on Pt-Vis-TiO_2/N-Titanystar even under visible light irradiation ($\lambda > 420$ nm). The main origins of the visible light activity of the Vis-TiO_2 thin film photocatalysts can be ascribed to the Vis-TiO_2 deposited onto the various substrates since the O/Ti ratio of the Vis-TiO_2 thin films gradually decrease from the top surface (O/Ti ratio of 2.00) to the inside bulk (O/Ti ratio of 1.93). Such an anisotropic morphology of the Vis-TiO_2 thin film may modify the electronic properties of the thin films, leading to changes in the band gap energy [13-18]. Thus, it was elucidated that Pt-Vis-TiO_2/N-Titanystar can be applied for the elimination of harmful organic compounds in the gas phase even under visible light irradiation ($\lambda > 420$ nm) at 293 K.

2.4. Conclusions

Vis-TiO_2 thin film photocatalyst were deposited on various kinds of substrates (P-Titanystar, Ti-N and N-Titanystar) by a RF magnetron sputtering deposition method at a substrate temperature of 873 K and their photocatalytic activity was investigated. The Vis-TiO_2 thin film photocatalyst deposited on various substrates were observed to efficiently oxidize 2-propanol in water under UV light irradiation while the highest activity was observed for Vis-TiO_2/N-Titanystar. It was also found that Pt-Vis-TiO_2/N-Titanystar shows higher activity for the oxidation of 2-propanol in water than Vis-TiO_2/N-Titanystar. The photoctalytic oxidation of methanol vapor was then investigated on Pt-Vis-TiO_2/N-Titanystar using a flow reactor. Results show that methanol vapor is photocatalytically oxidized into CO_2 on Pt-Vis-TiO_2/N-Titanystar even in a flow system, while the oxidation rate of methanol vapor into CO_2 varied

greatly depending on the UV light intensity from the LED lamp (375 nm). Finally, it was elucidated that Pt-Vis-TiO_2/N-Titanystar can oxidize various organic compounds into CO_2 as well as decompose ammonia gas into N_2 in the presence of O_2 even under visible light irradiation ($\lambda > 420$ nm) at 293 K.

2.5. References

[1] I. Sopyan, M. Watanabe, S. Murasawa, K. Hashimoto, A. Fujishima, *J. Photochem. Photobiol. A: Chem.*, **98**, 79 (1996)

[2] A. Fujishima, T.N. Rao, D.A. Tryk, *J. Photochem. Photobiol. C: Photochem. Rev.*, **1**, 1 (2000).

[3] S.C. Moon, Y. Matsumura, M. Kitano, M. Matsuoka, M. Anpo, *Res. Chem. Intermed.*, **29**, 233 (2003).

[4] M. Anpo, H. Yamashita, in M. Schiavello (Ed.), *Heterogeneous Catalysis*, Wiley, London (1997).

[5] M. Anpo, *Bull. Chem. Soc. Jpn.*, **77**, 1427 (2004).

[6] E. Borgarello, J. Kiwi, M. Gratzel, E. Pelizzetti, Visca M., *J. Am. Chem. Soc.*, **104**, 2996 (1982).

[7] W. Choi, A. Termin, M. R. Hoffmann, *J. Phys. Chem.*, **98**, 13669 (1994).

[8] T. Ohno, T. Tsubota, M. Toyofuku, R. Inaba, *Catal. Lett.*, **98**, 255 (2004).

[9] M. Takeuchi, M. Anpo, T. Hirao, N. Itoh, N. Iwamoto, *Surf. Sci. Jpn.*, **22**, 561 (2001).

[10] M. Kitano, M. Takeuchi, M. Matsuoka, J. M. Thomas, M. Anpo, *Chem. Lett.*, **34**, 616 (2005).

[11] M. Matsuoka, M. Kitano, M. Takeuchi, M. Anpo, J. M. Thomas, *Top. Catal.*, **35**, 305 (2005).

[12] A. L. Linsebigler, G.. Lu, J. T. Yates, *Chem. Rev.*, **95**, 735 (1995).

[13] M. Kitano, M. Matsuoka, M. Ueshima, M. Anpo, *Appl. Catal. A: General*, **325**, 1 (2007)

[14] M. Matsuoka, M. Kitano, S. Fukumoto, K. Iyatani, M. Takeuchi, M. Anpo, *Catal. Today*, **132**, 159 (2008)

[15] M. Kitano, K. Tsujimaru, M. Anpo, *Appl. Catal. A: General*, **314**, 179 (2006)

[16] M. Kitano, M. Takeuchi, M. Matsuoka, J. M. Thomas, M. Anpo, *Catal. Today*, **120**, 133 (2007)

[17] H. Chen, M. Matsuoka, J. Zhang, M. Anpo, *J. Catal.*, **228**, 75 (2004)

[18] M. Matsuoka, M. Kitano, M. Takeuchi, K. Tsujimaru, M. Anpo, J. M. Thomas, *Catal. Today*, **122**, 51 (2007)

Chapter 3

Photocatalytic Activity of a Photoelectrochemical Circuit System Consisting of a Rod-type TiO_2 Electrode and Silicon Solar Cell

3.1. Photocatalytic Decomposition of Ethanethiol on a Photoelectrochemical Circuit System Consisting of a Rod-Type TiO_2 Electrode and Silicon Solar Cell

3.1.1. Introduction

The TiO_2 photocatalyst is a fascinating photo-functional material which enables various useful reactions at ambient temperature such as the complete mineralization of toxic organic compounds [1], elimination of NOx in air [2] or hydrogen evolution from biomass [3]. These photocatalytic activities are based on the strong oxidation and reduction ability of the photo-formed holes and electrons, respectively. In addition to powdered TiO_2 photocatalysts, the photoelectrochemical properties of TiO_2 electrodes have been widely investigated. So far, it has been shown that the photocatalytic reaction rates as well as reaction dynamics of the photo-formed electrons and holes are significantly affected by the external electric bias applied to the TiO_2 electrodes. In our recent work, a unique photoelectrochemical circuit system consisting of a rod-type TiO_2 electrode and silicon solar cell has been constructed [4]. This photoelectrochemical circuit system can effectively oxidize lactic acid in water into CO_2, while the reaction rate is enhanced by the negative bias applied to the rod-type TiO_2 electrode by a silicon solar cell [4]. These results suggest that the photoelectrochemical circuit system can be utilized for the elimination of various undesirable toxic or odorous organic compounds. It is well known that methanethiol, which exists in the human buccal or oral cavity, is the cause of breath odor. Furthermore, it has been shown that ethanethiol is an important intermediate in the formation of methanethiol in the metabolic decomposition of sulfur-containing protein [5]. In the present work, the application of TiO_2 photocatalysts for dental care or buccal protection, especially for the prevention of bad breath, has been carried out with a the photoelectrochemical circuit system for the oxidation of ethanethiol in water. Moreover, the effect of the external bias as well as calcination temperature of the rod-

type TiO_2 electrode on the oxidation rate of ethanethiol has been investigated.

3.1.2. Experimental

Rod-type TiO_2 electrodes were prepared by the calcination of a metal Ti rod (3 mm × 78 mm) at various temperatures, i.e., without calcination, at 473 K, 673 K, 873 K, and 1073 K, for 3 min in air and denoted as TE_{273}, TE_{473}, TE_{673}, TE_{873} and TE_{1073}, respectively. The photoelectrochemical circuit systems were constructed by connecting the rod-type TiO_2 electrode and rod-type Pt electrode (denoted as PE: 3 mm × 78 mm) through a silicon solar cell (SSC: 2.4 V, 6 μA at 200 lx). Two different types of photoelectrochemical circuit systems (TE-SSC-PE) were constructed, i.e., TE-$^{+}$SSC^{-}-PE and TE-$^{-}$SSC^{+}-PE, as shown in Fig. 3.1.1(A). Here, TE is connected to the positive electrode of SSC for the former system (TE-$^{+}$SSC^{-}-PE), while TE is connected to the negative electrode of SSC for the latter (TE-$^{-}$SSC^{+}-PE). As shown in Fig. 3.1.2, the TE-$^{-}$SSC^{+}-PE system has been practically applied for the electric circuit of a toothbrush (Soladey 3; Shiken Corp.). In addition to the TE-SSC-PE system, three kinds of circuit systems (TE-PE, TE-TE, PE-PE) were constructed by directly connecting TE and PE. The photocatalytic decomposition reaction of ethanethiol (C_2H_5SH) was performed by using a closed reaction cell (Fig. 3.1.1(B)) under light irradiation from various light sources such as a black light lamp (6 W) or fluorescent lamp (6 W) at 298 K. The concentration of ethanethiol aqueous solution (18 ml) was adjusted to 0.08 mol/l and K_2SO_4 was added (0.30 mol/l) as the electrolyte. The amount of evolved CO_2 in the gas phase was analyzed by gas chromatography (Shimadzu, GC-7A). The crystal structure and surface morphologies of the rod-type TiO_2 electrodes were investigated by XRD (Shimadzu, XRD-6100) and scanning electron microscopy (SEM, Hitachi, S-4500). The XPS spectra were recorded under vacuum at 298 K (Shimadzu, ESCA3000). The photoelectrochemical properties of the rod-type TiO_2 electrodes were evaluated using a potentiostat (Hokuto Denko, HZ3000) where the rod-type TiO_2

electrode, Pt electrode and saturated calomel electrode (SCE) were set as the working, counter and reference electrodes, respectively. For the photoelectrochemical measurements, the working electrode was immersed in 0.25 M K_2SO_4/10 vol % methanol aqueous solution and irradiated with a 500 W Xenon lamp through a water filter.

3.1.3. Results and Discussion

Figure 3.1.3 shows the effect of the calcination temperature on the XRD pattern of the rod-type TiO_2 electrode (TE). Typical diffraction peaks of the Ti metal substrate (2θ = 38.5, 40.2) can mainly be observed when the calcination temperature is below 673 K, while diffraction peaks due to the rutile phase of TiO_2 (2θ = 27.5, 54.3) can be observed above 873 K. TE_{1073} shows the most intense diffraction peaks due to the rutile phase of TiO_2, while the intensity of the diffraction peaks due to the Ti metal substrate was remarkably decreased. These results clearly suggest that the surface of TE is covered by a rutile TiO_2 layer after calcination treatment above 873 K, while the thickness of the rutile TiO_2 layer increases with an increase in the calcination temperature. Figure 3.1.4 shows the effect of the calcination temperature on the Ti 2p XPS spectrum of the rod-type TiO_2 electrode. Typical Ti $2p_{1/2}$ and Ti $2p_{3/2}$ peaks due to the Ti^{4+} species were observed at around 465.1 and 459.4 eV, respectively, regardless of the calcination temperature [6,7]. These results show that the surface of the rod-type TiO_2 electrode is covered by a stoichiometric TiO_2 layer regardless of the calcination temperature.

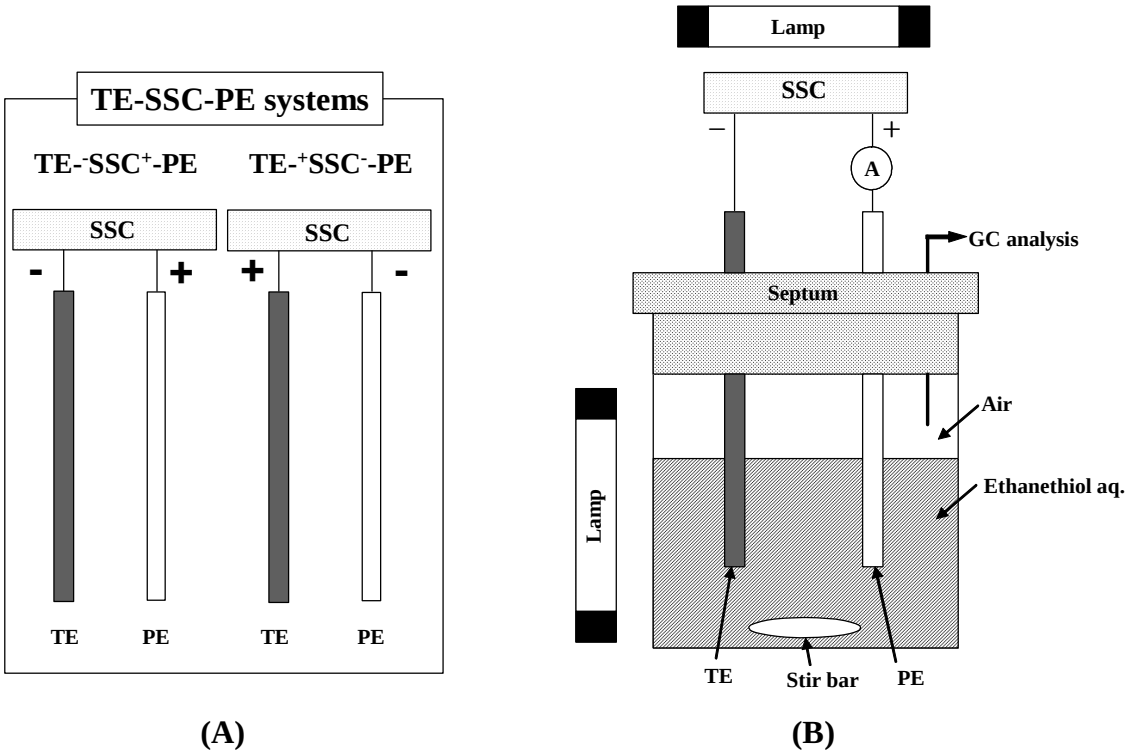

Figure 3.1.1. Schematic diagram of: (A) TE-SSC-PE systems and (B) reaction cell for the photocatalytic oxidation of ethanethiol

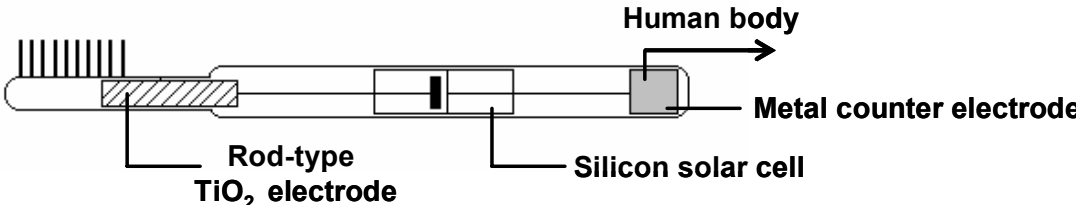

Figure 3.1.2. Schematic diagram of the electric circuit of a commercially produced toothbrush (Soladey 3; Shiken Corp.).

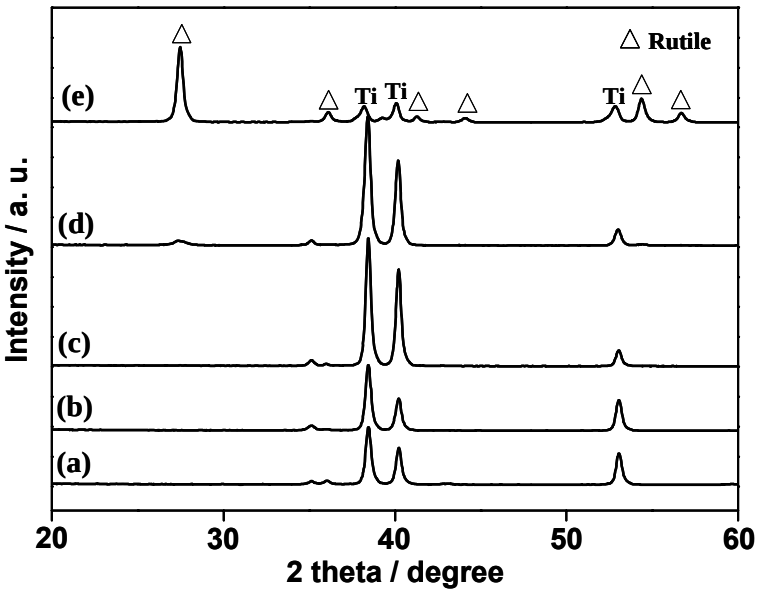

Figure 3.1.3. Effect of the calcination temperature on the XRD pattern of the rod-type TiO_2 electrode.

Calcination temperature (K): (a) Before calcination, (b) 473, (c) 673, (d) 873, (e) 1073.

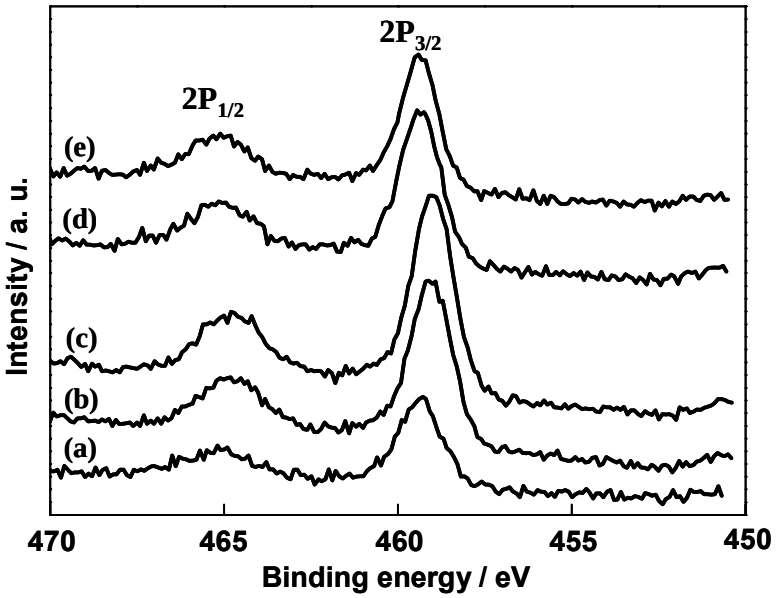

Figure 3.1.4. Effect of the calcination temperature on the XPS spectra of the Ti $2p_{3/2}$ and $2p_{1/2}$ peaks for the rod-type TiO_2 electrode.

Calcination temperature (K): (a) Before calcination, (b) 473, (c) 673, (d) 873, (e) 1073.

The rod-type TiO_2 electrode prepared at calcination temperatures of less than 873 K exhibited a rough surface morphology, while TE_{1073} showed a rather smooth and flat surface, as shown in Fig. 3.1.5. These results indicate that calcination at 1037 K is a suitable pretreatment to develop a dense and thick rutile TiO_2 layer on the rod-type TiO_2 electrode.

Photoelectrochemical measurements of the rod-type TiO_2 electrodes were performed in a 10 vol % methanol aqueous solution using a standard three-electrode system. Figure 3.1.6 shows the effect of the calcination temperature on the current-potential curves of the rod-type TiO_2 electrodes measured in 10 vol % methanol aqueous solution under UV irradiation. For all of the electrodes, the cathodic photocurrent dramatically increases under an applied negative bias of -1.0V (SCE: pH = 6), showing that the hydrogen evolution reaction can proceed on the electrode ($2H^+ + 2e^- \rightarrow H_2$). On the other hand, an anodic photocurrent was observed to proceed under an applied potential of –0.5 V and increased with an increase in the applied positive bias. These results suggest that the anodic oxidation of methanol by photo-formed holes occurs on these electrodes under UV irradiation of TE (λ > 300nm). Moreover, significant increases in the anodic photocurrent were observed with an increase in the calcination temperature, especially above 873 K. These results are in good agreement with XRD results showing that a dense and thick rutile TiO_2 layer can be developed on the TE after calcination treatment above 873 K. Figure 3.1.7 shows the photocurrent observed for the rod-type TiO_2 electrode (TE) calcined at various temperatures as a function of the incident light. Here, the wavelengths of the incident light were controlled by various cut-off filters. The observed photocurrent increased with an increase in the calcination temperature and the highest photocurrent was observed for TE_{1073}. Furthermore, the photoelectrochemical threshold onsets locate at around 400 nm independent of the calcination temperature, suggesting that the observed photocurrent is derived from the photoexcitation of the stoichiometric TiO_2 layers.

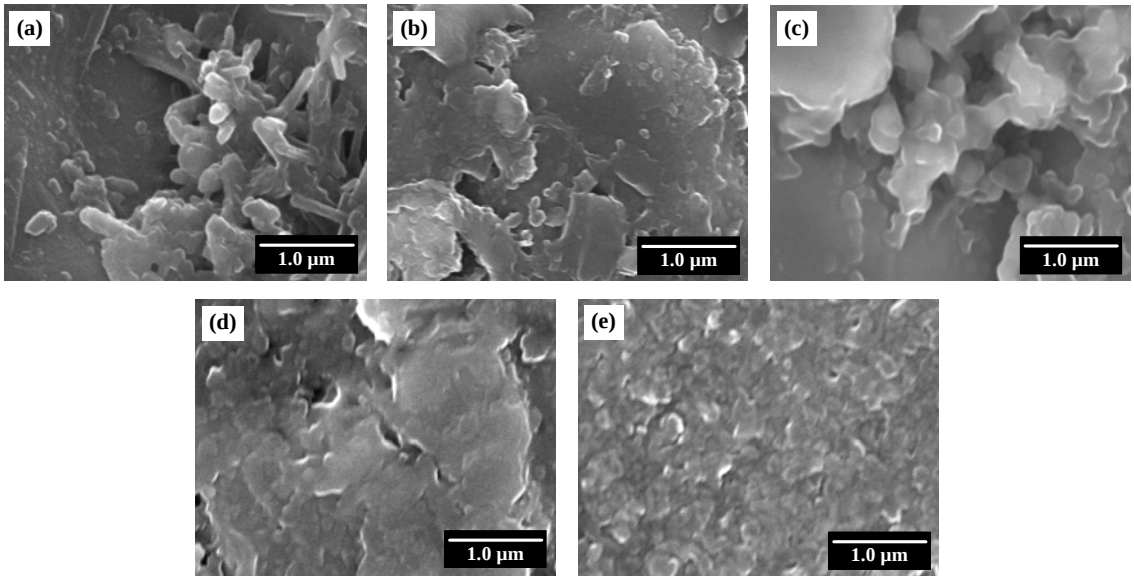

Figure 3.1.5. Effect of the calcination temperature on the SEM images of the rod-type TiO_2 electrode.

Calcination temperature (K): (a) Before calcination, (b) 473, (c) 673, (d) 873, (e) 1073.

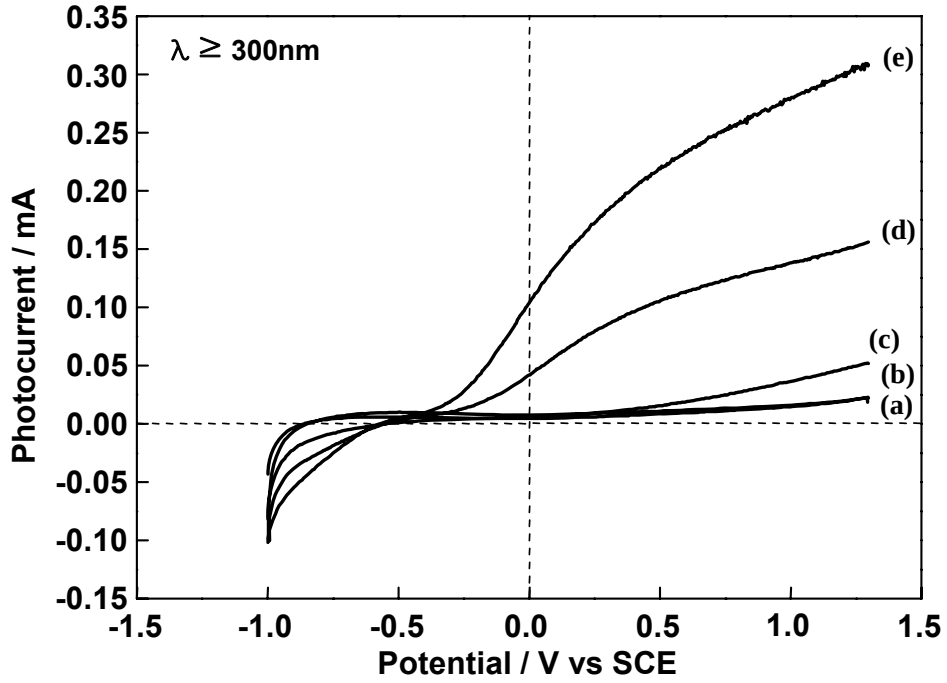

Figure 3.1.6. Effect of the calcination temperature on the current–potential curves of the rod-type TiO_2 electrodes measured in 10 vol % methanol aqueous solution under UV irradiation ($\lambda > 300$ nm).

Calcination temperature (K): (a) Before calcination, (b) 473, (c) 673, (d) 873, (e) 1073.

Light source: 500 W Xenon lamp.

Electrolyte: 0.1 M $HClO_4$ aq.

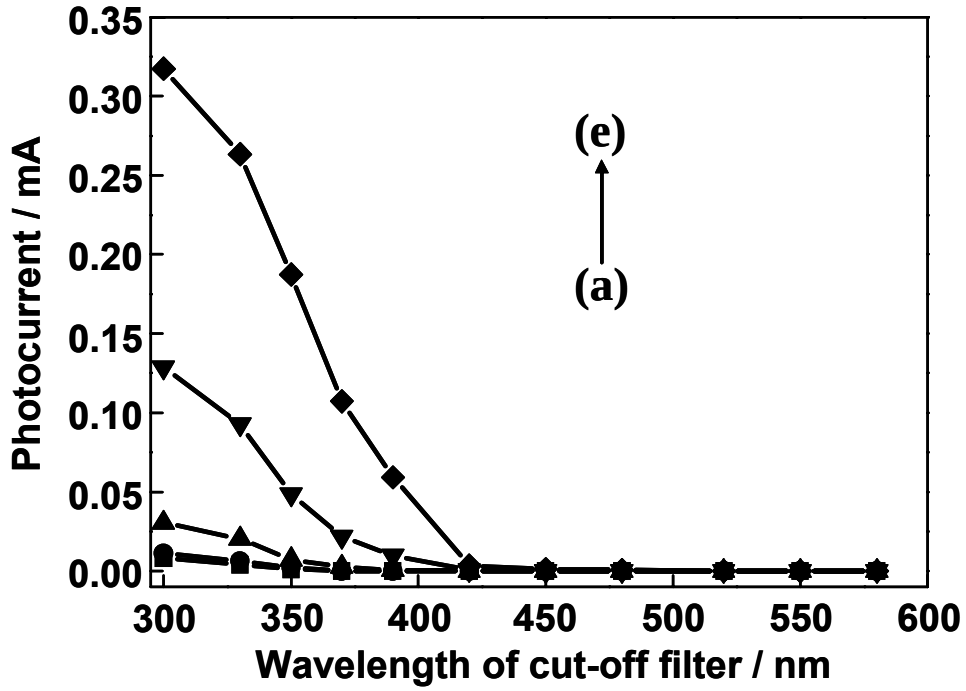

Figure 3.1.7. Relative photocurrent as a function of the cutoff wavelength of the incident light for the rod-type TiO_2 electrodes measured in 10 vol % methanol aqueous solution.

(Potential: +1.0 V vs SCE)

Calcination temperature (K): (a) Before calcination, (b) 473, (c) 673, (d) 873, (e) 1073.

Light source: 500 W Xenon lamp.

Electrolyte: 0.1 M $HClO_4$ aq.

The decomposition reaction of ethanethiol (C_2H_5SH) was investigated under light irradiation with a black light lamp (BL: 6 W) in a closed reaction cell at 298 K, as shown in Fig. 3.1.1. Figure 3.1.8 shows the yields of CO_2 in the photocatalytic decomposition of ethanethiol on various photoelectrochemical circuit systems and the irradiated parts of the photoelectrochemical circuit system are denoted in parenthesis. For example, TE-[$^+$SSC$^-$]-PE indicates that only SSC was irradiated, while [TE-$^+$SSC$^-$-PE] indicates that all parts of TE-$^+$SSC$^-$-PE were irradiated. Only a negligible formation of CO_2 and negligible current was observed on TE-SSC-PE under dark conditions, showing that the decomposition of ethanethiol does not proceed in the dark (data not shown). Moreover, CO_2 formation was not observed under light irradiation of the ethanethiol aqueous solution when the photoelectrochemical circuit system was not immersed in the solution (data not shown).

The decomposition of ethanethiol was investigated on three photoelectrochemical circuit systems (TE-[$^+$SSC$^-$]-PE, TE-[$^-$SSC$^+$]-PE, PE-[$^+$SSC$^-$]-PE) where only SSC was irradiated. CO_2 formations were observed for all three systems, showing that ethanethiol can be oxidized into CO_2 by electrolysis. It was also found that the circuit current observed for PE-[$^+$SSC$^-$]-PE (210 μA) was not affected by the presence of ethanethiol in the aqueous solution, showing that the observed circuit current is mainly ascribed to water electrolysis under an applied voltage by SSC. A higher circuit current was observed for TE-[$^+$SSC$^-$]-PE than TE-[$^-$SSC$^+$]-PE, which can be explained by the rectification effect due to the Schottky barrier at the interface between the TiO_2 layer and metal Ti. Next, the decomposition of ethanethiol was performed on three other kinds of photoelectrochemical circuit systems ([TE-PE], [TE-TE], [PE-PE]) where all of the electrodes were irradiated by a black light lamp. CO_2 formation was observed for [TE-TE] while only a negligible formation of CO_2 was observed for [PE-PE], showing that ethanethiol is photocatalytically decomposed into CO_2 on TE. Moreover, the yield of CO_2 was found to increase markedly for [TE-PE] as compared to

[TE-TE]. This enhancement of the photocatalytic activity can be ascribed to a decrease in the charge recombination rate due to the efficient transfer of the photo-formed electrons from TE to PE [8-11]. The decomposition of ethanethiol was performed on [TE-$^{-}$SSC^{+}-PE] and [TE-$^{+}$SSC^{-}-PE] where all parts of the photoelectrochemical circuit system were irradiated by a black light lamp. Light irradiation of both systems led to the efficient formation of CO_2, confirming that ethanethiol can be decomposed with these systems. The CO_2 yield on both systems was much higher than the sum of the CO_2 yield on TE-[$^{-}$SSC^{+}]-PE (0.3 μmol) and [TE-PE] (0.7 μmol). Moreover, [TE-$^{-}$SSC^{+}-PE] showed higher activity for the complete oxidation of ethanethiol than [TE-$^{+}$SSC^{-}-PE]. Since a higher circuit current was observed for [TE-$^{-}$SSC^{+}-PE] (270 μA) than [TE-$^{+}$SSC^{-}-PE] (220 μA), the activity of both systems was compared under the same circuit current. Here, the proper resistance was serially connected in the [TE-$^{-}$SSC^{+}-PE] circuit system and the circuit current was adjusted at 220 μA. This reaction condition was denoted as "[TE-$^{-}$SSC^{+}-PE] (current adjusted)". As shown in Fig. 3.1.8, [TE-$^{-}$SSC^{+}-PE] shows higher activity than [TE-$^{+}$SSC^{-}-PE] even under the same circuit current conditions (220 μA), showing that an applied negative bias on TE by SSC is more effective in enhancing ethanethiol decomposition than an applied positive bias. These results suggest that applying a negative bias on TE promoted the reduction of oxygen to form an O_2^{-} species on the surface of TE, leading to the efficient oxidation of ethanethiol into CO_2. Figure 3.1.8 shows the time dependences of the yields of CO_2 in the decomposition of ethanethiol on [TE-$^{-}$SSC^{+}-PE]. It can clearly be seen that light irradiation of the TE-$^{-}$SSC^{+}-PE system led to the formation of CO_2 with a good linearity against the light irradiation time, confirming the efficient and steady decomposition of ethanethiol on this system.

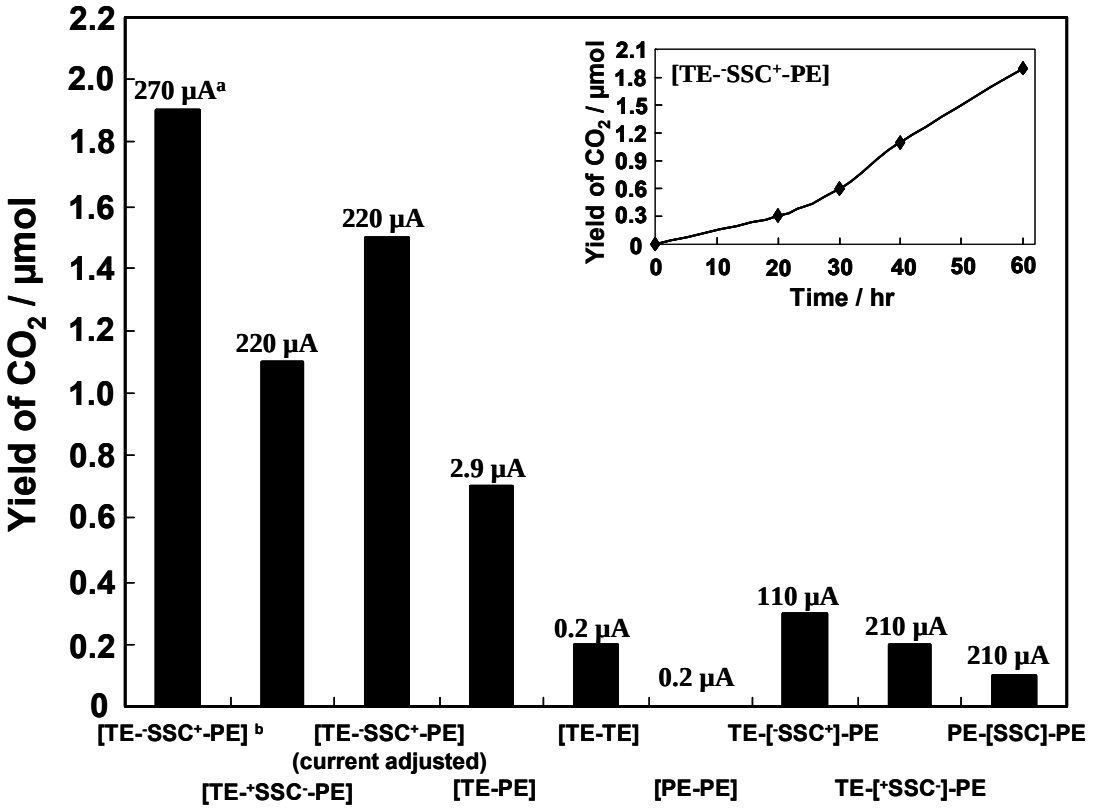

Figure 3.1.8. Yields of CO_2 in the decomposition of ethanethiol on various photoelectrochemical circuit systems.

Inset: Time profile of the CO_2 yield on [TE-$^{-}$SSC^{+}-PE].

[a]The absolute values of the observed short circuit current between two electrodes are shown on each bar.

[b]Irradiated parts of the photoelectrochemical circuit system are denoted in parentheses.

Light source: Black light lamp (6 W)

Irradiation time: 60 hrs

Figure 3.1.9 shows the effect of the calcination temperature of TE on the yield of CO_2 in the decomposition of ethanethiol on the [TE-$^-$SSC$^+$-PE] circuit system. It was clearly observed that the increase in the calcination temperature led to a marked increase in the CO_2 yields while TE_{1073} shows the highest activity for the complete oxidation of ethanethiol. These results show good agreement with the results of the current-potential curve measurements (Fig. 3.1.6), indicating that the dense and thick TiO_2 layer formed on TE_{1073} acted as the most efficient photocatalyst for the decomposition of ethanethiol. Finally, the decomposition reactions of ethanethiol were performed on various photoelectrochemical circuit systems under light irradiation from a fluorescent lamp (6 W). The CO_2 yield on [TE-$^-$SSC$^+$-PE] was almost the same as the sum of the CO_2 yields on [TE-PE] and TE-[$^-$SSC$^+$]-PE. Thus, no marked or dramatic synergy effect could be observed when combining the TE-PE system and SSC, in contrast to the case under black light irradiation (Fig. 3.1.8). However, these results clearly show that [TE-$^-$SSC$^+$-PE] can be practically applied for the clean and safe removal of ethanethiol in human buccal under light irradiation from a fluorescent lamp.

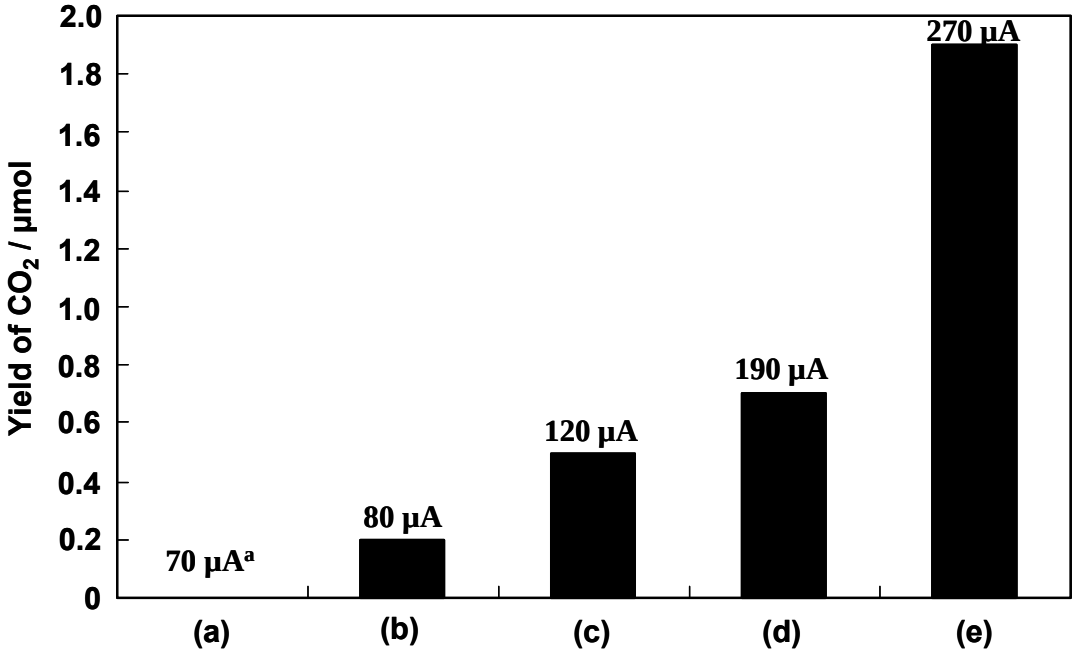

Figure 3.1.9. Effect of the calcination temperature of TE on the yield of CO_2 in the decomposition of ethanethiol on the [TE-$^{-}$SSC^{+}-PE] circuit system.

[a]The absolute values of the observed short circuit current between the two electrodes are shown on each bar.

Light source: Black light lamp (6 W)

Reaction time: 60 hrs

Calcination temperature (K): (a) Before calcination, (b) 473, (c) 673, (d) 873, (e) 1073.

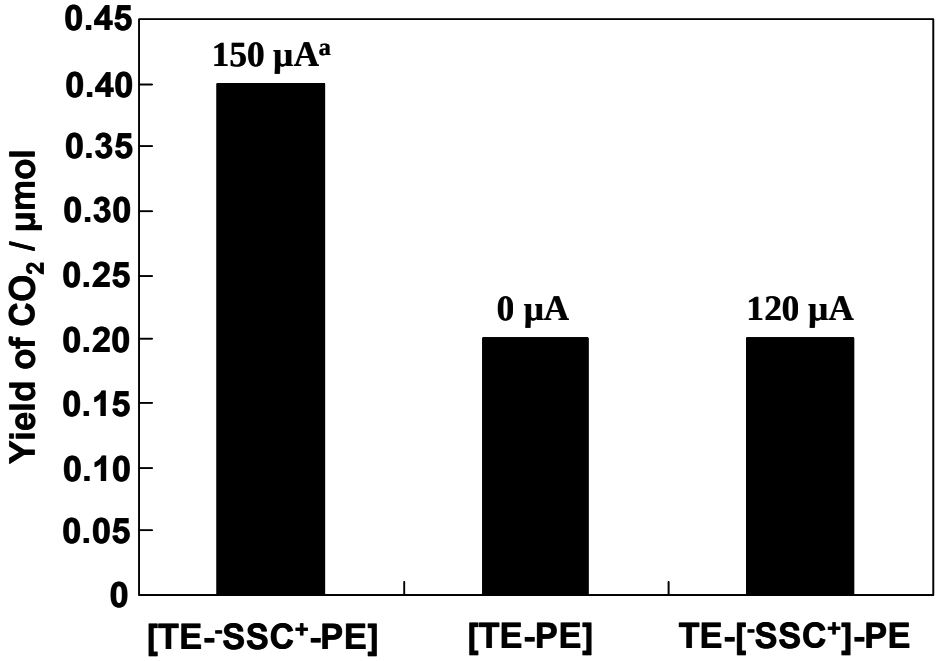

Figure 3.1.10. Yields of CO_2 in the decomposition of ethanethiol on various photoelectrochemical circuit systems.

Light source: Fluorescent lamp (6 W)

Reaction time: 60 hrs

3.1.4. Conclusions

It was found that the [TE-$^{-}$SSC^{+}-PE] system can efficiently oxidize ethanethiol in water into CO_2. The activity of [TE-$^{-}$SSC^{+}-PE] for the decomposition of ethanethiol was greatly affected by the calcination temperature of TE and TE_{1073} was observed to exhibit the highest activity for the oxidation of ethanethiol. Spectroscopic investigations have revealed that a dense and thick stoichiometric TiO_2 layer was formed on TE_{1073} which shows the highest activity for the decomposition of ethanethiol. A negative bias applied on TE by SSC was also found to markedly enhance the reaction rate, showing a remarkable synergy effect when combining the TE-PE system and SSC for the oxidation of ethanethiol. Finally, it was shown that [TE-$^{-}$SSC^{+}-PE] can be applied for the removal of ethanethiol in water even under light irradiation from a fluorescent lamp (6 W).

3.1.5. References

[1] D.F. Ollis, H. AlEkabi, *Photocatalytic Purification and Treatment of Water an d Air*, Elsevier, Amsterdam (1993).

[2] M. Anpo, in: P. Tundo, P. Anastas (Eds.), *Green Chemistry*, Oxford Universit y Press, 1 (2000).

[3] S. Fukumoto, M. Kitano, M. Takeuchi, M. Matsuoka, M. Anpo, *Catal. Lett.*, **127**, 39 (2009).

[4] M. Matsuoka, T. Kamegawa, D. Rakhmawaty, M. Kitano, K. Wada, M. Anpo, *Topics Catal.*, **47**, 162 (2008).

[5] K. Masatake, *Dental Magazine*, **105**, 32 (2002).

[6] B. Erdem, R.A. Hunsicker, G.W. Simmons, E.D. Sudol, V.L. Dimonie, M.S. El-Aasser, *Langmuir*, **17**, 2664 (2001).

[7] M. Kitano, K. Funatsu, M. Matsuoka, M. Ueshima, M. Anpo, *J. Phys. Chem. B*, **110**, 25266 (2006).

[8] J. Sa, M. Fernandez-Garcia, J.A. Anderson, *Catal. Commun*., **9**, 1991 (2008).

[9] M. Anpo, N. Aikawa, Y. Kubokawa, *J. Phys. Chem*., **88**, 3998 (1984).

[10] M. Kitano, K. Tsujimaru, M. Anpo, *Appl. Catal. A: Gen*., **314**, 179 (2006).

[11] M. Kitano, K. Iyatani, K. Tsujimaru, M. Matsuoka, M. Takeuchi, M. Ueshima, J.M. Thomas, M. Anpo, *Top. Catal.*, 49, 24 (2008).

3.2. Effect of Various Calcination Treatments on the Photocatalytic Activity of the Rod-Type TiO_2 Electrode

3.2.1. Introduction

Titanium dioxide (TiO_2) photocatalysts have attracted much attention due to their high photocatalytic activity and chemical stability. TiO_2 photocatalysts have many advantages for practical applications in such areas as the purification of toxic compounds in polluted water and air [1,2], elimination of NOx in air [3], and the photocatalytic decomposition of toxic agents in water [4] as well as for the development of self-cleaning materials [5]. Photoelectrochemical investigations have revealed that the photocatalytic reaction rates as well as reaction dynamics of the photo-formed electrons and holes are significantly affected by the external electric bias applied in the TiO_2 electrode [6,7]. Recently, we have reported on the construction of a unique photoelectrochemical circuit system consisting of a rod-type TiO_2 electrode and silicon solar cell [6,7]. This photoelectrochemical circuit system can efficiently oxidize lactic acid and ethanethiol in water into CO_2, while the reaction rate is enhanced by the negative bias applied on the rod-type TiO_2 electrode by a silicon solar cell [6,7]. However, the effect of various treatments of the rod-type TiO_2 electrode, such as calcination in NH_3 or under vacuum, on the decomposition rate of ethanethiol for the photoelectrochemical circuit system has not been fully investigated.

In the present work, enhancement of the photocatalytic activity of the photoelectrochemical circuit system has been undertaken by investigations into the effect of various treatments of the rod-type TiO_2 electrode, such as post-calcination in NH_3 or under vacuum, on the performance of this system for the oxidation of ethanethiol in water.

3.2.2. Experimental

The rod-type TiO_2 electrode (denoted as TE) was prepared by the calcination of a

metal Ti rod (ϕ 3 mm × 78 mm) at 1073 K for 3 min in air. The rod-type TiO_2 electrodes (TE) were then calcined in NH_3 (1.0×10^4 Pa) or under vacuum at various temperature, i.e., without calcination (293 K), 573 K, 673 K, 773 K, and 873 K for 2 hr. Photoelectrochemical circuit systems (TE-$^-$SSC$^+$-PE) were constructed by connecting TE and the rod-type Pt electrode through a silicon solar cell (SSC: 2.4 V, 6 μA at 200 lx), where TE was connected to the negative electrode of SSC. The TE-$^-$SSC$^+$-PE system has already been commercially applied for the electric circuit of a toothbrush (Soladey 3; Shiken Corp.). The photocatalytic decomposition reaction of ethanethiol (C_2H_5SH) in water was performed by using a closed reaction cell under black light lamp (6 W) light irradiation at 298 K. The concentration of the ethanethiol aqueous solution (18 ml) was adjusted to 0.08 mol/l and H_2SO_4 was added (0.30 mol/l) as the electrolyte. The amount of evolved CO_2 in the gas phase was analyzed by gas chromatography (Shimadzu, GC-7A). The crystal structure and surface morphologies of the rod-type TiO_2 electrodes were investigated by XRD (Shimadzu, XRD-6100) and scanning electron microscopy (SEM, Hitachi, S-4500). The XPS spectra were recorded under vacuum at 298 K (Shimadzu, ESCA3000). The photoelectrochemical properties of the rod-type TiO_2 electrodes were evaluated using a potentiostat (Hokuto Denko, HZ3000) where the rod-type TiO_2 electrode, Pt electrode and saturated calomel electrode (SCE) were set as the working, counter and reference electrodes, respectively. For the photoelectrochemical measurements, the working electrode was immersed in 0.25 M K_2SO_4/10 vol % methanol aqueous solution and irradiated with a 500 W Xenon lamp through a water filter.

3.2.3. Results and Discussions

Figure 3.2.1 shows the effect of the temperature of post-calcination treatment in NH_3 or under vacuum on the XRD pattern of TE. The XRD pattern shows typical diffraction peaks due to the Ti metal substrate and a rutile phase of TiO_2 (Fig. 3.2.1(a)).

These results suggest that the surface of TE is covered with a TiO_2 layer having a rutile phase. As shown in Fig. 3.2.1 (A) and (B), the peak intensity of the rutile phase of TE scarcely changes with an increase in the post- calcination temperature, showing that the crystallinity as well as crystal phase of the TiO_2 layer formed at the surface of TE is scarcely affected by these post-calcination treatments in NH_3 or under vacuum. Figure 3.2.2 shows the effect of these treatments on the Ti 2p XPS spectrum of TE. Typical Ti $2p_{1/2}$ and Ti $2p_{3/2}$ peaks were observed for all samples at around 464.0 eV and 458.3 eV, indicating that these peak positions are in good agreement with those observed for the Ti^{4+} species reported in previous literature [8-10]. These results also show good agreement with the XRD results which indicate that the surface of TE is covered with a TiO_2 layer of the rutile phase regardless of the kind of calcination atmosphere. Figure 3.2.3 shows the effect of post-calcination treatment in NH_3 on the N 1s XPS spectrum of TE. As shown in Fig. 3.2.3, the N 1s peak was observed at around 399.8 eV when the calcination temperature was below 673 K. The N 1s peak observed at around 399.8 eV can be attributed to the N_2 molecules adsorbed on the TiO_2 surface [11]. Moreover, when the calcination temperature is raised above 673 K, the shoulder peak which can be assigned to the N 1s peak to the TiN moieties can be observed at around 376.5 eV. These results clearly suggest that the calcination of TE in the presence of NH_3 above 673 K led to the formation of a TiN layer at the surface of TE through the substitution of lattice oxygen with the nitrogen atoms. Figure 3.2.4 shows the effect of the post-calcination treatment in NH_3 or under vacuum on the SEM images of TE. It can be clearly seen that the surface roughness increased with an increase in the calcination temperature up to 773 K while decreasing at a calcination temperature of 873 K regardless of the kind of gas atmosphere (NH_3 or vacuum). These results indicate that post-calcination at 773 K is a suitable pretreatment to develop a highly active rutile TiO_2 layer with high surface roughness on TE. The photoelectrochemical properties of TE were investigated using a standard three-electrode system. Figure

3.2.5 shows the effect of the calcination treatments in NH_3 or under vacuum on the current-potential curves of TE measured in 10 vol % methanol aqueous solution under UV irradiation. As shown in Fig. 3.2.5(A), an anodic photocurrent was observed for all of the electrodes under a scanning potential of -0.5 V to +1.3 V and its intensity increased with an increase in the applied positive bias. Furthermore, regardless of the kind of gas atmosphere (NH_3 or vacuum), the anodic photocurrent increased with an increase in the calcination temperature until the maximum values were attained at 773 K and then decreased at a calcination temperature of 873 K. It should be noted that the highest photocurrent was observed for TE calcined at 773 K under NH_3 atmosphere. Furthermore, as shown in the inset of Fig. 3.2.5, for the electrodes, the cathodic photocurrent increased dramatically when a negative bias of -1.0 V (SCE : pH = 6) was applied, showing that a hydrogen evolution reaction proceeds on the electrode calcined at 773 K in NH_3 or vacuum ($2H^+ + 2e^- \rightarrow H_2$).

These results suggest that the anodic oxidation of methanol by photo-formed holes proceeds efficiently on these electrodes under UV irradiation of TE ($\lambda \geq 300$ nm) and that the photoelectrochemical properties of TE can be dramatically improved by calcination treatment at 773 K under NH_3 atmosphere. The high photoelectrochemical performance of TE calcined at 773 K in NH_3 atmosphere can be attributed to the high surface roughness morphology of the rutile TiO_2 layer.

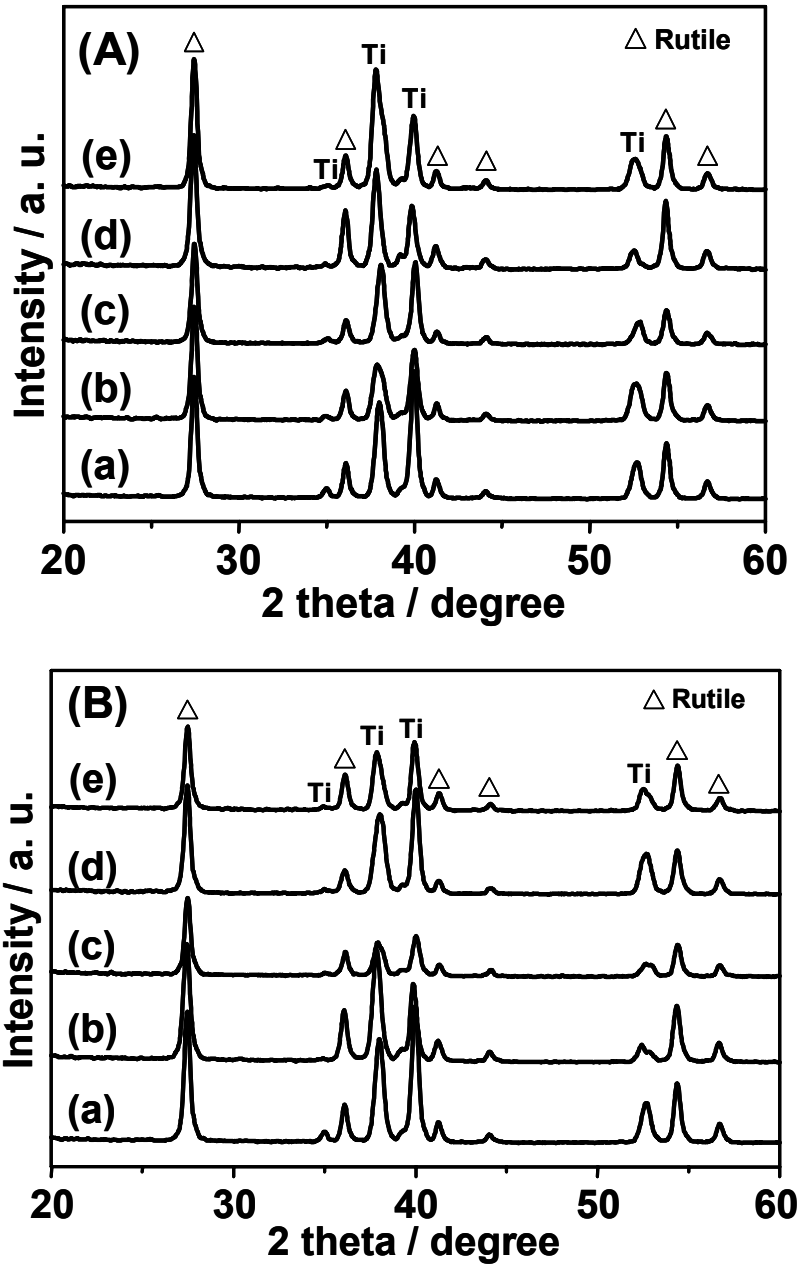

Figure 3.2.1. Effect of the temperatures of post-calcination treatment (A) in NH_3 and (B) under vacuum on the XRD pattern of the rod-type TiO_2 electrode.

Calcination temperature (K): (a) without calcination, (b) 573, (c) 673, (d) 773, (e) 873.

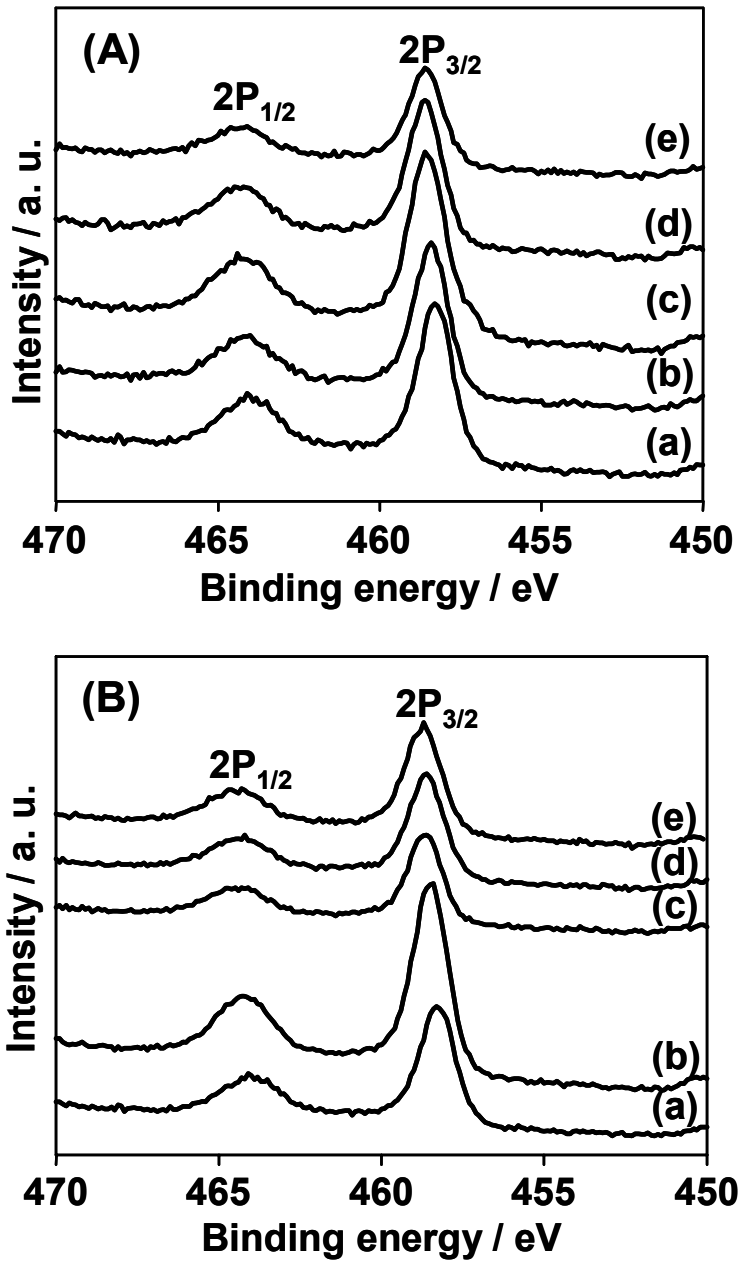

Figure 3.2.2. Effect of the temperatures of post-calcination treatment (A) in NH_3 and (B) under vacuum on the Ti $2p_{3/2}$ and $2p_{1/2}$ peaks of the XPS spectra for the rod-type TiO2 electrode.

Calcination temperature (K): (a) without calcination, (b) 573, (c) 673, (d) 773, (e) 873.

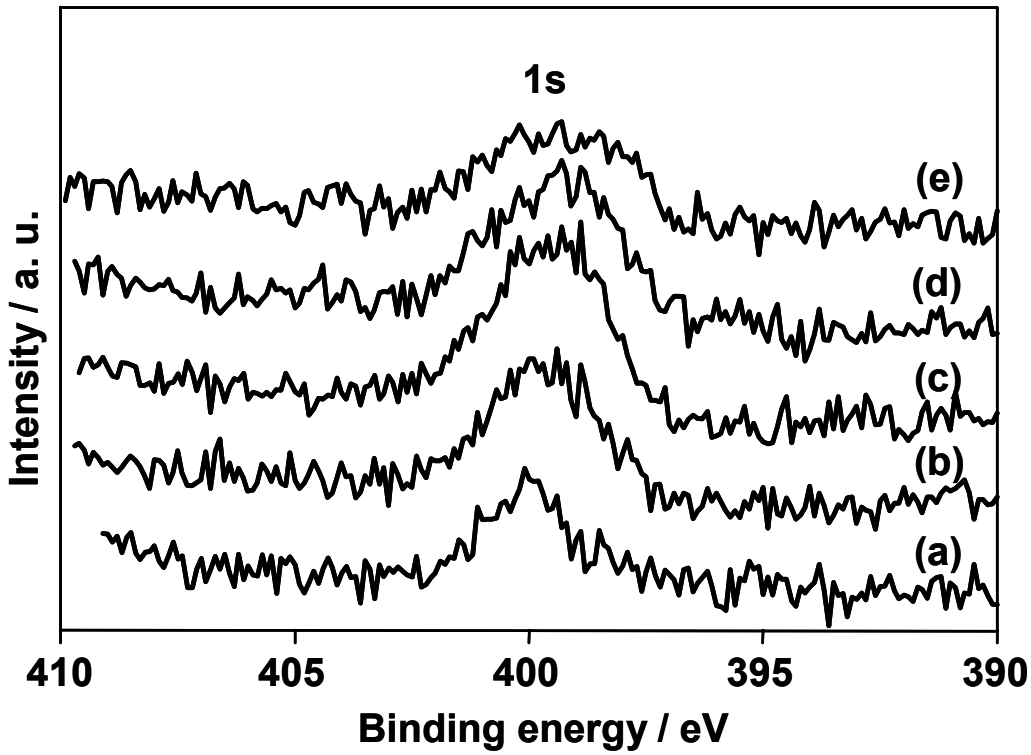

Figure 3.2.3. Effect of the temperatures of the calcination treatment in NH_3 on the XPS spectra of the N 1s peaks for the rod-type TiO_2 electrode.

Calcination temperature (K): (a) without calcination, (b) 573, (c) 673, (d) 773, (e) 873.

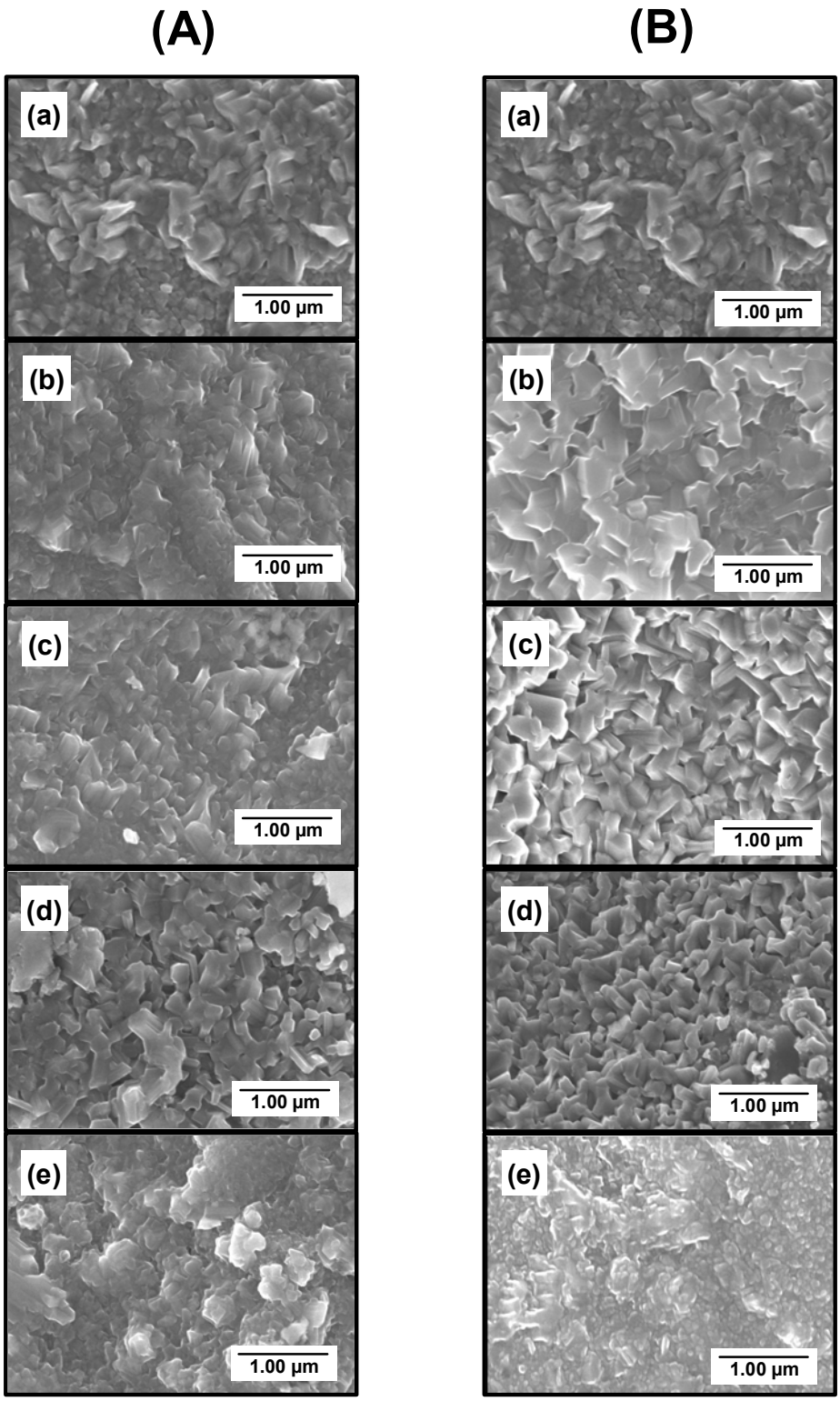

Figure 3.2.4. Effect of the temperatures of calcination treatment (A) in NH_3 and (B) under vacuum on the SEM images of the rod-type TiO_2 electrode.

Calcination temperature (K): (a) without calcination, (b) 573, (c) 673, (d) 773, (e) 873.

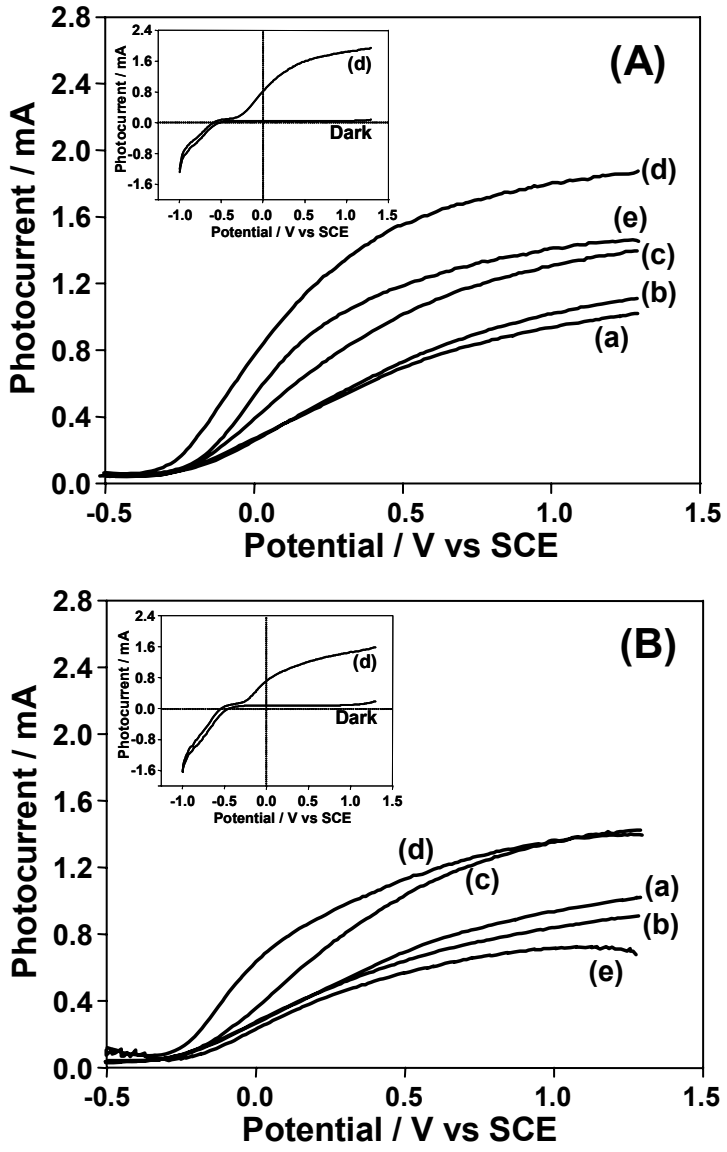

Figure 3.2.5. Effect of post-calcination (A) in NH_3 and (B) under vacuum on the current-potential curves of the rod-type TiO_2 electrodes measured in 10 vol % methanol aqueous solution under UV irradiation ($\lambda \geq 300$ nm). (All curves were recorded as the difference in the current-potential curves under UV irradiation and dark, except for the insets.)

Calcination temperature (K): (a) Before calcination, (b) 573, (c) 673, (d) 773, (e) 873.

Light source : 500 W Xenon lamp.

Electrolyte : 0.1 M HClO4 aq.

The oxidation reaction of ethanethiol (C_2H_5SH) was performed by using a closed system reaction cell under light irradiation from a black light lamp (BL: 6W) at room temperature (Fig. 3.1.1). This photoelectrochemical system has actually been practically applied for the electric circuit of a toothbrush (Soladey 3; Shicken Corp.) equipped with a silicon solar cell (2.4 V, 6 μA) and counter electrode (Fig. 3.1.2). Figure 3.2.6 shows the effect of the calcination treatment of TE in NH_3 or under vacuum on the yield of CO_2 in the decomposition of ethanethiol on this photoelectrochemical circuit system. The yields of CO_2 increased with an increase in the calcination temperature up to 773 K regardless of the kind of gas atmosphere, and then decreased at a calcination temperature of 873 K. It was thus found that TE calcined at 773 K in NH_3 shows the highest photocatalytic performance for the complete oxidation of ethanethiol. These results show good agreement with the results of the current-potential curve measurements (Fig. 3.2.5), indicating that the rutile TiO_2 layer formed on TE by calcination treatment at 773 K in NH_3 and having a high surface roughness morphology shows the highest photocatalytic activity for the oxidation of ethanethiol.

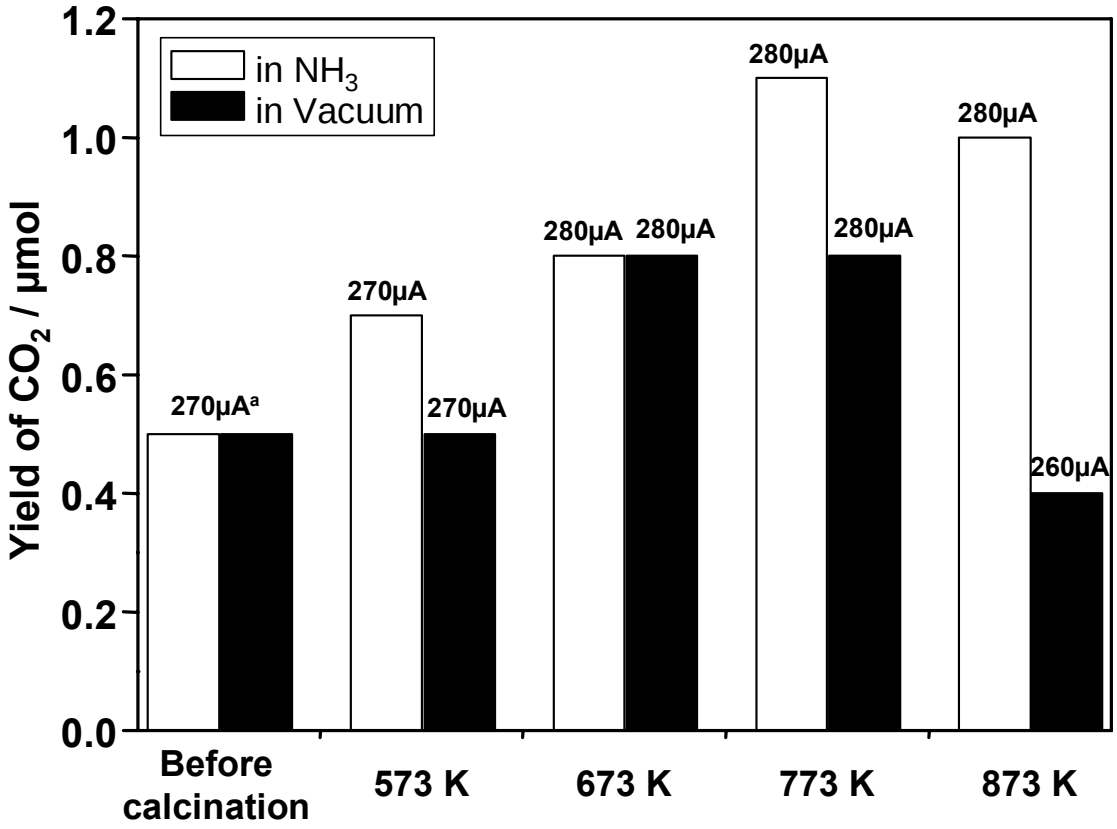

Figure 3.2.6. Effect of the temperatures of post-calcination treatments in NH_3 or under vacuum of the rod-type TiO_2 electrode on the yield of CO_2 in the decomposition of ethanethiol on the photoelectrochemical circuit system (TE-$^{-}$SSC^{+}-PE).

The absolute values of the observed short circuit current between two electrodes are shown on each bar.

Light source : Black light lamp (6 W).

Reaction time : 30 hrs.

3.2.4. Conclusions

A rod-type TiO_2 electrode (TE) has been prepared by calcination treatment of a metal Ti rod at 1073 K for 3 min and its photoelectrochemical performance was investigated. It was found that the photoelectrochemical performance of TE is greatly enhanced by post calcination treatment at 773 K in NH_3 or in vacuum. A unique photoelectrochemical circuit system was constructed by connecting a rod-type TiO_2 electrode with a Pt electrode through a silicon solar cell. This novel photoelectrochemical circuit system (TE-$^-$SSC$^+$-PE) was found to efficiently oxidize ethanethiol in water into CO_2 where the negative bias was applied on TE by SSC. The activity of the photoelectrochemical circuit system for the decomposition of ethanethiol was greatly affected by the temperature of the post-calcination treatment of TE in NH_3 or in vacuum. Spectroscopic investigations have revealed that a rutile TiO_2 layer with a morphology of high surface roughness was formed on TE after post-calcination treatment at 773 K in NH_3, showing the highest activity for the decomposition of ethanethiol.

3.2.5. References

[1] I. Sopyan, M. Watanabe, S. Murasawa, K. Hashimoto, A. Fujishima, *J. Photochem. Photobiol. A*, **98**, 79 (1996).

[2] A. Fujishima, T. N. Rao, D. A. Tryk, *J. Photochem. Photobiol. C : Photochem. Rev.*, **1**, 1 (2000).

[3] M. Anpo, in: P. Anastas (Eds.), *Green Chemistry*, Oxford University Press, 1, (2000).

[4] Y. Paz, Z. Luo, L. Rabenberg, A. Heller, *J. Mater. Res.*, **10**, 2842 (1995).

[5] S. C. Moon, Y. Matsumura, M. Kitano, M. Matsuoka, M. Anpo, *Res. Chem. Intermed.*, **29**, 233 (2003).

[6] M. Matsuoka, T. Kamegawa, D. Rakhmawaty, M. Kitano, K. Wada, M. Anpo, *Topics Catal.*, **47**, 162 (2008).

[7] T. H. Kim, M. Saito, M. Matsuoka, S. Tsukada, K. Wada, M. Anpo, *Res. Chem. Intermed.*, **35**, 633 (2009).

[8] C.N. Sayers, N.R. Armstrong, *Surf. Sci.*, **77**, 301 (1978)

[9] B. Erdem, R.A. Hunsicker, G.W. Simmons, E.D. Sudol, V.L. Dimonie, M.S. El-Aasser, *Langmuir*, **17**, 2664 (2001)

[10] Z.W. Zhao, B.K. Tay, S.P. Lau, G.Q. Yu, *J. Crystal Growth*, **268**, 543 (2004)

[11] J. Yang, H. Bai, X. Tan, J. Lian, *Appl. Surf. Sci.*, **253**, 1988 (2006)

Chapter 4

Effect of Surface Modification by Fluoride Ions for the Selective Photocatalytic Oxidation of Benzyl Alcohol into Benzaldehyde by O_2 on TiO_2 under Visible Light

4.1. Introduction

Titanium dioxides (TiO_2) are a promising nano-sized material for such photochemical applications [1-4] as H_2 production by water splitting, the degradation of volatile organic compounds (VOC), organic synthesis, dye-sensitized solar cells, and super-hydrophilic materials. Since the band gap of TiO_2 with an anatase structure is ca. 3.2 eV, it can only be activated by UV light, however, only a low percentage reaches the earth's surface from the sun. In order to utilize as much clean and safe solar energy as possible, the development of visible light-sensitive nano-photocatalysts is essential.

Meanwhile, the photo-oxidation of alcohol into aldehyde or ketone has been widely studied on TiO_2 [4-16] and Nb_2O_5 [17, 18]. In particular, the selective photocatalytic oxidation of aromatic compounds such as benzyl alcohol in the presence of O_2 under only UV-light irradiation has previously been reported on TiO_2 in the gas phase [9], in acetonitrile [10, 11] or in aqueous solution [12-16].

On the other hand, we have recently reported the photocatalytic oxidation of benzyl alcohol and its derivatives on TiO_2 in the presence of O_2 [19]. TiO_2 was found to exhibit the selective photocatalytic oxidation of benzyl alcohol and its derivatives such as 4-methoxybenzyl alcohol, 4-chlorobenzyl alcohol, 4-nitrobenzyl alcohol, 4-methylbenzyl alcohol, 4-(trifluoromethyl)benzyl alcohol, and 4-tertiary-butylbenzyl alcohol into corresponding aldehydes at high conversion and selectivity under irradiation with both UV and visible light. It was also demonstrated that the surface complex formed by the interaction of benzyl alcohol with TiO_2 induces visible light absorption and plays a vital role in the selective photocatalytic oxidation reaction. On the other hand, Shishido et al. have recently reported the mechanism behind the photooxidation of alcohol over Nb_2O_5 and demonstrated the surface complex of the alcoholate species which is activated by visible light, leading to the formation of a carbonyl compound [18].

In order to understand the surface interactions between TiO_2 and benzyl alcohol,

the effect of the calcination temperature of TiO_2 as well as HF treatment on the selective photocatalytic oxidation of benzyl alcohol into benzaldehyde under visible light irradiation have been investigated.

4.2. Experimental

TiO_2 (ST-01, Ishihara Co. Ltd) was used in the photocatalytic reactions and two different surface modifications of TiO_2 (ST-01) were performed: 1) TiO_2 was calcinated at varying temperatures (673 - 973 K) for 3 h in an electric furnace under air atmosphere. The temperature was raised at a rate of 5 K min^{-1}. The TiO_2 photocatalysts calcinated at 673, 773, 873 and 973 K are referred to as TiO_2(673), TiO_2(773), TiO_2(873) and TiO_2(973), respectively; and 2) 2.0 g of the untreated TiO_2 was suspended in 50 mL H_2O involving different volumes (12.5, 25, 110 and 400 μL) of 50 % HF solution for 2 h. The presence of F^- ions in the filtrate separated from the TiO_2 suspension was determined by the addition of $CaCl_2$ solution to form a CaF_2 precipitate (limitation detected: > 7 ppm). F^- ions could hardly be detected in the bulk solution for all the samples prepared, suggesting that they were mostly adsorbed on the TiO_2 surface. After HF treatment, the samples were washed in distilled water, filtrated, and dried at 343 K for 12 h. The HF-treated TiO_2 were then referred to as HF(x)-TiO_2 (x: 12.5, 25, 110 and 400). The x stands for the volume (μL) of 50 % HF solution added to the preparation of HF-TiO_2. Furthermore, HF(400)-TiO_2 was stirred in 0.1 M NaOH solution for 2 h, washed in distilled water, dried at 343 K for 12 h and referred to as NaOH-HF(400)-TiO_2.

Photo-oxidations of benzyl alcohol were performed on the TiO_2 photocatalysts at room temperature. The photocatalysts (50 mg each) were dispersed in acetonitrile solution (10 mL) involving benzyl alcohol (50 μmol) in a test tube made of pyrex glass (volume: 20 mL) and the gas phase was purged by O_2 at 298 K. The photo-reaction cell was set at a photo-intensity of ca. 1.8×10^4 lux emitted from a blue LED lamp ($\lambda >$

400 nm) and measured by an illumination meter, TMS 870 (TASCO Japan Co., Ltd.).

After the reaction, the catalysts were immediately separated from the TiO_2 suspension by filtration through a 0.20 μm membrane filter (Dismic-25, Advantec). The solution was then analyzed by HPLC (Shimadzu LC10ATVP, UV-Vis detector, column: Chemcopak, mobile phase: a mixture of acetonitrile and 1.0 % formic acid aqueous solution) and the head space was analyzed by GC (Ohkura, Model-802, column: porapak Q).

X-ray diffraction (XRD) patterns were obtained with a RIGAKU RINT2000 using Cu K_α radiation (λ = 1.5417 Å) within a scan range of 20 - 60° and a scan speed of 2° min^{-1}. The crystallite size of TiO_2 was estimated by the Scherrer equation (1).

$$d = 0.9\,\lambda / \beta \cos\theta \qquad (1)$$

Here, d is the crystallite size, λ is the wavelength of X-ray ($CuK_{\alpha 1}$, λ =1.5417 Å), β is the full width at half maximum (FWHM, radian) at the diffraction angle of θ. The specific BET surface area of the samples was estimated from the amount of N_2 adsorption at 77 K using the BET equilibrium equation. The atomic composition of the HF-treated TiO_2 was analyzed by X-ray photoelectron spectroscopy (XPS, ESCA 3200, Shimadzu). The C_{1s} peak (E_b = 285.0 eV) as an internal standard was used for energy calibration.

UV-Vis spectroscopic measurements were carried out using a UV-Vis recording spectrophotometer (UV-2200A, Shimadzu) in diffuse reflectance mode. For the UV-Vis measurement, the benzyl alcohol-adsorbed TiO_2 was prepared as follows: 1g of TiO_2 or HF(400)-TiO_2 for each was stirred in acetonitrile involving 1.0 M benzyl alcohol, followed by washing with acetonitrile and drying in air at room temperature.

4.3. Results and Discussion

Optical properties of benzyl alcohol-adsorbed TiO_2

In order to understand the optical properties, the UV-Vis absorption spectra of: (a) TiO_2 by itself, (b) the benzyl alcohol-adsorbed TiO_2, (c) HF(400)-TiO_2, and (d) the benzyl alcohol-adsorbed HF(400)-TiO_2 were investigated and the results are shown in Fig. 4.1. It was observed that both TiO_2 and HF(400)-TiO_2 exhibit absorption only in the UV region with a band-gap transition at ca. 385 nm (3.2 eV), as shown in Fig. 4.1 (a, c). In contrast, as can be seen in Fig. 4.1 (b, d), absorption in the visible region appears in the spectrum when benzyl alcohol is adsorbed on TiO_2 and HF(400)-TiO_2. An intensity of the absorption in the visible region for the benzyl alcohol-adsorbed HF(400)-TiO_2 is similar to that of benzyl alcohol-adsorbed TiO_2 (see Figs. 4.1 (b) and (d)). This absorption in the visible light region can be assigned to the surface complex through a ligand-to-metal charge transfer (LMCT) between the substrates and Ti sites on the surface [20, 21]. From these results, absorption in the visible region of the surface complex can be expected to lead to photocatalytic reactions under visible light irradiation. Photocatalytic reactions could, therefore, be carried out under irradiation with visible light emitted from a LED lamp and the energy distribution is shown in Fig. 4.1 (e).

Photocatalytic oxidation of benzyl alcohol on TiO_2 under visible light irradiation

Figure 4.2 shows the oxidation of benzyl alcohol on the TiO_2 photocatalyst as a function of time under irradiation with visible light emitted from the LED lamp. It was confirmed that the oxidation reaction does not take place under photo-irradiation without a TiO_2 photocatalyst nor with a TiO_2 photocatalyst without irradiation, i.e., both TiO_2 and irradiation are both required in combination for the oxidation reaction to occur. Before irradiation, a decrease in the amount of benzyl alcohol originating from its adsorption on TiO_2 was observed. Photo-irradiation was carried out after confirming the equilibrium adsorption of benzyl alcohol. With an increase in time under visible light irradiation, a decrease in benzyl alcohol was observed while the yield of

benzaldehyde increased. It was found that the yields of benzaldehyde increased up to ca. 95 % and the carbon balance in the liquid phase was ca. 95 % after photo-irradiation for 240 min. Benzaldehyde by itself was also confirmed to oxidize into benzoic acid or CO_2 under visible light irradiation within 240 min.

Effect of calcination temperature of TiO_2 on the photocatalytic oxidation of benzyl alcohol

Figure 4.3 shows the photocatalytic oxidation of benzyl alcohol on the TiO_2 photocatalysts treated by calcination at different temperatures. As shown in Fig. 4.3 [I], the amount of photo-formed benzaldehyde increased with an increase in time and the activity decreased in the following order: un-treated TiO_2 > TiO_2(673) > TiO_2(773) > TiO_2(873) > TiO_2(973). The reaction rate constants of k are estimated from Equation (2), as follows:

$$k\,t = \ln \{a / (a-x)\} \qquad (2)$$

When the condition is given that the concentration of the molecular oxygen during the photocatalytic reactions remain constant, the kinetics are ruled by a first-order reaction. The linear relationship of ln {a / (a-x)} vs. t (time) was plotted, as shown in Fig. 4.3 [II], and slope k determined. Here, the amount of benzyl alcohol added (50 mol) and the amount of the photo-formed benzaldehyde are defined as a and x, respectively, as a function of time (t). The reaction rate constants for the photocatalytic oxidation of benzyl alcohol into benzaldehyde as well as the amount of adsorbed benzyl alcohol in dark are listed in Table 1. XRD analysis revealed that all of the TiO_2 listed in Table 1 possess an anatase structure and the BET surface area decreases due to aggregation of the TiO_2 particles, while the crystallite size increases with an increase in the calcination temperature of TiO_2.

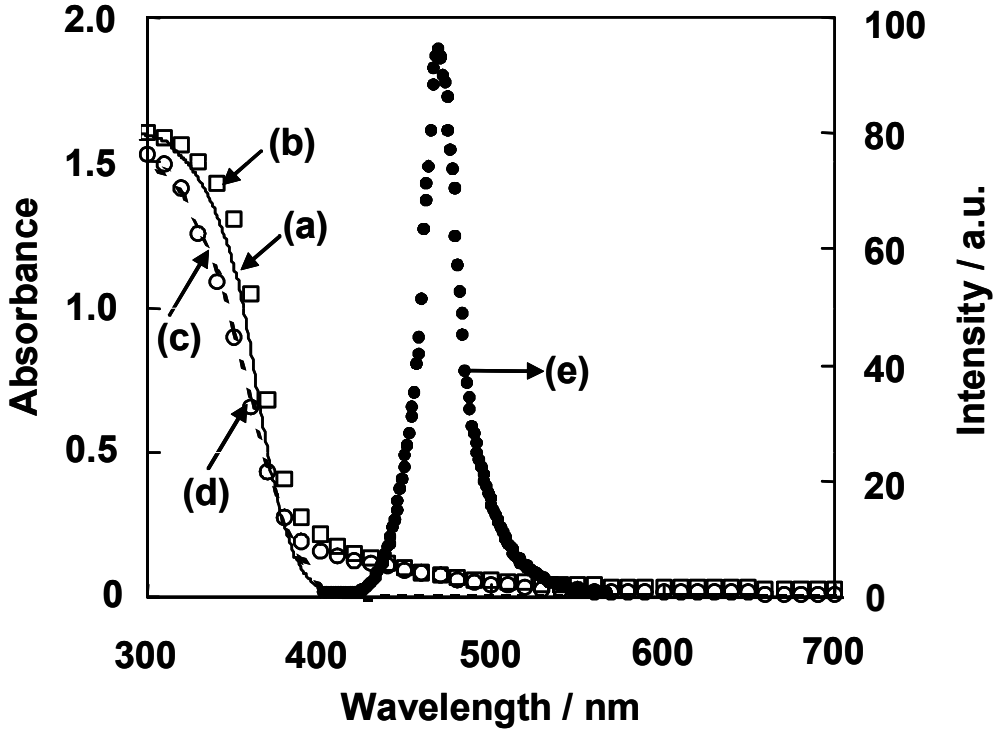

Figure 4.1. The UV-Vis absorption spectra of: (a: solid line) TiO_2 by itself; (b: open square) benzyl alcohol-adsorbed TiO_2; (c: broken line) HF(400)-TiO_2; (d: open circle) benzyl alcohol-adsorbed HF(400)-TiO_2; and (e) the energy profile of the LED lamp used in the experiments.

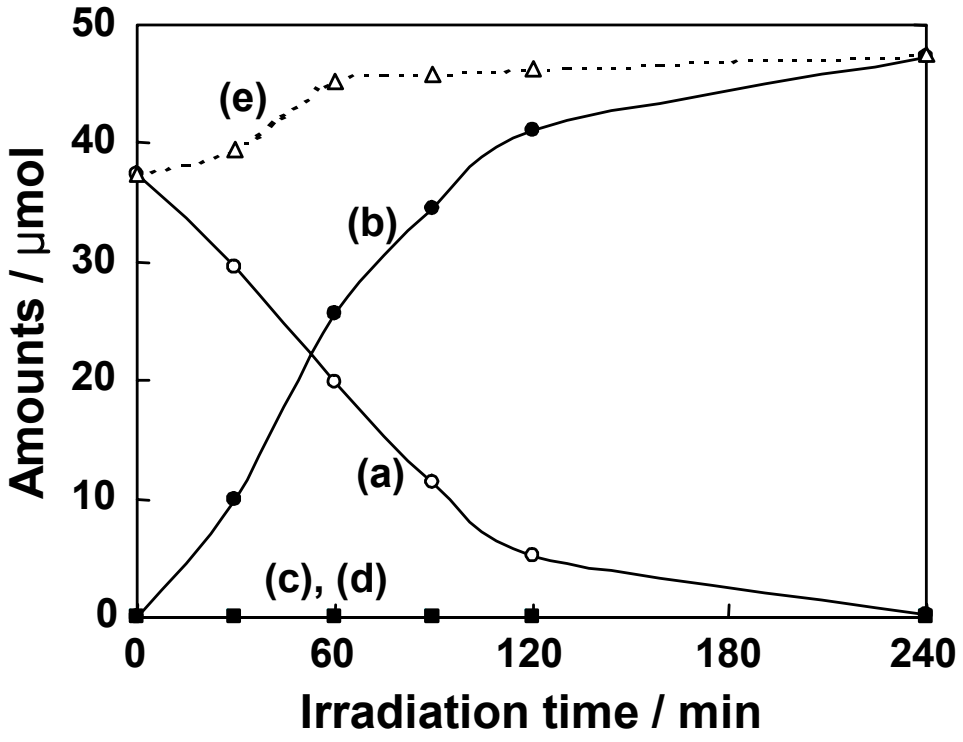

Figure 4.2. Photocatalytic oxidation of benzyl alcohol on TiO_2 (50 mg) under visible light emitted from a LED lamp. The initial amount of benzyl alcohol added to the reaction cell was 50 μmol. The plotted amounts of: (a) benzyl alcohol; (b) benzaldehyde; (c) benzoic acid; (d) CO_2; and (e) both benzyl alcohol and benzaldehyde evolved in solution.

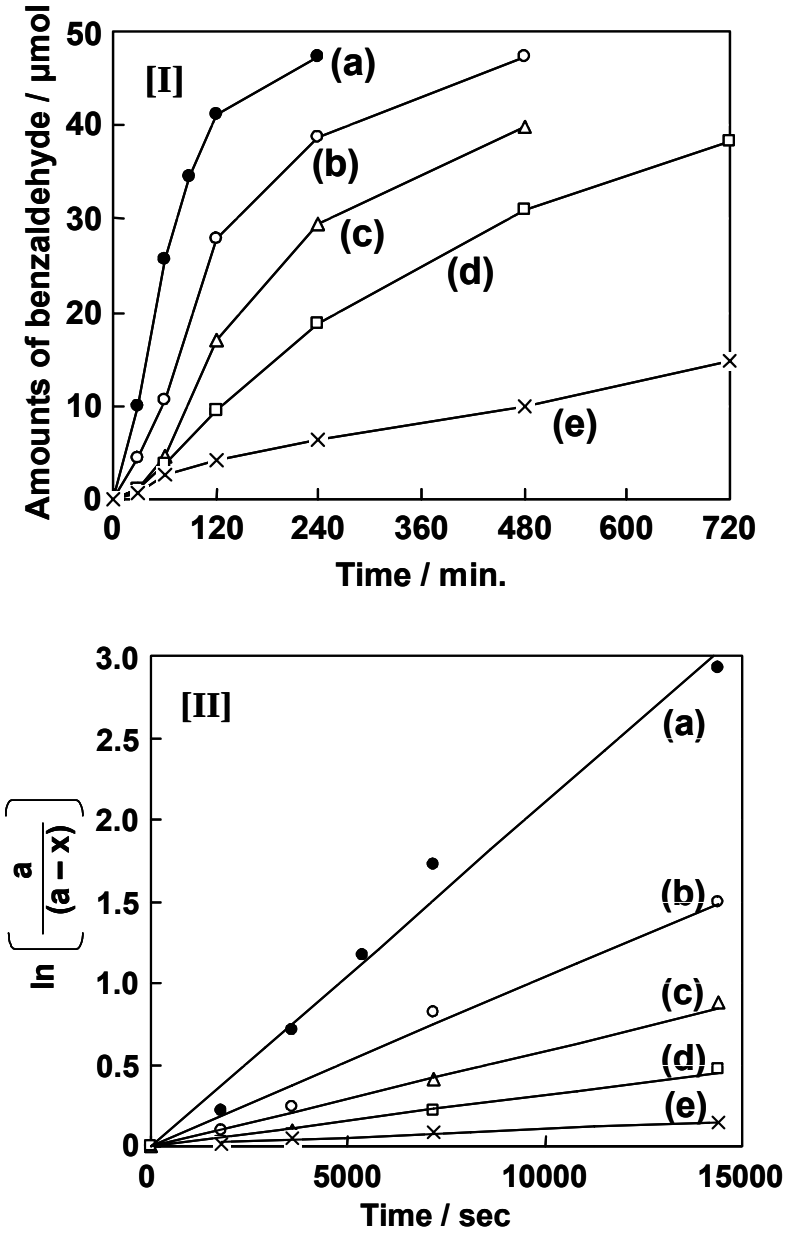

Figure 4.3. Photocatalytic oxidation of benzyl alcohol into benzaldehyde on TiO_2 (50 mg) under visible light irradiation [I] and the corresponding plots for ln{a / (a-x)} vs. t [II] on: (a) the un-treated TiO_2; (b) TiO_2(673); (c) TiO_2(773); (d) TiO_2(873); and (e) TiO_2(973). The initial amounts of benzyl alcohol and TiO_2 added to the reaction cell were 50 μmol and 50 mg, respectively.

Table 4.1. Physico-chemical properties and reaction rate constants for the TiO_2 photocatalysts as a function of the calcination temperature.

Photocatalysts	d / nm[a)]	S / m^2 g^{-1} [b)]	k / s^{-1} [c)]	uptakes / μmol [d)]
untreated TiO_2	7.3	320	2.1×10^{-4}	12.3
TiO_2 (673)	14.8	255	1.0×10^{-4}	7.2
TiO_2 (773)	15.8	158	5.8×10^{-5}	5.4
TiO_2 (873)	21.6	124	3.1×10^{-5}	3.6
TiO_2 (973)	23.7	91	1.0×10^{-5}	2.6

[a)] crystallite size (d), [b)] specific BET surface area (S), [c)] reaction rate constant (k) derived from Fig. 4.3 [II], and [d)] uptakes of benzyl alcohol within 1 h in the dark after benzyl alcohol (50 μmol) was added to an acetonitrile suspension involving TiO_2 (50 mg).

Meanwhile, the IR band of the TiO_2 without thermal treatment was observed at ca. 3750 ~ 3650 cm^{-1} due to the surface OH groups superimposed on a broad band at ca. 3700 ~ 2600 cm^{-1} attributed to the physisorbed H_2O [22-24]. Subsequently, the intensity of these bands was observed to decrease by calcination at high temperatures. It was previously reported that the thermal stability of the surface OH groups depend on the calcination temperature, i.e., the bridged OH groups bound to two other Ti sites are stable in air up to a temperature of 773 K, the terminal OH groups bound to one Ti^{4+} site are eliminated below 873 K; and the TiO_2 surface is fully de-hydrated at temperatures higher than 973 K [23, 24]. From these results, such physicho-chemical properties as BET surface area, particle size and the amount of surface OH groups of TiO_2 are considered to be associated with the adsorbility of benzyl alcohol in dark and the photocatalytic activity were discussed.

Effect of TiO_2 surface modification by treatment in HF solution

The photocatalytic activity for the oxidation of benzyl alcohol into benzaldehyde on HF-treated TiO_2 was investigated and the results are shown in Fig. 4.4. When HF-treated TiO_2 was used as a photocatalyst, the photocatalytic activity drastically decreased with the addition of HF, in particular, HF(110)-TiO_2 and HF(400)-TiO_2 exhibited negligible photocatalytic activity. It was also observed that the uptake of benzyl alcohol on TiO_2 decreased with an increase in HF under dark conditions while the uptake in HF(110)-TiO_2 and HF(400)-TiO_2 was half that on the untreated TiO_2, as shown in Fig. 4.4. Furthermore, the photocatalytic activity and uptakes of benzyl alcohol on NaOH-HF(400)-TiO_2 could be recovered up to ca. 80 % compared with untreated TiO_2.

In order to understand the surface state of HF-treated TiO_2, the surface composite was analyzed by XPS spectroscopy. As shown in Fig. 4.5, a peak at 683 - 685 eV of the binding energy due to F1s was observed on HF(400)-TiO_2, although it was not

observed on TiO_2. This peak is usually observed in surface-fluorinated TiO_2 systems as ≡Ti-F or $\equiv TiOF_2$ on a TiO_2 crystal surface [25]. It can, thus, be assumed that the surface OH groups of TiO_2 are modified by HF solution, partially to form ≡Ti-F or $\equiv TiOF_2$, leading to a decrease of the active OH groups. Furthermore, when HF(400)-TiO_2 was treated by NaOH solution, the peak intensity due to F1s decreased. These results indicate that the treatment of HF(400)-TiO_2 by NaOH solution caused a partial elimination of the fluoride ions, probably to re-generate the surface OH groups.

Interaction of the TiO_2 surface with benzyl alcohol for the selective photocatalytic oxidation reaction under visible light

The interaction between the TiO_2 surface and benzyl alcohol has been proposed here, as shown in Fig. 4.6: benzyl alcohol molecules can be adsorbed either on the Ti sites or OH sites. The absorption in the visible light region can be attributed to the charge transfer from benzyl alcohol to the Ti sites. Since the fluorinated surfaces of HF(110)-TiO_2 or HF(400)-TiO_2 do not participate in the photocatalytic activity in spite of the appearance of visible light absorption, the intrinsic surface OH groups interacting with benzyl alcohol were observed to play an important role in the photocatalytic oxidation of benzyl alcohol into benzaldehyde. As previously reported [19], the photo-excited surface complex does not produce benzaldehyde simply by the photo-induced holes but in combination with the assistance of O_2, which plays a significant role as electron acceptors. Thus, the reduction of O_2 by the photo-induced electrons leads to the production of H_2O and/or the surface OH groups on the TiO_2 surface. The interaction of benzyl alcohol with the Ti sites then leads to the absorption of visible light and its combination with the adjacent OH groups plays a significant role in the unique selective photocatalytic oxidation reaction of benzyl alcohol into benzaldehyde.

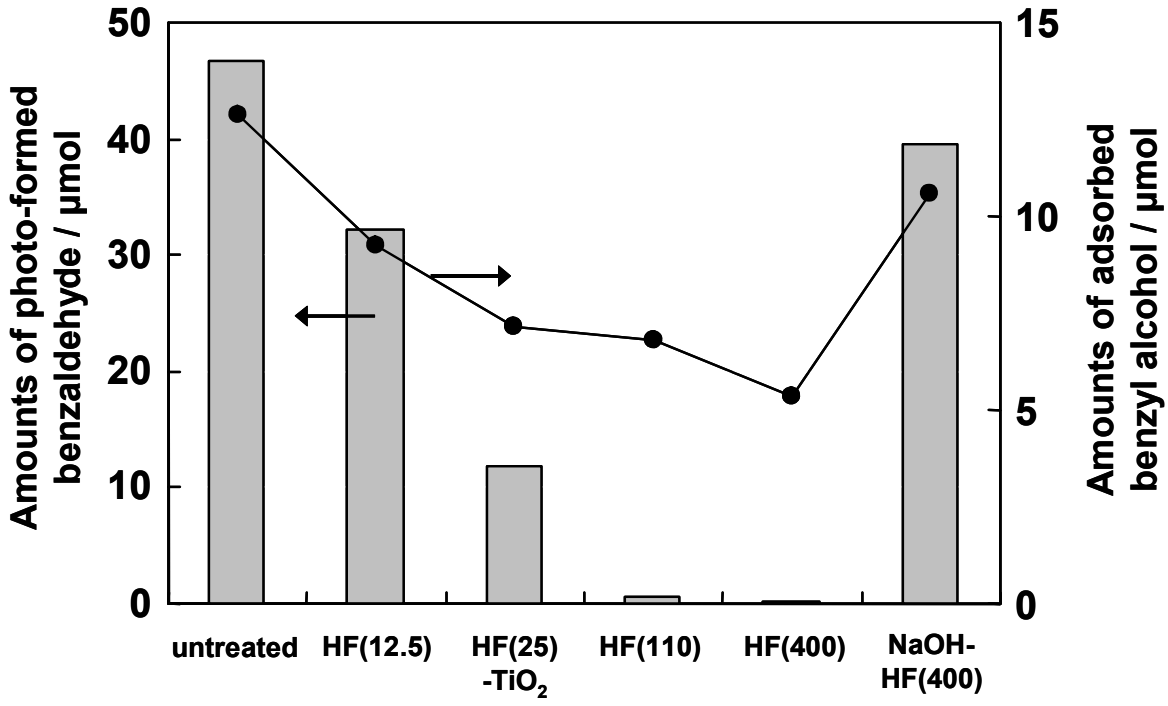

Figure 4.4. Amounts of photo-formed benzaldehyde for the photocatalytic oxidation of benzyl alcohol under 4 h visible light irradiation (gray bar); and uptakes of benzyl alcohol (●) within 1 h in the dark on untreated TiO_2; HF(x)-TiO_2 (x: 12.5, 25, 110, 400); and NaOH-HF(400)-TiO_2. Benzyl alcohol (50 μmol) was added to an acetonitrile suspension involving TiO_2 (50 mg).

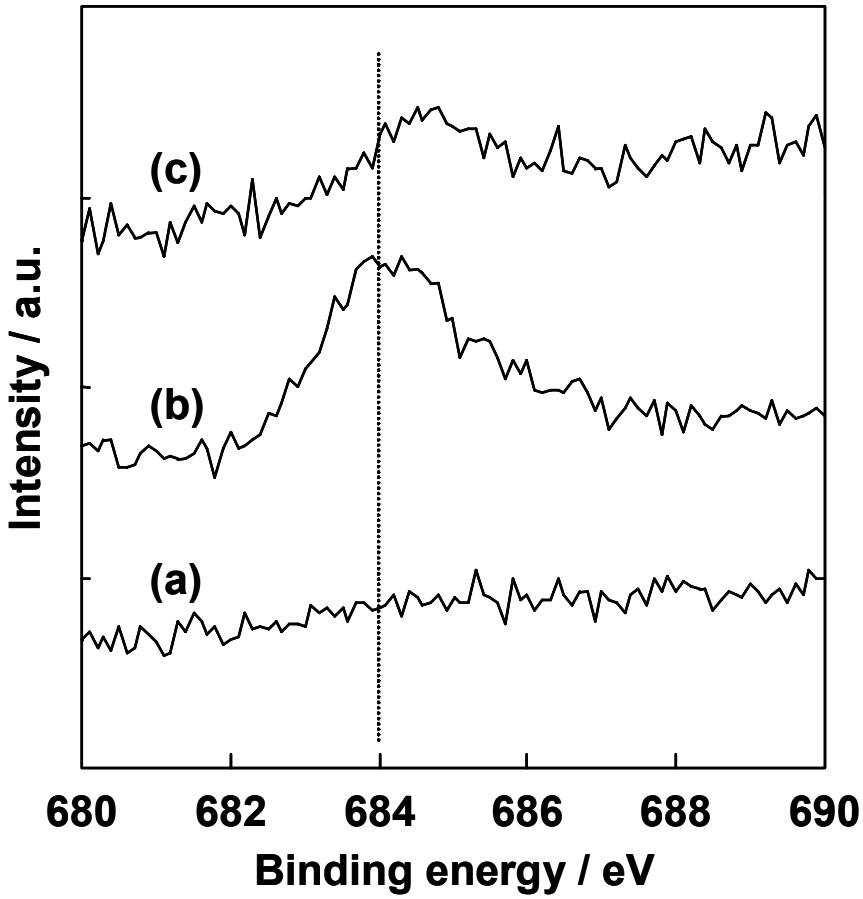

Figure 4.5. XPS spectra of the F 1s peaks of: (a) TiO_2; (b) HF(400)-TiO_2, and (c) NaOH-HF(400)-TiO_2.

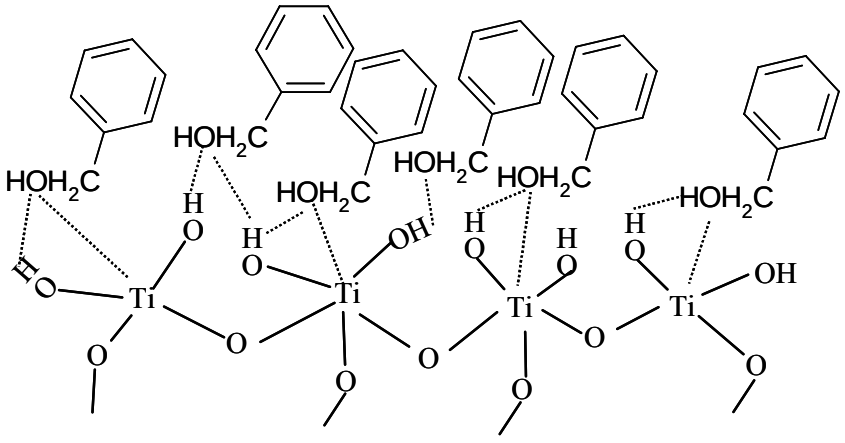

Figure 4.6. Proposed surface structures of benzyl alcohol adsorbed-TiO_2.

4.4. Conclusions

The selective photocatalytic oxidation of benzyl alcohol into benzaldehyde proceeded at a high conversion rate of > 99 % and high selectivity of > 99 % on TiO_2 in the presence of O_2 under visible light irradiation. It was confirmed that the surface complex formed by the interaction of benzyl alcohol with the coordinately unsaturated Ti sites of TiO_2 was essential for visible light absorption and its excitation to induce charge separation of the holes and electrons. Moreover, a combination of the assistance from the surface OH groups on TiO_2 was also vital for the selective photocatalytic oxidation of benzyl alcohol into benzaldehyde.

4.5. References

[1] M. Kitano, K. Iyatani, K. Tsujimaru, M. Matsuoka, M. Takeuchi, M. Ueshima, J.M. Thomas, M. Anpo, *Top. Catal.*, **49**, 24 (2008).

[2] M. Grätzel, *J. Photochem. Photobiol. C: Photochem. Rev.*, **4**, 145 **(**2003).

[3] A. Fujishima, T.N. Rao, D.A. Tryk, *J. Photochem. Photobiol. C: Photochem. Rev.*, **1**, 1 (2000).

[4] M.A. Fox, M.T. Dulay, *Chem. Rev.* , **93**, 341 (1993).

[5] J. Chen, D.F. Ollis, W.H. Rulkens, H. Bruning, *Water Research*, **33**,669 (1998).

[6] D.S. Muggli, J.T. Mccue, J.L. Falconer, *J. Catal.*, **173**, 470 (1998).

[7] J.L. Falconer, K.A. Magrini-Bair, *J. Catal.*, **179**, 171 (1998).

[8] F.H. Hussein, G. Pattenden, R. Rudham, J.J. Russell, *Tetrahedron Lett.*, **25**, 3363 (1984).

[9] U.R. Pillai, E. Sahle-Demessie, *J. Catal.*, 211, 434 (2002).

[10] O.S. Mohamed, A.E.M. Gaber, A.A. Abdel-Wahab, *J. Photochem. Photobiol. A*, **148**, 205 (2002).

[11] S. Farhadi, M. Afshari, M. Maleki, Z. Badazadeh, *Tetrahedron Lett.*, **46**, 8483 (2005).

[12] S. Yurdakal, G. Palmisano, V. Loddo, V. Augugliaro, L. Palmisano, *J. Am. Chem. Soc.*, **130**, 1568 (2008).

[13] V. Augugliaro, T. Caronna, V. Loddo, G. Marci, G. Palmisano, L. Palmisano, S. Yurdakal, *Chem. Eur. J.*, **14**, 4640 (2008).

[14] G. Palmisano, S. Yurdakal, V. Augugliaro, V. Loddo, L. Palmisano, *Adv. Synth. Catal.*, **349**, 964 (2007).

[15] G. Palmisano, M. Addamo, V. Augugliaro, T. Caronna, E. Garcia-Lopez, V. Loddo, L. Palmisano, *Chem. Commun.*, 1012 (2006).

[16] M. Addamo, V. Augugliaro, M. Bellardita, A.D. Paola, V. Loddo, G. Palmisano, L. Palmisano, S. Yurdakal, *Catal. Lett.*, 126, 58 (2008).

[17] T. Ohuchi, T. Miyatake, Y. Hitomi, T. Tanaka, *Catal. Today*, 120, 233 (2007).

[18] T. Shishido, T. Miyatake, K. Teramura, Y. Hitomi, H. Yamashita, T. Tanaka, *J. Phys. Chem. C*, **113**, 18713 (2009).

[19] S. Higashimoto, N. Kitao, N. Yoshida, T. Sakura, M. Azuma, H. Ohue, Y. Sakata, *J. Catal.*, **266**, 279 (2009).

[20] Y. Wang, K. Hang, N.A. Anderson, T. Lian, *J. Phys. Chem. B*, **107**, 9434 (2003).

[21] T. Tachikawa, S. Tojo, M. Fujitsuka, T. Majima, *Langmuir*, **20**, 2753 (2004).

[22] M. Takeuchi, L. Bertinetti, G. Martra, S. Coluccia, M. Anpo, *Appl. Catal. A: Gen.*, **307**, 13 (2006).

[23] A.Y. Nosaka, J. Nishino, T. Fujiwara, T. Ikegami, H. Yagi, H. Akutsu, Y. Nosaka, *J. Phys. Chem. B*, **110**, 8380 (2006).

[24] G.D. Parfitt, *Prog. Surf. Membr. Sci.*, **11**, 181 (1976).

[25] H.G. Yang, C.H. Sun, S.Z. Qiao, J. Zou, G. Liu, S.C. Smith, H.M. Cheng, G.Q. Lu, *Nature*, **453**, 638 (2008).

Chapter 5

Preparation and Characterization of Single-Site Heterogeneous Catalysts and Their Photocatalytic Reactivity

5.1. Preparation and Characterization of Ti-, V-, Cr-oxide Containing Zeolite and Their Photocatalytic Reactivity

5.1.1. Introduction

One of the most important challenges facing scientists today is discovering way to utilize clean and abundant solar energy and convert it into useful chemical energy, especially for applications in environmentally friendly catalysts that can reduce toxic pollutants in the atmosphere and water as well as for the production of clean energy resources. To address such concerns, the development of various types of semiconducting bulk photocatalysts have been intensively carried out with such successful results as the elimination of NOx in air [1,2], the degradation of toxic organic pollutants diluted in water [3,4], and the decomposition of water into H_2 and O_2 by separate evolution [5,6]. In addition to these semiconducting bulk photocatalysts, the unique photocatalytic properties of single-site catalysts constructed on various support surfaces such as SiO_2 as well as within zeolites frameworks or cavities by impregnation, grafting or anchoring methods and the hydrothermal synthesis of transition metal oxide-incorporated zeolites also have the potential for many new applications in photofunctional systems [7–32].

As shown in Eq. (1), highly dispersed and isolated transition metal oxides, such as Ti, V, Mo, and Fe, can be excited under UV or visible light (or sunlight) irradiation for Cr-oxides to form corresponding charge-transfer excited states involving an electron transfer from O^{2-}(l) to $M^{n+}{}_{(l)}$:

$$[M^{n+} - O^{2-}]_{(l)} \xrightarrow{h\nu} [M^{(n-1)+}\text{-}O^{-}]^{*}_{(l)} \qquad (M : Ti, V, Cr, Mo,\ldots) \qquad (1)$$

The high reactivity and selectivity of these charge-transfer excited states formed on single-site heterogeneous catalysts, in which the electron–hole pair states are localized in close proximity, led to such significant photocatalytic reactions as the decomposition of NOx (NO and N_2O) into N_2 and O_2 [9–16,20], the partial oxidation of hydrocarbons

with O_2 or NO [9–16,24,25], the degradation of organic pollutants dissolved in water [33–35], and the reduction of CO_2 with H_2O to produce CH_4 and CH_3OH [9–19]. This is in stark contrast to semiconducting bulk photocatalysts in which the photo-formed electrons and holes have large distant spaces between them (charge separation), thus, leading to different reaction mechanisms. These findings indicate that a fundamental understanding of the coordination structure and electronic state of the active surface species, as well as the bulk crystalline structure and electronic properties, is important in the design of applicable photocatalytic systems having high reactivity and selectivity.

In the present paper, the photocatalytic reactivities of various single-site transition metal oxide photocatalyst species such as Ti, V, Mo and Cr have been summarized. The local structures of these single-site oxides are discussed based on results obtained by various in situ spectroscopic techniques. Special attention has been focused on the relationship between the local structures of the single-site catalysts and their photocatalytic reactivity and selectivity for various photocatalytic reactions.

5.1.2. Experimental

Preparation of single-site photocatalysts

A Ti-oxide/Y-zeolite (1.1 wt.% as TiO_2) was prepared by ion-exchange with an aqueous titanium ammonium oxalate solution using a Y-zeolite sample (SiO_2/Al_2O_3 = 5.5) (ex-Ti-oxide/Y-zeolite). Mo-MCM-41 with 1.0 and 4.0 wt.% as Mo were synthesized using tetraethylorthosilicate and $(NH_4)_6Mo_7O_{24}\cdot 4H_2O$ as the starting materials and cetyltrimethylammonium bromide as the structure directing agent.

Characterization of single-site photocataltsts

The diffuse reflectance UV-vis spectra were recorded at 298 K with a Shimazu UV-2200A double-beam digital spectrophotometer. The XAFS (XANES and

EXAFS) spectra were obtained at the BL10B and BL-01B1 facility of the High Energy Acceleration Organization (KEK) in Tsukuba and SPring-8 at the Japan Synchrotron Radiation Research Institute (JASRI). The ESR (Electron Spin Resonance) spectra were recorded with a JEOL-2X spectrometer (X-band) at 77 K. The FT-IR spectra were recorded at room temperature with a FT-IR spectrometer (JASCO FT-IR 660 Plus) with self-supporting pellets of the samples in the transmission mode. The photoluminescence spectra were measured at 298 K with a SPEX Fluorolog-3 spectrofluorometer. Photocatalytic reactions were carried out in a closed system using a quartz reactor (reaction volume: 101 cm^3) under UV irradiation at 293 K with a 100 W high-pressure mercury lamp (Toshiba SHL-100UVQ-2) through a water filter. The amount of the catalyst used for the photocatalytic reactions was fixed at 50 mg. The reaction products were analyzed by on-line gas chromatography.

5.1.3. Results and Discussion

5.1.3.1. Photocatalytic reactivity of Ti-oxide species constructed within zeolite cavities

In the use of solar energy through chemical storage, the design of highly efficient and selective photocatalytic systems that work without any loss is of vital interest. In particular, the development of efficient photocatalytic systems that are able to decompose NO directly into N_2 and O_2 or to reduce CO_2 with H_2O into chemically valuable compounds such as CH_4 or CH_3OH is one of the most desired and challenging goals in the research of environmentally friendly catalysts [9−16]. We have reported that these photocatalytic reactions were successfully able to proceed on powdered TiO_2 at room temperature [36,37]. Using various types of well-characterized powdered TiO_2 catalysts, the effect of the structure on the catalytic activity was investigated. Extremely small TiO_2 particles having large band gaps were found to show the highest

reactivity [36]. At the same time, the activity of the highly dispersed Ti-oxide species anchored onto silica glass or zeolites was also investigated [9−19] and it was found that the highly dispersed Ti-oxide species exhibits unique and high photocatalytic reactivity as compared to bulk TiO_2 powdered catalysts. The formation of N_2 and O_2 in the decomposition of NO as well as the formation of CH_3OH in the reduction of CO_2 with H_2O were observed and the product selectivity increased as the extent of the dispersion of the Ti-oxide species became higher [9−19]. These results indicate that by using zeolites as supports, highly dispersed Ti-oxides species can be produced, leading to the development of environmentally friendly photocatalytic systems having high catalytic efficiency, selectivity and other fascinating properties such as shape selectivity and a reactant gas condensation effect, which can be derived from the physicochemical properties of the zeolites.

Photocatalytic reduction of CO_2 with H_2O on Ti-oxide single-site catalysts constructed within zeolite cavities

A Ti-oxide/Y-zeolite (1.1 wt.% as TiO_2) was prepared by ion-exchange with an aqueous titanium ammonium oxalate solution using a Y-zeolite sample (SiO_2/Al_2O_3 = 5.5) (ex-Ti-oxide/Y-zeolite). The Pt-loaded ex-Ti-oxide/Y-zeolite (1.0 wt.% as Pt) was prepared by impregnation with an aqueous solution of H_2PtCl_6. Ti-oxide/Y-zeolites having different Ti contents (1.0 and 10 wt.% as TiO_2) were prepared by impregnating the Y-zeolite with an aqueous solution of titanium ammonium oxalate (imp-Ti-oxide/Yzeolite). UV-irradiation of powdered TiO_2 and the Ti-oxide/Y-zeolite catalysts prepared by ion-exchange or impregnation methods in the presence of a mixture of CO_2 and H_2O led to the evolution of CH_4 and CH_3OH in the gas phase at 328 K as well as trace amounts of CO, C_2H_4 and C_2H_6. The evolution of small amounts of O_2 was also observed. As shown in Fig. 5.1.1, the yields of these photo-formed products increased linearly as a function of the UV-irradiation time and the reaction

immediately ceased when irradiation was discontinued, indicating the reduction of CO_2 with H_2O on the catalysts was photocatalytic. The specific photocatalytic reactivities for the formation of CH_4 and CH_3OH are shown in Fig. 5.1.2. It is clear that the photocatalytic reaction rate and selectivity for the formation of CH_3OH depend strongly on the type of catalyst. It can also be seen that the specific photocatalytic reactivities of the Ti-oxide/Y-zeolite catalysts, which have been normalized by unit gram of Ti in the catalysts, are much higher than bulk TiO_2. The ex-Ti-oxide/Y-zeolite exhibits a high reactivity and selectivity for the formation of CH_3OH, while the formation of CH_4 was found to be the major reaction on bulk TiO_2 as well as on the imp-Ti-oxide/Y-zeolite.

The ex-Ti-oxide/Y-zeolite exhibited an intense single pre-edge peak, indicating that the Ti-oxide species exists in tetrahedral coordination [17,20]. On the other hand, the imp-Ti-oxide/Y-zeolite exhibited three characteristic weak pre-edge peaks attributed to the crystalline anatase TiO_2. Curve-fitting analysis of the EXAFS spectra showed that the ex-Ti-oxide/Y-zeolite catalyst consists of 4-coordinate titanium ions with a coordination number (N) of 3.7 and an atomic distance (R) of 1.78 Å. On the other hand, the imp-Ti-oxide/Y-zeolite catalysts exhibited an intense peak at around 2.7 Å assigned to the neighboring titanium atoms (Ti–O–Ti), indicating the aggregation of the Ti-oxide species in these catalysts.

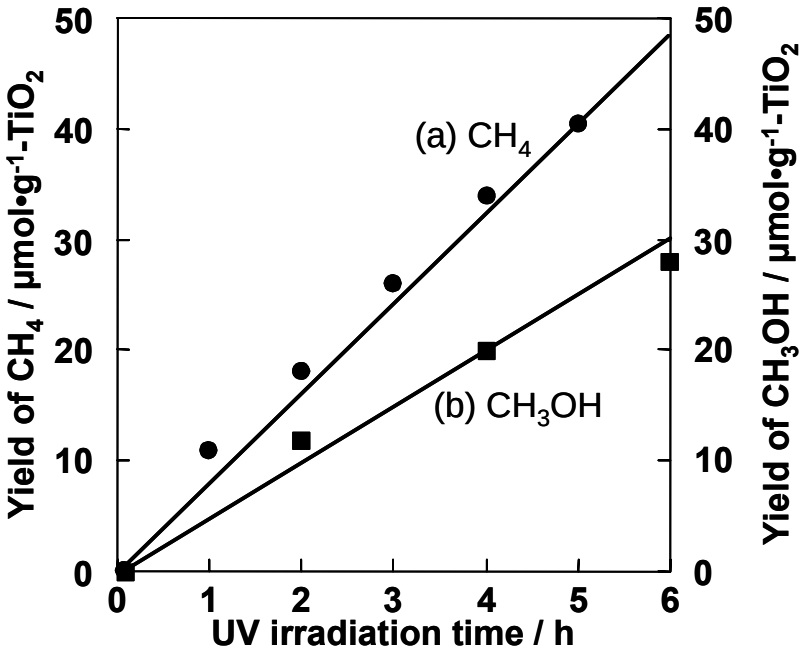

Figure 5.1.1. The reaction-time profiles of the photocatalytic reaction of CO_2 with H_2O to produce CH_4 (a) and CH_3OH (b) on the ex-Ti-oxide/Y-zeolite catalysts.

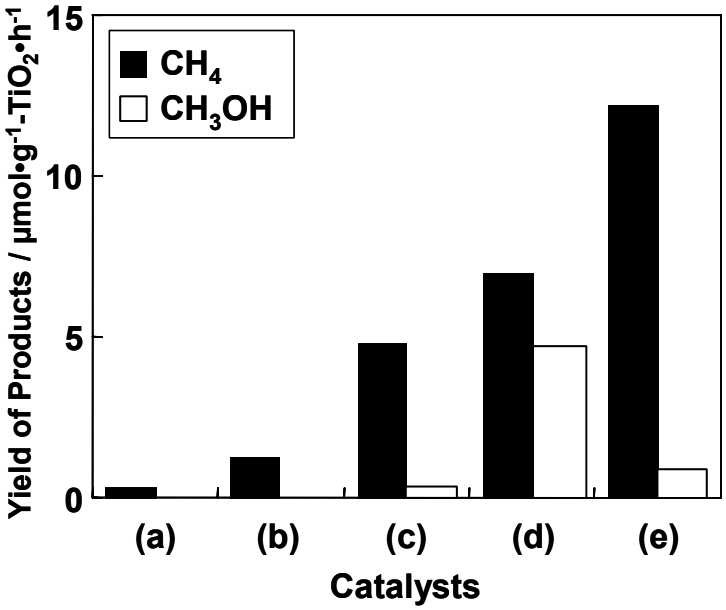

Figure 5.1.2. The product distribution of the photocatalytic reduction of CO_2 with H_2O on anatase TiO_2 powder (a), the imp-Ti-oxide/Y-zeolite (10 wt.% as TiO_2) (b), the imp-Ti-oxide/Y-zeolite (1.0 wt.% as TiO_2) (c), the ex-Ti-oxide/Y-zeolite (1.1 wt.% as TiO_2) (d) and the Pt-loaded ex-Ti-oxide/Y-zeolite (e) catalysts.

The ex-Ti-oxide/Y-zeolite catalyst exhibited a photoluminescence spectrum at around 490 nm by excitation at around 290 nm at 77 K. The observed photoluminescence and absorption bands are in good agreement with those previously observed with the highly dispersed tetrahedrally coordinated Ti-oxide species prepared in silica matrices [17–20]. It could, therefore, be concluded that the photoluminescence spectrum is attributed to the radiative decay process from the charge-transfer excited state to the ground state of the highly dispersed Ti-oxide species in tetrahedral coordination, as shown below:

$$(Ti^{4+} - O^{2-}) \underset{hv'}{\overset{hv}{\rightleftharpoons}} (Ti^{3+} - O^{-})^{*}$$

On the other hand, the imp-Ti-oxide/Y-zeolite catalysts did not exhibit any photoluminescence. These results clearly indicate that the ex-Ti-oxide/Y-zeolite catalyst consists of a highly dispersed isolated tetrahedral Ti-oxide species while the imp-Ti-oxide/Y-zeolite catalysts involve an aggregated octahedral Ti oxide species which do not exhibit any photoluminescence spectra.

The addition of H_2O or CO_2 molecules to the ex-Ti-oxide/Y-zeolite catalyst led to an efficient quenching of the photoluminescence. The lifetime of the charge-transfer excited state was also found to be shortened by the addition of CO_2 or H_2O, its extent depending on the amount of added gasses. Such an efficient quenching of the photoluminescence with CO_2 or H_2O suggests not only that the tetrahedrally coordinated Ti-oxide species is located at positions accessible to the added CO_2 or H_2O but also that the added CO_2 or H_2O interacts and/or reacts with the Ti-oxide species in both its ground and excited states. UV-irradiation of the anchored Ti-oxide catalyst in the presence of CO_2 and H_2O at 77 K led to the appearance of ESR signals due to the Ti^{3+} ions, H atoms, and carbon radicals [17,37]. From these results, the reaction mechanism in the photocatalytic reduction of CO_2 with H_2O on the highly dispersed Ti-oxide catalyst can be proposed as follows: CO_2 and H_2O molecules interact with the

excited state of the photoinduced $(Ti^{3+}–O^{-})^*$ species and the reduction of CO_2 and the decomposition of H_2O proceed competitively. Furthermore, H atoms and OH· radicals are formed from H_2O and react with the carbon species formed from CO_2 to produce CH_4 and CH_3OH.

The addition of CO_2 or H_2O to these zeolites resulted in a significant quenching of the photoluminescence, indicating the excellent accessibility of the Ti-oxide species to CO_2 and H_2O. In addition, quenching with H_2O was observed to be much more effective than with CO_2, reflecting the stronger interaction of H_2O with the Ti-oxide species [17–20]. UV-irradiation of the Ti mesoporous zeolites and the TS-1 zeolite in the presence of CO_2 and H_2O also led to the formation of CH_3OH and CH_4 as the main products. It was found that Ti-MCM-48 exhibited much higher reactivity than either TS-1 or Ti-MCM-41. Besides the higher dispersion state of the Ti-oxide species, the other distinguishing features of these zeolite catalysts are: TS-1 has a smaller pore size (ca. 5.7 Å) and a three-dimensional channel structure; Ti-MCM-41 has a large pore size (>20 Å) but one-dimensional channel structure; and Ti-MCM-48 has both a large pore size (>20 Å) and three-dimensional channels. The higher reactivity and selectivity for the formation of CH_3OH observed with the Ti-MCM-48 zeolite than with the other catalysts may, thus, be due to the combined contribution of the high dispersion state of the Ti oxide species and the large pore size having a three-dimensional channel structure. These results strongly indicate that mesoporous zeolites with highly dispersed Ti-oxide species in their framework are promising candidates to act as effective photocatalysts for the reduction of CO_2 with H_2O [15–20].

The effect of Pt-loading on the photocatalytic reactivity of Ti-containing zeolites has also been investigated. Although the addition of Pt onto Ti-containing zeolites was seen to be effective in increasing the photocatalytic reactivity, only the formation of CH_4 was promoted accompanied by a decrease in the CH_3OH yields. The absorption spectra of the Pt-loaded catalysts were the same as those observed with the original Ti-

containing zeolite without Pt loading. The Pt-loaded catalyst also exhibited the same pre-edge peak in the XANES spectra and the same Ti–O bonding peak in the FT-EXAFS spectra as those of the original Ti-containing zeolite. Moreover, Pt-loading on the Ti-containing zeolite catalyst led to an efficient quenching of the photoluminescence accompanied by a shortening of its lifetime. Since the results of XAFS and absorption measurements indicated that the local structure of the Ti-oxide species dispersed in the zeolite was not altered by Pt loading, the effective quenching of the photoluminescence can be attributed to the electron transfer from the photo-excited Ti-oxide species to the metallic Pt which exists in the neighborhood of the Ti-oxide species. The electrons are easily transferred from the charge-transfer excited state of the Ti-oxide species, the electron–hole pair state of $(Ti^{3+}–O^{-})^{*}$, to the Pt moieties while the holes remain in the Ti-oxide species, resulting in the charge separation of the electrons and holes from the photo-formed electron–hole pair states. As a result, on the Pt-loaded Ti-containing zeolite catalyst, photocatalytic reactions that proceed in the same manner as on bulk TiO_2 catalysts became predominant and the reduction reaction by electrons and the oxidation reaction by holes occurred separately on different sites, leading to the selective formation of CH_4.

Photocatalytic decomposition of NO into N_2 and O_2 on the Ti-oxide single-site catalyst constructed within Y-zeolite cavities

The Ti-oxide/Y-zeolite (1.1 wt.% as TiO_2) was prepared by ion-exchange with an aqueous titanium ammonium oxalate solution using Y-zeolite samples (SiO_2/Al_2O_3 = 5.5) (ex-Ti-oxide/Y-zeolite). Ti-oxide/Y-zeolites having different Ti contents (1.0 and 10 wt.% as TiO_2) were prepared by impregnating the Y-zeolite with an aqueous solution of titanium ammonium oxalate (imp-Ti-oxide/Y-zeolite).

UV-irradiation of the powdered TiO_2 and the Ti-oxide/Y-zeolite catalysts prepared by ion-exchange or impregnation methods in the presence of NO were found to lead to

the evolution of N_2, O_2 and N_2O in the gas phase at 275 K with different yields and different product selectivity [14–16,20]. The yields of these photo-formed N_2, O_2 and N_2O increased linearly with the UV-irradiation time and the reaction immediately ceased when irradiation was discontinued, as shown in Fig. 5.1.3, indicating that the presence of a Ti-oxide species included within the zeolites as well as UV-irradiation light are indispensable for the photocatalytic reaction to take place. The direct decomposition of NO to produce N_2, O_2 and N_2O thus occurs photocatalytically on the surface of the Ti-oxide single-site catalyst.

The photocatalytic reactivities of various Ti-oxide catalysts for the direct decomposition of NO are shown in Table 5.1.1. Of special interest is the comparison of the photocatalytic activities of the Ti-oxide/Y-zeolite catalysts with that of the widely used bulk TiO_2 powdered catalyst. It can be seen that the specific photocatalytic reactivities of the Ti-oxide/Y-zeolite catalysts, which have been normalized for the unit amount of TiO_2 in the catalysts, are much higher than that for the bulk TiO_2 catalysts [14–16, 20].

Table 5.1.1 also shows the yields of the photo-formed N_2 and N_2O (efficiency) and their distribution (selectivity) in the photocatalytic decomposition of NO on various types of Ti-oxide catalysts. From Table 5.1.1, it is clear that the efficiency and selectivity for the formation of N_2 depend strongly on the type of catalyst. The ex-Ti-oxide/Y-zeolite catalyst exhibits a high reactivity and selectivity for the formation of N_2, while the formation of N_2O was found to be the major reaction on the bulk TiO_2 catalyst as well as on the imp-Ti-oxide/Y-zeolite catalyst. Thus, the results obtained with the ex-Ti-oxide/Y-zeolite clearly show the large difference in selectivity as well as efficiency between the imp-Ti-oxide/Y-zeolite and bulk TiO_2 catalyst [14–16,20].

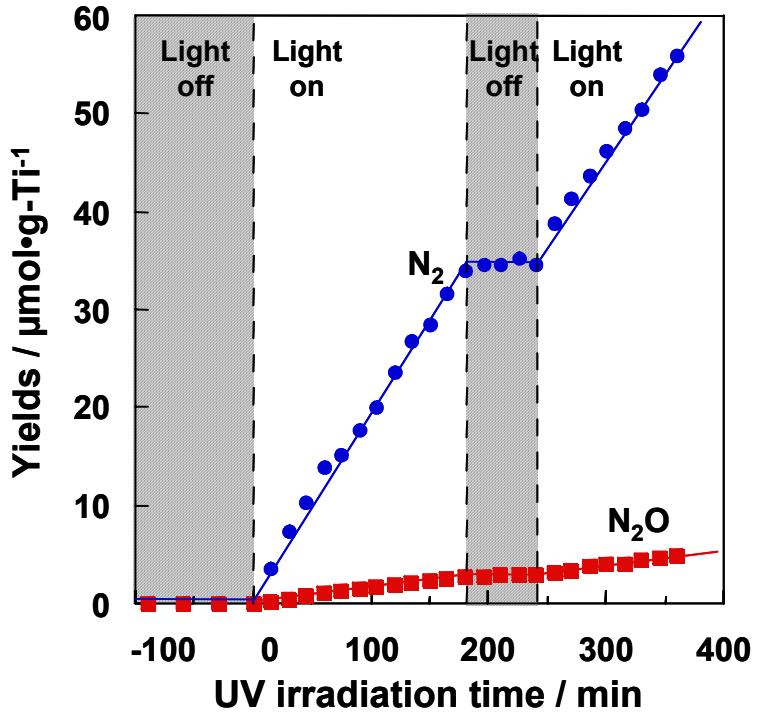

Figure 5.1.3. Reaction time profiles of the photocatalytic decomposition of NO into N_2 and N_2O on the ex-Ti-oxide/Y-zeolite.

Table 5.1.1. Yields of the photo-formed products, N_2 and N_2O in the photocatalytic decomposition of NO at 275 K and their distribution on various Ti-based photocatalysts.

Catalysts	Ti content (wt.% as TiO_2)	Yields (µmol/g of TiO_2 h)			Selectivity (%)	
		N_2	N_2O	Total	N_2	N_2O
ex-Ti-oxide/Y-zeolite	1.1	14	1	15	91	9
imp-Ti-oxide/Y-zeolite	1.0	7	10	17	41	59
imp-Ti-oxide/Y-zeolite	10	5	22	27	19	81
TiO_2 powder		2	6	8	25	75

XAFS (XANES and EXAFS) investigations of Ti-oxide catalysts at the Ti K-edge were carried out and it was revealed that the Ti-oxide species has a tetrahedral coordination for the ex-Ti-oxide/Y-zeolite catalyst while, for the imp-Ti-oxide/Y-zeolite catalyst, the Ti-oxide species had a octahedral coordination. Moreover, the relationship between the coordination number of the Ti-oxide species and the selectivity for N_2 formation in the photocatalytic decomposition of NO on various types of Ti-oxide based photocatalysts are shown in Fig. 5.1.4. A clear dependence of the N_2 selectivity on the coordination number of the Ti-oxide species can be observed, i.e., the lower the coordination number of the Ti-oxide species, the higher the N_2 selectivity. From these results, it can be proposed that a highly efficient, highly selective photocatalytic reduction of NO into N_2 and O_2 can be achieved using the ex-Ti-oxide/Y-zeolite, which includes the highly dispersed isolated tetrahedral Ti-oxide as the active species. Also, the formation of N_2O as the major product was observed for the bulk TiO_2 catalysts and on the imp-Ti-oxide/Y-zeolite catalysts, which include the aggregated octahedrally coordinated Ti-oxide species.

Photoluminescence investigations of the ex-Ti-oxide/Y-zeolite catalyst were also carried out and a photoluminescence spectrum at around 490 nm by excitation at around 290 nm at 77 K due to the highly dispersed tetrahedrally coordinated Ti-oxide species was observed, as shown in Fig. 5.1.5. However, no photoluminescence spectrum could be observed for the imp-Ti-oxide/Y-zeolite catalysts. The addition of NO onto the ex-Ti-oxide/Y-zeolite catalyst led to an efficient quenching of the photoluminescence spectrum and the lifetime of the charge-transfer excited state was also found to be shortened, its extent depending on the amount of NO added. These results indicate not only that the tetrahedrally coordinated Ti-oxide species may be located at positions accessible to the added NO but also that the added NO easily interacts with the charge-transfer excited state of the species [14–16,20].

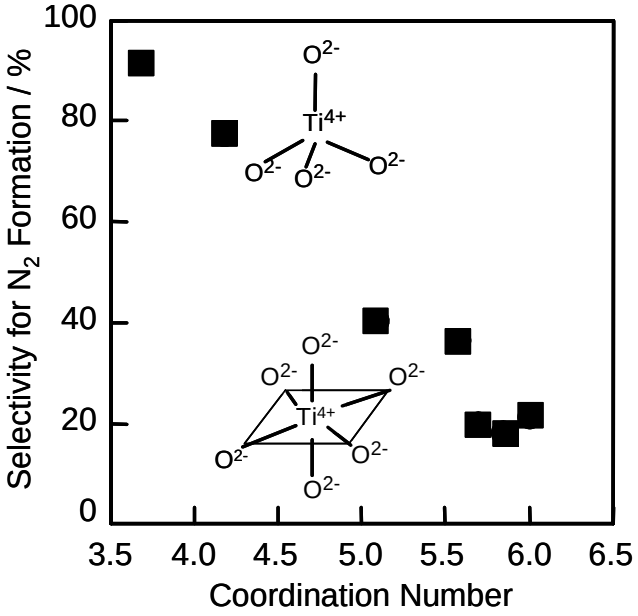

Figure 5.1.4. Relationship between the coordination number of Ti-oxide species and the selectivity for N_2 formation in the photocatalytic decomposition of NO on various titanium oxide photocatalysts.

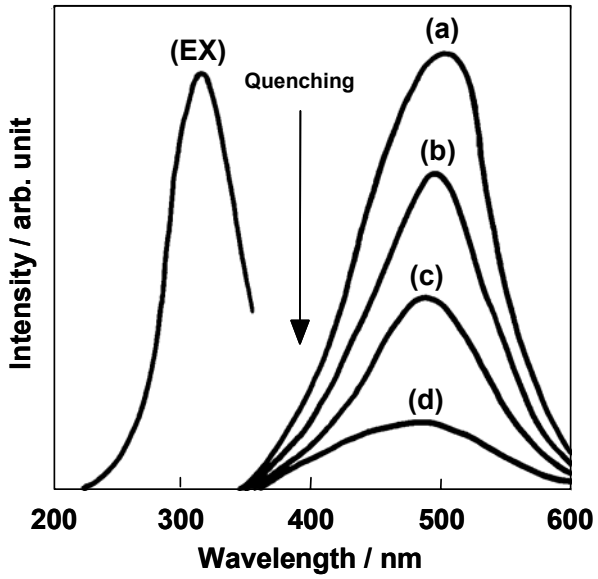

Figure 5.1.5. Observed photoluminescence spectrum of (a) the ex-Ti-oxide/Y-zeolite catalyst, (EX) its excitation spectrum, (b, c) the effect of the addition of CO_2 and H_2O, and (d) and the loading of Pt on the photoluminescence spectrum at 77 K. Excitation at 290 nm, emission monitored at 490 nm, amounts of added CO_2: (b) 8.5, and H_2O; (c) 2.9 μmol g^{-1}.

Based on these results, the reaction mechanism for the photocatalytic decomposition of NO on the isolated tetrahedral Ti-oxide species was proposed, as shown in Scheme 5.1.1. The NO species was able to adsorb onto these oxide species as weak ligands to form the reaction precursors. Under UV-irradiation, the charge-transfer excited complexes of the oxides, $(Ti^{3+}–O^{–})^{*}$, are formed. Within their lifetimes, the electron transfer from the trapped electron center, Ti^{3+}, into the π-antibonding orbital of NO takes place and, simultaneously, the electron transfer from the π -bonding orbital of another NO into the trapped hole center, $O^{–}$, occurs. These electron transfers led to the direct decomposition of two sets of NO on $(Ti^{3+}–O^{–})^{*}$ into N_2 and O_2 under UV-irradiation in the presence of NO even at 275 K. On the other hand, with the aggregated or bulk TiO_2 catalysts, the photo-formed holes and electrons rapidly separate from each other with large space distances between the holes and electrons, thus, preventing the simultaneous activation of two NO on the same active sites and resulting in the formation of N_2O and NO_2 in place of N_2 and O_2. Moreover, the decomposed N and O species react with NO on different sites to form N_2O and NO_2, respectively.

These results clearly demonstrate that zeolites used as supports enable the construction of the Ti-oxide species in a highly dispersed state within the zeolite cavities, thus, such tetrahedrally coordinated Ti-oxide photocatalysts can be seen to be promising candidates for unique and applicable photocatalysts for the reduction of toxic NOx compounds.

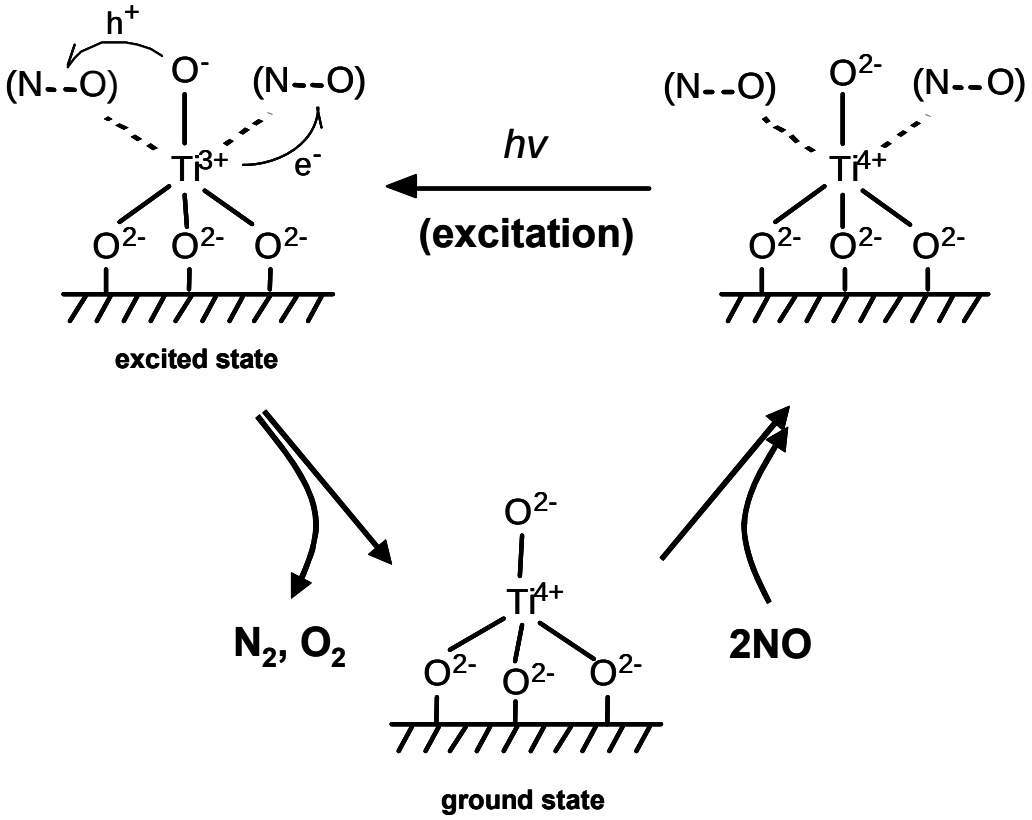

Scheme 5.1.1. Reaction scheme of the photocatalytic decomposition of NO into N_2 and O_2 on the Ti-oxide/Y-zeolite catalyst at 275 K.

Design of visible light-responsive Ti/zeolite catalysts by applying an advanced metal ion implantation method

Titanium oxide photocatalysts anchored within various zeolites exhibit unique and high photocatalytic activity, however, the isolated tetrahedral Ti-oxide species absorbs UV light of wavelengths below 300 nm. Photocatalysts which can operate efficiently under both UV and visible light are urgently required for practical and widespread use. A modification of the electronic properties of Ti/zeolite photocatalysts by bombarding them with high-energy metal ions has led to the discovery that metal ion-implantation with various transition-metal ions such as V or Cr accelerated by high electric fields can produce a large shift in the absorption band toward visible light regions [10]. Ti-HMS and Ti-MCM-41 exhibit their absorption spectra at around 200–260 nm which can be attributed to the charge-transfer absorption process involving an electron transfer from the O^{2-} to Ti^{4+} ion of the highly dispersed tetrahedrally coordinated Ti-oxide species of these catalysts [10]. However, V ion-implantation on Ti-HMS and Ti-MCM-41 lead to a large shift in their absorption spectra toward visible light regions, the extent strongly depending on the amount of V ions implanted. These results indicate that the interaction of the implanted V ions with the tetrahedrally coordinated Ti-oxide species lead to a modification of the electronic properties of the Ti-oxide species within the zeolite framework, enabling them to absorb visible light. The photocatalytic activity of the V ion-implanted Ti-HMS and Ti-MCM-41 was also investigated for the decomposition of NO into N_2 and O_2 under visible light irradiation ($\lambda > 420$ nm). Visible light irradiation of the V ion-implanted Ti-HMS led to the efficient decomposition of NO into N_2 and O_2, while the unimplanted original Ti-HMS exhibited no activity for the reaction under the same conditions [10]. These results show that ion-implantation is an effective technique for the modification of the electronic properties of titanium oxide photocatalysts, enabling them to absorb and operate under visible light ($\lambda > 420$ nm) with high efficiency.

The local environment of the implanted metal ions was investigated by XANES and EXAFS (XAFS) analyses [10]. The V K-edge FT-EXAFS spectra of the Ti-HMS catalyst implanted with V ions show that the next-neighbors of the V environment are not the same as the vanadium-oxide based catalysts (e.g., V_2O_5) and suggest the formation of tetrahedral titanium oxides having a V–O–Ti bond instead of V–O–V linkage [10]. These findings show that the formation of the V–O–Ti bridge structures between the isolated tetrahedrally coordinated Ti-oxide species and implanted V ions affect the electronic structure of the isolated Ti-oxide species, leading to a red shift in the absorption spectra of these catalysts.

It has also been recently reported that the Ti^{4+}–O–Ce^{3+} linkage constructed within MCM-41 (Ti/Ce-MCM-41) exhibits photocatalytic activity for the oxidation of 2-propanol into acetone or CO_2 under visible light irradiation (λ = 460 nm) [38]. The Ti^{4+}–O–Ce^{3+} linkage was constructed within MCM-41 by the reaction between an isolated $(OH)Ti(OSi)_3$ site and $Ce(III)NO_3$ in acetonitrile. Ti-MCM-41 and Ce-MCM-41 exhibit no absorption bands in the visible light region, while Ti/Ce-MCM-41 absorbs visible light up to 540 nm. Ce L_{III}-edge XANES investigations strongly suggest that the Ce ions exist in trivalent state within Ti/Ce-MCM-41. Considering these XANES results, the visible light absorption of Ti/Ce-MCM-41 may be considered to be due to the metal-to-metal charge-transfer (MMCT) excitation of the Ti^{4+}–O–Ce^{3+} linkage (Ti^{4+}–O–$Ce^{3+} \rightarrow Ti^{3+}$–O–$Ce^{4+}$) which plays an important role in the oxidation of 2-propanol [38].

5.1.3.2. Photocatalytic reactions on V-oxide species constructed within zeolite framework structures

Zeolites having transition metal oxides in their frameworks have been the focus of much attention for their interesting and distinctive properties. Thus far, several types of zeolites incorporating V-oxide species have been developed and the true chemical

nature and reactivity of the species, especially their photochemical properties, are beginning to be understood. Among these, the unique photocatalytic properties of the V-oxide species towards the partial oxidation of alkenes as well as other reactions have been reported [21–25,39]. In fact, the dispersion level of the V-oxide species is known to be the key factor in controlling the photocatalytic reactivity and a well-prepared V-oxide species within a zeolite framework structure has been shown to exhibit unique and high photocatalytic reactivity.

The VS-1 catalyst exhibited a photoluminescence spectrum having a vibrational fine structure at around 400–650 nm upon excitation at around 300 nm due to the highly dispersed tetrahedrally coordinated V–O moieties in C_{3v} symmetry [21–25]. Those excitation and photoluminescence spectra are attributed to the charge-transfer processes on the V–O moieties of the tetrahedral vanadate ions (VO_4^{3-}), involving an electron transfer from the O^{2-} to V^{5+} ions and a reverse radiative decay from the charge-transfer excited triplet state to its ground state:

$$(V^{5+} = O^{2-}) \underset{h\nu'}{\overset{h\nu}{\rightleftharpoons}} (V^{4+} - O^{-})^*$$

From the second derivative of the photoluminescence spectrum, the energy separation between the (0–0) and (0–1) vibrational transitions was determined to be about 960 cm^{-1} and was attributed to the vibrational transition in the V=O bond. An energy separation of 960 cm^{-1}, obtained from the photoluminescence spectrum of VS-1, was found to be slightly different from that of the V-oxide species highly dispersed on silica (1035 cm^{-1}) [21–25,40,41]. The V=O bond length of the V–O moieties within the zeolite framework structure of VS-1 obtained from the curve-fitting results of FT-EXAFS was 1.68 Å. The V=O bond length (1.68 Å) was found to be longer than that of the V–O moieties anchored on the surface of Vycor glass or silica (1.62 Å), showing that the O=V–O(Si) bond angle was smaller for the V–O moieties within the zeolite framework structure [21–25,40,41]. These results indicate that a highly dispersed V-

oxide species is present within the zeolite framework as a tetrahedrally coordinated species and that the charge-transfer excited state of this oxide species is well localized in the shorter V=O bond. The addition of propane or NO onto VS-1 led to the efficient quenching of the photoluminescence as well as a shortening of the photoluminescence lifetime, indicating that propane or NO interacts with the excited state of the V–O moieties so that the catalyst might act as a photocatalyst for reactions with NO or propane [21–25]. The reaction–time profile of the yields of N_2 in the photocatalytic decomposition of NO in the absence and the presence of propane on the VS-1 catalyst is shown in Fig. 5.1.6. UV-irradiation of the catalyst in the presence of NO led to the photocatalytic decomposition of NO while the evolution of N_2 was also observed together with O_2 and N_2O as minor products. The reaction proceeded much more efficiently under a mixture of NO and propane, thus, leading to the formation of propylene, ethylene and oxygen-containing compounds such as CH_3CHO and CO_2 in addition to the evolution of N_2. The yield as well as the selectivity for the formation of N_2 increased in proportion to the amount of added propane, while the yield of the formation of N_2O decreased and the yield of the oxygen-containing products increased [21–25]. Moreover, the turnover frequency of the catalyst for the decomposition of NO exceeded unity after prolonged UV-irradiation. These results clearly indicate that this reaction is photocatalytic and that the photocatalytic reduction of NO could proceed efficiently in the presence of propane on the VS-1 catalyst. The reduction of NO with propane on VS-1 was about five times higher than on the V-oxide photocatalyst anchored onto porous Vycor glass or silica, indicating that the difference in the coordination structure and electronically excited states of the V-oxide species are the main factors controlling the reactivity for the photocatalytic reduction of NO. The efficiency of the photocatalytic reduction of NO was found to depend strongly on the kind of hydrocarbons used, such as CH_4 and C_2H_6, and among these hydrocarbons, C_3H_8 showed the highest enhancement in the reaction rate, indicating that the

abstraction of the H atom from the hydrocarbons by a charge-transfer excited state, $(V^{4+}–O^{-})^{*}$, plays a significant role in the enhancement of the reaction [21–25]. The importance of the abstraction of an H atom from the hydrocarbons is also confirmed by the fact that the presence of CO did not enhance the photocatalytic reduction of NO. The photo-induced adsorption of NO and C_3H_8 were also investigated. Only small amounts of NO were found to be adsorbed onto the catalyst under UV-irradiation while the adsorption of NO was greatly enhanced in the co-existence of C_3H_8. These results suggest the importance of the intermediate species formed from NO and hydrocarbonradicals, followed by further reactions with NO to produce N_2 as well as oxygen-containing products such as CH_3CHO and CO_2. From these results, it can be emphasized that the differences in the coordination structures and the electronically excited states of the V-oxide species are the main factors controlling the photocatalytic activity for the direct decomposition as well as reduction of NO. The incorporation of a V-oxide species into the zeolite framework made it possible to control the local structure as well as the electronic state of the V-oxide species on a molecular scale. Thus, using zeolites as host materials for active sites in various photocatalytic reactions can be considered an especially promising way to develop unique and well-defined photocatalysts having high reactivity and selectivity.

The highly dispersed V-oxide species exhibit unique photocatalytic activity, however, UV light irradiation is essential for their activation. It has been reported that the alkali-ion modification of the highly dispersed V-oxide species results in the formation of a unique surface vanadate species which exhibits photocatalytic activity for the partial oxidation of hydrocarbons under visible light irradiation ($\lambda > 390$ nm) [42,43]. The V/SiO_2 (VS) catalyst prepared by an impregnation method exhibits a typical photoluminescence spectrum at around 500 nm with a well-defined vibrational fine structure upon excitation at 310 nm due to the highly dispersed tetrahedrally coordinated V-oxide species. However, the addition of alkali metal ions such as Na^{+},

K^+ and Rb^+ onto the VS catalyst by an impregnation method (Na_2O–VS, K_2O–VS, Rb_2O–VS) led to the appearance of unique featureless photoluminescence at around 530 nm upon excitation at 400 nm. This featureless photoluminescence can be attributed to the formation of the VO_4 tetrahedron where two V–O bonds interact with an alkali metal ion [43]. This unique V-oxide species exhibits photocatalytic activity for the partial oxidation of hydrocarbons under visible light irradiation ($\lambda > 390$ nm), e.g., Rb_2O–VS oxidizes propane into COx (CO and CO_2) and propanone photocatalytically. The conversion of propane reached 67.1%, while the selectivity for COx (CO and CO_2) and propanone were 34 % and 60 %, respectively [43].

Another type of visible light-responsive photocatalyst has recently been prepared by the isomorphous substitution of a Ti^{4+} species within ETS-10 with the V-oxide species [44]. ETS-10 is a microporous titanosilicate zeolite with a framework containing linear Ti–O–Ti–O– chains where Ti^{4+} species exist in octahedral coordination. The vanadium substituted ETS-10 (ETVS-10: V/(V + Ti) = 0.43) was prepared by hydrothermal treatment. The Raman spectrum of ETVS-10 shows a characteristic –V–O–Ti–bond vibration at 839 cm^{-1} while the NEXAFS spectrum of ETVS-10 exhibits peaks due to the L_{III}- and L_{II}-edges of V^{5+} and V^{4+}, clearly suggesting the isomorphous substitution of the Ti^{4+} species with the V^{5+} and V^{4+} species [44]. The band gap energy of ETS-10 decreased from 4.32 to 3.58 eV by the isomorphous incorporation of the V species, enabling the absorption of visible light above 400 nm. In fact, ETVS-10 exhibited photocatalytic activity for the polymerization of ethylene under visible light irradiation ($\lambda > 400$ nm) [44].

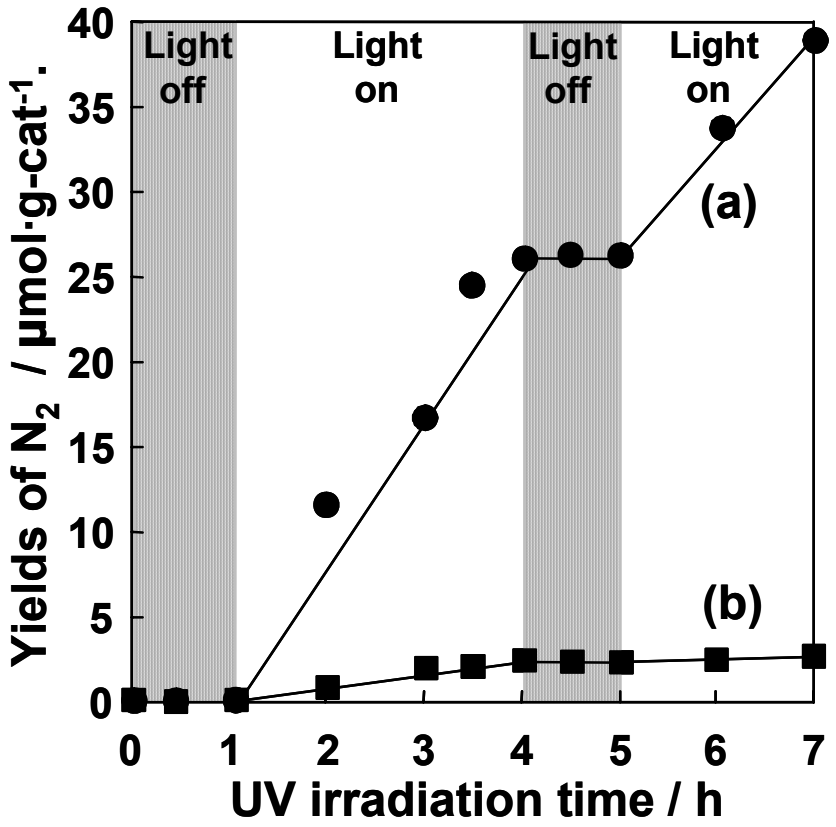

Figure 5.1.6. Reaction-time profiles of the photocatalytic decomposition of NO (a) with and (b) without propane on VS-1. Propane added: 1.97 x 10^{-4} mol/g-cat, NO: 1.82 x 10^{-4} mol/g-cat.

5.1.3.3. Photocatalytic reactions on the Mo-MCM-41 catalyst

Mo-MCM-41 (1.0 Mo wt.%) exhibited photoluminescence at around 400-600 nm upon excitation at around 295 nm (defined as X), coinciding with the photoluminescence of the tetrahedrally coordinated Mo-oxide species highly dispersed on SiO_2. Those excitation and emission spectra are attributed to the charge-transfer processes on the Mo–O moieties of the isolated tetrahedral molybdate ions (MoO_4^{2-}), involving an electron transfer from the O^{2-} to Mo^{6+} ions and a reverse radiative decay from the charge-transfer excited triplet state. The width and wavelength at the maximum intensity of the emission band did not change upon varying the excitation wavelength, indicating that there is only one luminescent moiety.

$$[Mn^{6+} = O^{2-}]_{(I)} \xrightarrow{hv} [Mo^{5+} = O^{-}]^{*} \xrightarrow{hv'} [Mo^{6+} = O^{2-}]$$

On the other hand, there were at least two luminescent species (absorption spectrum can be deconvoluted into two components in wavelength regions X and Y: 295 and 310 nm, respectively) on Mo-MCM-41 (4.0 Mo wt.%) [28]. The increase in the Mo content led to the formation of not only an emitted X site with a photoluminescence lifetime of 2.25 ms but also another emitting Y site with low photoluminescence yields and a short photoluminescence lifetime (0.91 ms). Taking the results of XAFS measurements into consideration, only isolated tetrahedrally coordinated Mo-oxides are formed at lower Mo loadings, while isolated tetrahedrally coordinated Mo-oxides as well as an oligomeric tetrahedral $(MoO_4^{2-})n$ species are formed in higher Mo loadings. The addition of C_3H_8 or NO to Mo-MCM-41 (1.0 Mo wt.%) was seen to lead to the efficient quenching of the photoluminescence as well as a shortening of the photoluminescence lifetime, as shown in Fig. 5.1.7. On the other hand, as shown in Fig. 5.1.8, for Mo-MCM-41 (4.0 Mo wt.%), NO or C_3H_8 interacted with the X site more efficiently than the Y site. It can, thus, be expected that an isolated tetrahedral Mo-oxide species will exhibit higher photocatalytic reactivity as

compared to the $(MoO_4^{2-})n$ species.

Measurements on the photocatalytic reaction of NO in the presence of C_3H_8 were performed on Mo-MCM-41. Under UV-irradiation, the photocatalytic reaction of NO with C_3H_8 was found to proceed efficiently, leading to the formation of N_2 and oxygencontaining compounds such as CH_3COCH_3 and CO_2. Fig. 5.1.9 shows the relationship between the yields of N_2, or CH_3COCH_3 formation and relative intensity of the absorption spectra observed in the region of 295 nm for Mo-MCM-41 (0.5, 1.0, 2.0 and 4.0 Mo wt.%). The intensities of the absorption spectra at 295 nm have a good relationship with the yields of N_2 or CH_3COCH_3 formation, suggesting that the charge-transfer excited triplet state of the tetrahedrally coordinated Mo-oxide species in a highly dispersed state plays a significant role in the reaction.

After UV-irradiation of Mo-MCM-41 in the presence of C_3H_8, its subsequent evacuation at 295 K did not lead to the recovery of the original photoluminescence intensity but to the appearance of the ESR signals due to Mo^{5+} ions.

This shows that the charge-transfer excited triplet state of the Mo-oxide species abstracts the H atom from C_3H_8 to form a Mo^{5+} ion and hydrocarbon radical [28]. Moreover, only small amounts of NO or C_3H_8 were photoadsorbed under UV-irradiation; however, a great enhancement of the photoadsorption occurred in the presence of a mixture of NO and C_3H_8. Based on these considerations, the following reaction mechanism can be proposed: the intermediate species formed between NO and the hydrocarbon radicals, which is formed by H abstraction of the photo-excited Mo-oxide species from C_3H_7, subsequently reacts with NO to produce N_2 as well as oxygen-containing compounds.

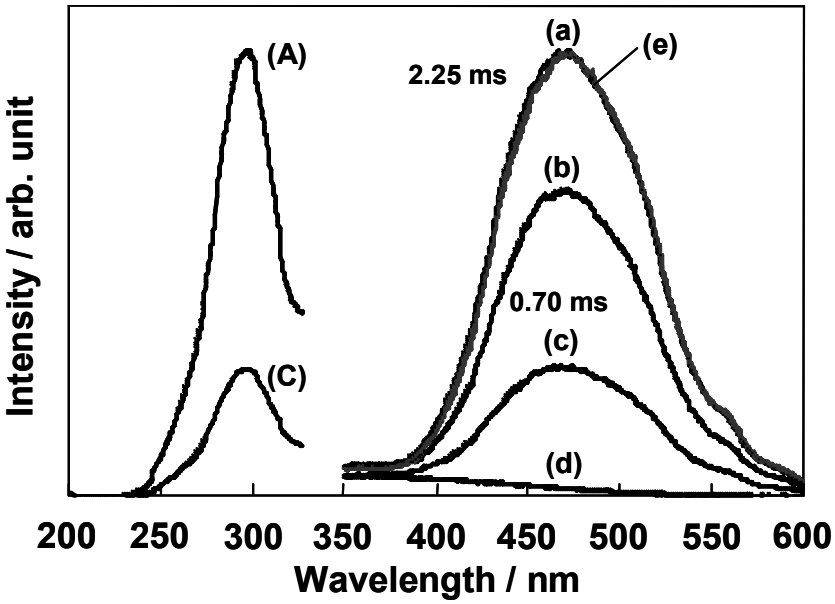

Figure 5.1.7. Effect of the addition of NO on the photoluminescence spectrum and excitation spectrum of Mo-MCM-41(1.0 Mo wt.%).

Pressure of added NO: (A, a) 0, (b) 0.07, (C, c) 0.4 Torr, (d) excess, (e) degassed after (d).

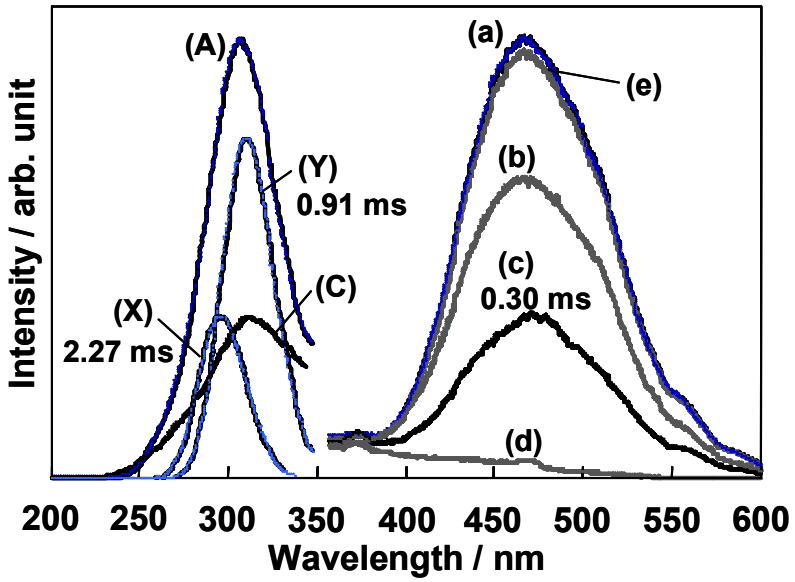

Figure 5.1.8. Effect of the addition of NO on the photoluminescence spectrum and excitation spectrum of Mo-MCM-41(4.0 Mo wt.%).

Pressure of added NO: (A, a) 0, (b) 0.6, (C, c) 4 Torr, (d) excess, (e) degassed after (d). Spectrum (A) can be deconvoluted into (X) and (Y).

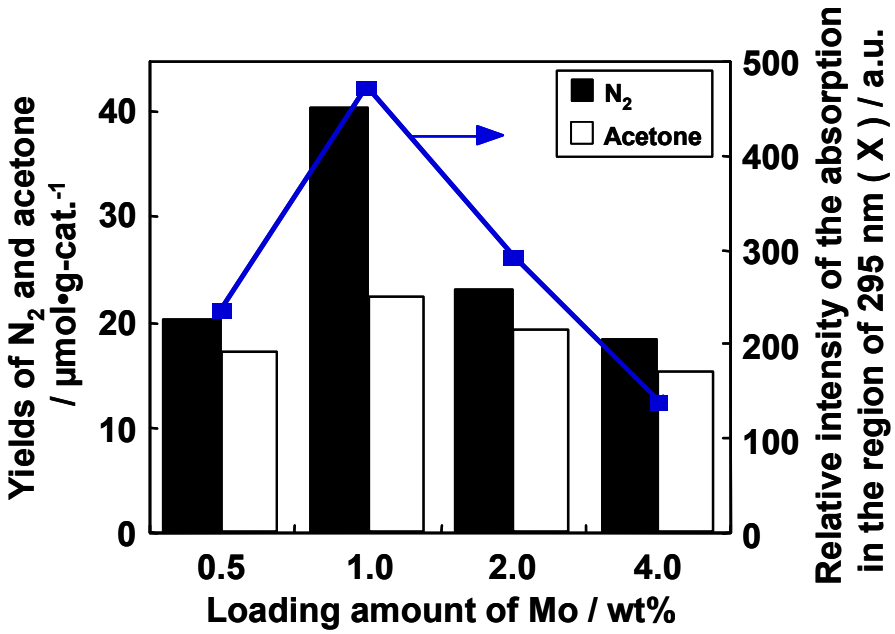

Figure 5.1.9. Relationship among the yields of N_2, acetone formation and the relative intensity of the absorption in the region of 295 nm (X) calculated by the deconvolution of the original excitation spectrum of the Mo-MCM-41 (0.5, 1.0, 2.0, and 4.0 Mo wt.%). Added propane or NO: 180 μmol•g-cat.$^{-1}$.

The photocatalytic decomposition reactions of NO were also found to be dramatically enhanced in the presence of CO, leading to the formation of N_2 and CO_2. Figure 5.1.10 shows the relationship between the yields of N_2 formation for the decomposition of NO on Mo-MCM-41 (0.5–4.0 Mo wt.%) in the presence of CO and the relative intensity of the absorption spectra observed in the total region (X and Y) of the catalyst. The yields of N_2 have a good relationship with the intensities of the absorption spectra in the total region of X and Y as well as with the amount of Mo^{4+} ions generated through the photoreduction of Mo^{6+} with CO (number of Mo^{4+} ions estimated by the number of photo-formed CO_2 molecules) [28,45]. These results indicate that the charge-transfer excited triplet states of both the isolated tetrahedral Mo-oxides and $(MoO_4^{2-})_n$ play a significant role in the reaction.

UV-irradiation of Mo-MCM-41 in the presence of CO alone and its subsequent evacuation at 293 K led to an efficient quenching of the photoluminescence. However, under identical conditions, no ESR signals due to the Mo^{5+} ions were detected, suggesting that the charge-transfer excited triplet state, i.e., the $[Mo^{5+}–O^{-}]^{*}$ complex reacts with CO to form Mo^{4+} ions and CO_2. It was found that the Mo^{4+} ions formed reacts efficiently with NO and N_2O under dark conditions to produce N_2O and N_2, respectively, as well as for the reoxidation of Mo^{4+} to Mo^{6+} ions, indicated by the reappearance of the photoluminescence of Mo^{6+} ions after the addition of NO and N_2O. From these results, it could be concluded that the following catalytic cycle plays a major role in the photocatalytic decomposition of NO in the presence of CO, i.e., Mo^{4+} ions that are formed through the reaction of the charge-transfer excited triplet state of $Mo^{6+}=O^{2-}$ with CO are reoxidized back to the original Mo^{6+} species in the presence of NO or N_2O.

Regarding the photo-oxidation of CO by O_2, an important reaction in fuel cell technology which is essential in removing CO impurities from H_2 or the electrode is poisoned by CO and performance is weakened, a plausible mechanism has been

proposed (Fig. 5.1.11) based on the known structures of the single-site $Mo^{6+}O_4$ centre as determined by XAFS [29,30]. A charge-transfer excited triplet state is observed and good quantum yields were obtained. This single-site photocatalytic method of purifying H_2 from its unwanted CO impurity is an alternative to the thermally activated heterogeneous catalytic method of achieving the same results using Pt–Fe and other noble-metal catalysts supported on alumina [46].

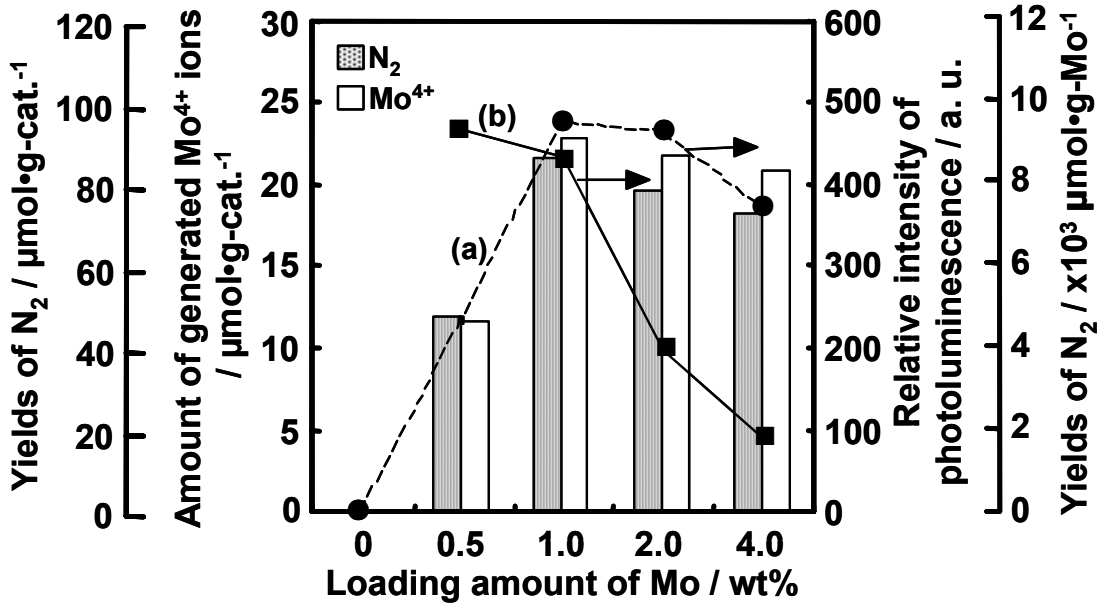

Figure 5.1.10. Relationship between the yields of N_2 formation for the photocatalytic decomposition reactions of NO by the coexistence of CO (left), amount of generated Mo^{4+} ions, the relative intensity of the absorption in the total region of (X and Y) (dotted line; a) and the yields of N_2 per Mo atoms of 1g (solid line; b) of Mo-MCM-41 (0.5, 1.0, 2.0, and 4.0 Mo wt.%). Added NO or CO: 180 μmol•g-cat.$^{-1}$.

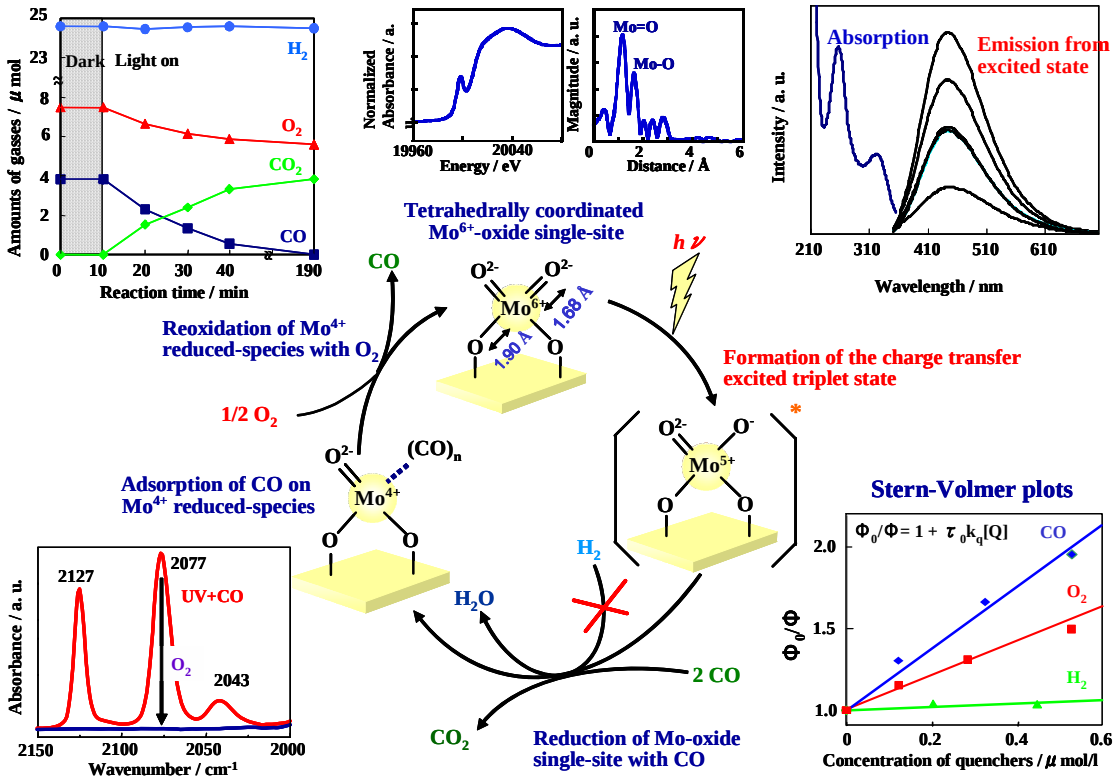

Figure 5.1.11. Photocatalytic selective elimination of CO with O_2 in the presence of H_2 on Mo-oxide single-site catalysts.

5.1.3.4. Photocatalytic reactions on Cr-HMS and Cr-MCM-41 catalysts

We have found that the Cr-containing mesoporous zeolite (Cr-HMS) shows photocatalytic reactivity for the photocatalytic decomposition of NO into N_2 and O_2 and the partial oxidation of C_3H_8 with O_2 under both UV and visible light (or sunlight) irradiation. Here, special attention is focused on an understanding of the local structure of the Cr-oxide species on Cr-HMS and their photocatalytic activity for NO decomposition [31].

The UV–vis spectra of the Cr-HMS catalysts exhibited three distinct absorption bands at around 250, 360 and 480 nm which could be assigned to the charge-transfer from O^{2-} to Cr^{6+} of the tetrahedrally coordinated Cr-oxide species, as shown in Fig. 5.1.12 [31,47]. Absorption bands above 550 nm assigned to the dichromate or Cr_2O_3 cluster could not be observed, indicating that the tetrahedrally coordinated Cr-oxide species exists in an isolated state. Cr-HMS exhibited photoluminescence spectra at ca. 550–750 nm upon excitation of the absorption (excitation) bands at ca. 250, 360 and 480 nm. These absorption and photoluminescence spectra are similar to those obtained with well-defined, highly dispersed Cr-oxides anchored onto Vycor glass or silica [15,16,31,47] and can be attributed to charge-transfer processes on tetrahedrally coordinated Cr-oxide species involving an electron transfer from O^{2-} to Cr^{6+} and a reverse radiative decay, respectively.

UV-light irradiation ($\lambda > 270$ nm) of Cr-HMS in the presence of NO in the gas phase at 275 K led to the photocatalytic decomposition of NO and evolution of N_2, N_2O and O_2. Cr-HMS also showed photocatalytic reactivity even under visible light irradiation ($\lambda > 450$ nm). The N_2 yields increased linearly with the irradiation time and the reaction stopped immediately when irradiation was ceased, as shown in Fig. 5.1.13. After prolonged irradiation, the amount of decomposed NO to form N_2 per total number of Cr ions included within the catalyst exceeded unity. These results clearly indicate that the presence of both the Cr-oxide species as well as light irradiation are

indispensable for the photocatalytic reaction to proceed and that the direct decomposition of NO occurs photocatalytically. Although the reaction rate under visible light was less than that under UV-light irradiation, the selectivity for N_2 formation (97%) under visible light was higher than that with UV-irradiation (45%). These results indicate that Cr-HMS can absorb and act as an efficient photocatalyst not only under UV but also visible light irradiation, significantly, to form N_2. The addition of NO to the Cr-HMS catalyst led to an efficient quenching of the photoluminescence spectrum, indicating that the charge-transfer excited state of the tetrahedrally coordinated isolated Cr-oxide species, $(Cr^{5+}–O^{-})$*, can easily interact with NO and also that the photo-excited species plays a major role in the photocatalytic reaction under UV and visible light irradiation.

Proton exchange membrane (PEM) fuel cells, also designated polymer electrolyte fuel cells (PEFC), demand a supply of H_2 stringently free of CO impurities and a favored method of achieving this is to catalytically oxidize the CO over either a transition-metal oxide or a supported Pt-rich catalyst, known generally as the preferential oxidation of CO in the presence of H_2 (PROX) [48–50]. But in view of both of the continuing high cost and ultimate scarcity of Pt, the design of a PROX catalyst for static fuel cell installations that is not only cheap and can be easily prepared but also function at ambient temperatures is highly desired. Here, we report on Cr^{6+} ions which function as a photocatalytic system under visible (or solar light) irradiation, thereby affording a clean, convenient (non-precious metal) catalyst for the PROX system. The XANES spectrum of Cr^{6+}-MCM-41 showed an intense and characteristic pre-edge peak, indicating that Cr^{6+}-MCM-41 contains a Cr^{6+}-oxide species in tetrahedral coordination, as can be seen in Fig. 5.1.14 [32]. Curve-fitting analysis of the Cr–O peaks revealed that the Cr^{6+}-oxide species exists in a highly distorted tetrahedral coordination with two shorter Cr=O double bonds (bond length (R) = 1.59 Å, coordination number of CN = 2.0) and two longer Cr–O single bonds (R = 1.85 Å, CN

= 2.1). UV–vis spectrum of Cr^{6+}-MCM-41 exhibits three distinct absorption bands at around 240, 350 and 460 nm due to the ligand to metal charge-transfer transition (LMCT: from O^{2-} to Cr^{6+}) of the tetrahedrally coordinated Cr^{6+}-oxide species [31,32,51]. Cr^{6+}-MCM-41 exhibited a photoluminescence spectrum at around 550–800 nm upon excitation at around 240, 350 and 460 nm at 298 K, due to the tetrahedrally coordinated Cr^{6+}-oxide species. The absorption and emission spectra are attributed to the following charge-transfer processes on the Cr=O moieties of the tetrahedral monochromate species (CrO_4^{2-}) involving an electron transfer from O^{2-} to Cr^{6+} ions and a reverse radiative decay from the charge-transfer excited triplet state [31,47,52]:

$$[Cr^{6+} = O^{2-}] \xrightarrow{h\nu} [Cr^{5+} = O^{-}]^* \xrightarrow{h\nu'} [Cr^{6+} = O^{2-}]$$

The photoluminescence of Cr^{6+}-MCM-41 is quenched in its intensity by the addition of CO, O_2 and H_2, indicating that the Cr^{6+}-oxide species, in its charge-transfer excited triplet state, easily interacts with CO, O_2 and H_2. Moreover, the absolute quenching rate constants (k_q (l/mol s)) for each gas which were determined by the Stern–Volmer plots [32,53], were found to increase in the following order: H_2 ($8.63 - 105$) << CO ($5.91 - 10^9$) < O_2 ($1.12 - 10^{10}$). These results indicated that CO interacts very efficiently with the photo-excited Cr^{6+}-oxide species as compared to H_2. Fieldwork experiments were carried out to investigate the photocatalytic reactivity of Cr^{6+}-MCM-41 for the preferential oxidation of CO with O_2 in the presence of H_2 under natural conditions of clean and safe solar light irradiation. The reaction–time profiles of the photocatalytic oxidation of CO with O_2 in the presence of H_2 on Cr^{6+}-MCM-41 under solar light are shown in Fig. 5.1.14. These data were observed from 11:00 to 14:30 of a sunny day with average solar light intensity of 78.5 mW/cm^2 and irradiation area of 3 cm^2, clearly showing that Cr^{6+}-MCM-41 could operate efficiently as a photocatalyst for CO oxidation. After light irradiation for 3.5 h, CO conversion and selectivity reached ~100% and 96%, respectively. The present results demonstrated

that Cr^{6+}-MCM-41 can be applied for clean and cost-efficient photo-PROX reaction systems using solar light energy at ambient temperatures without the use of Pt or other precious noble metals.

As shown in Fig. 5.1.14, visible light irradiation of Cr^{6+}-MCM-41 in the presence of CO led to the appearance of a typical FT-IR band due to the monocarbonyl Cr^{4+} species [Cr^{4+}(CO)] at 2201 cm^{-1} [32], accompanied by the formation of CO_2. Moreover, the addition of O_2 on this system at 298 K led to the complete disappearance of FT-IR band, indicating the regeneration of the original Cr^{6+}-oxide species. The catalytic reaction cycles on Cr^{6+}-MCM-41 under visible light ($\lambda > 420$ nm) or solar light irradiation can be proposed as in Fig. 5.1.14. That is, initially, the tetrahedral Cr^{6+}-oxide species is photo-excited to its charge-transfer excited triplet state and reacts with CO to form CO_2 and a photo-reduced Cr^{4+}-oxide species. Then the Cr^{4+}-oxide species are efficiently oxidized by O_2 and the original Cr^{6+}-oxide species are generated. The high CO selectivity observed for the Cr^{6+}-MCM-41 can be attributed to the high and selective reactivity of the photo-excited Cr^{6+}-oxide species with CO, as indicated by the high quenching efficiency of CO as compared to H_2.

These results show that the design of transition metal ion-containing zeolite catalysts is one of the most promising ways to develop unique light driven photocatalytic systems that enable the efficient utilization of abundant visible or solar light energy.

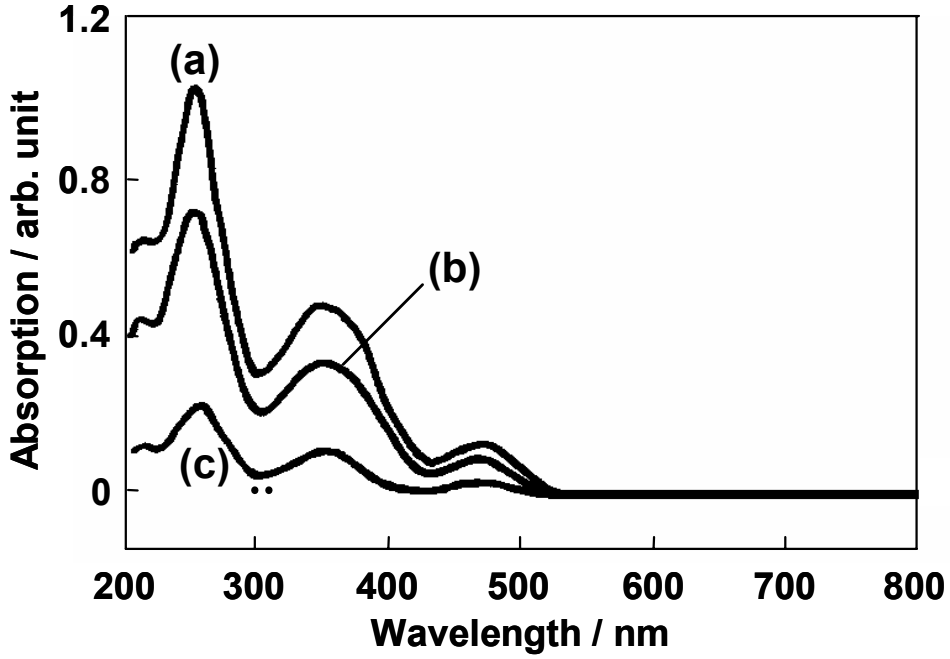

Figure 5.1.12. UV-VIS spectra of Cr-HMS catalysts (a) 2.0 wt.%, (b) 1.0wt.%, (c) 0.2 wt.%, as Cr.

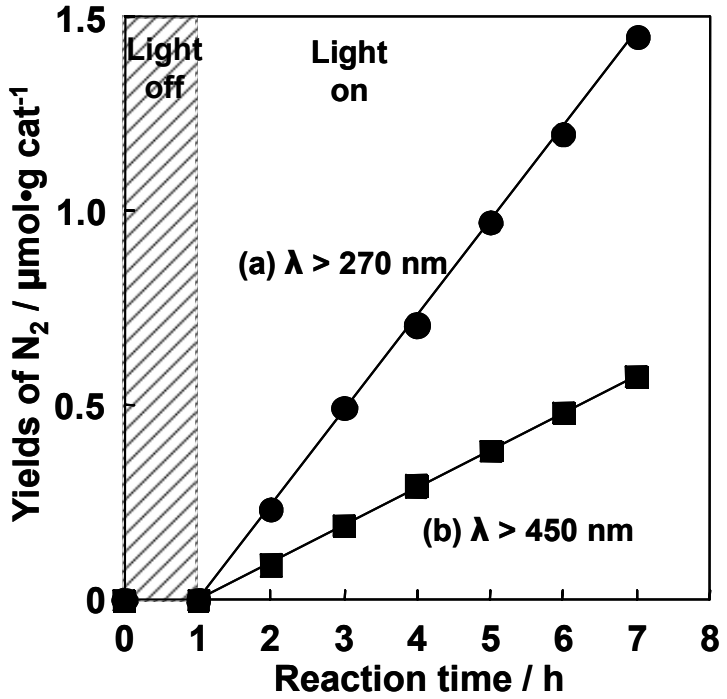

Figure 5.1.13. R eaction-time profile of N_2 formation in the photocatalytic decomposition of NO on the Cr-HMS catalyst at 273 K (2.0 wt.% as Cr) under UV-light irradiation (a: $\lambda > 270$ nm) and visible light irradiation (b : $\lambda > 450$ nm).

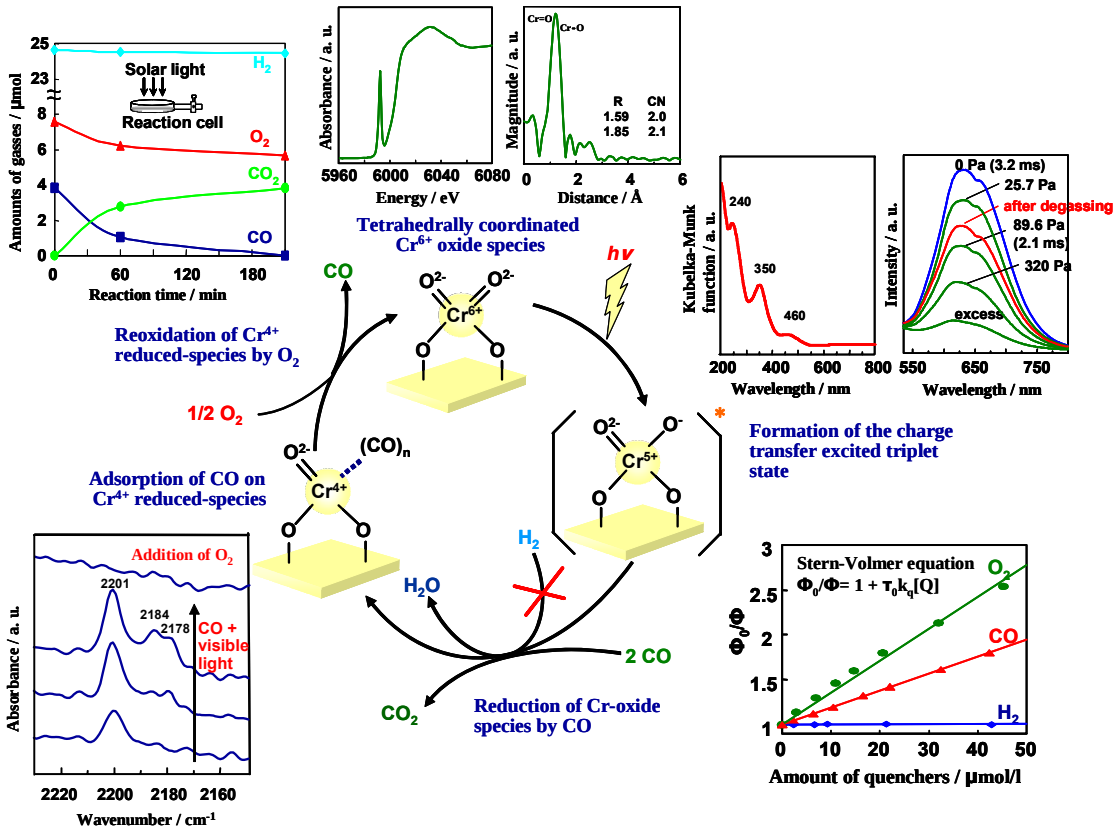

Figure 5.1.14. Photocatalytic selective elimination of CO with O_2 in the presence of H_2 on a Cr-MCM-41 single-site catalyst.

5.1.4. Conclusions

In this Chapter, the photocatalytic reactivities of various transition metal oxides (Ti, V, Mo and Cr) incorporated within zeolite framework structures as single site heterogeneous catalysts have been summarized. The interactions of these active species with gaseous NOx (NO and N_2O) and CO_2 were monitored and the photocatalytic reactivities of the catalysts for the decomposition of NOx as well as reduction of CO_2 with H_2O have been presented.

Metal oxide catalysts (Ti, V, Mo and Cr) constructed within the framework or cavities of various zeolites by ion-exchange or hydrothermal synthesis were found to exist in highly dispersed tetrahedral coordination states and were observed to act as efficient photocatalysts for the decomposition of NO into N_2 and O_2 as well as the reduction of CO_2 with H_2O to produce CH_4 and CH_3OH. Photoluminescence investigations revealed that the efficient interaction of the charge-transfer photo-excited complexes of these oxides, $(Me^{(n-1)+}–O^{-})^{*}$, i.e., the electron–hole pair state with reactant molecules such as NO, CO_2 and H_2O, plays a significant role in the photocatalytic reactions.

These results confirmed that by utilizing the physicochemical properties of various zeolites such as the pore size diameter or the channel structure, it becomes possible to control the photocatalytic activity as well as selectivity of the reaction, as was demonstrated by the results of the photocatalytic reduction of CO_2 with H_2O on Ti-containing mesoporous zeolites. It can, thus, be seen that the use of zeolites is one of the most promising approaches in the design of local structures at the molecular level for the development of effective photocatalytic systems to reduce and eliminate global air and water pollution.

5.1.5. References

[1] M. Anpo, in: P. Tundo, P. Anastas (Eds.), *Green Chemistry*, Oxford University Press, 1, (2000).

[2] M. Anpo, in: A. Corma, F.V. Melo, S. Mendioroz, J.L.G. Fierro (Eds.), *Studies in Surface Science and Catalysis*, vol. 130A, Proceedings of the 12th International Congress Catalysts, Granada, 157, (2000).

[3] D.F. Ollis, H. AlEkabi (Eds.), *Photocatalytic Purification and Treatment of Water and Air*, Elsevier, (1993).

[4] E. Pelizzetti, M. Schiavello (Eds.), *Photochemical Conversion and Storage of Solar Energy*, Kluwer Academic Publishers, (1991).

[5] M. Kitano, M. Matsuoka, M. Ueshima, M. Anpo, *Appl. Catal. A: Gen.*, **325**, 1 (2007).

[6] M. Kitano, M. Takeuchi, M. Matsuoka, J.M. Thomas, M. Anpo, *Catal. Today*, 120, 133 (2007).

[7] M. Matsuoka, M. Anpo, *Curr. Opin. Solid State Mater. Sci.*, **7**, 451 (2003).

[8] M. Anpo, M. Che, *Adv. Catal.*, **44**, 119 (2000).

[9] M. Anpo, M. Takeuchi, K. Ikeue, S. Dohshi, *Curr. Opin. Solid State Mater. Sci.*, **6**, 381 (2002).

[10] M. Anpo, M. Takeuchi, *Catal. J.*, **216**, 505 (2003).

[11] H. Yamashita, M. Anpo, *Curr. Opin. Solid State Mater. Sci.*, **7**, 471 (2003).

[12] M. Anpo, Bull. *Chem. Soc. Jpn.*, **77**, 1427 (2004).

[13] M. Anpo, S. Dohshi, M. Kitano, Y. Hu, M. Takeuchi, M. Matsuoka, *Ann. Rev. Mater. Res.*, **35**, 1 (2005).

[14] M. Anpo (Ed.), Surface Photochemistry, Wiley, (1996) (and references therein).

[15] M. Anpo (Ed.), Photofunctional Zeolites, NOVA Publishers Inc., (2000) (and references therein).

[16] M. Matsuoka, M. Anpo, *J. Photochem. Photobiol. C: Photochem. Rev.*, **3**, 225

(2003).

[17] M. Anpo, H. Yamashita, Y. Ichihashi, Y. Fujii, M. Honda, *J. Phys. Chem.*, **101**, 2632 (1997).

[18] H. Yamashita, K. Ikeue, T. Takewaki, M. Anpo, *Top. Catal.*, **18**, 95 (2002).

[19] K. Ikeue, H. Yamashita, M. Anpo, *Electrochemistry*, **70**, 402 (2002).

[20] H. Yamashita, Y. Ichihashi, M. Anpo, M. Hashimoto, C. Louis, M. Che, *J. Phys. Chem.*, **100**, 16041 (1996).

[21] S. Higashimoto, M. Matsuoka, H. Yamashita, M. Anpo, *Jpn. J. Appl. Phys.*, **38**, 47 (1999).

[22] S. Higashimoto, M. Matsuoka, H. Yamashita, M. Anpo, O. Kitao, H. Hidaka, M. Che, E. Giamello, *J. Phys. Chem. B*, **104**, 10288 (2000).

[23] M. Anpo, S. Higashimoto, M. Matsuoka, N. Zhanpeisov, Y. Shioya, S. Dzwigaj, M. Che, *Catal. Today*, **78**, 211 (2003).

[24] Y. Hu, S. Higashimoto, S. Takahashi, Y. Nagai, M. Anpo, *Catal. Lett.*, **100**, 35 (2005).

[25] Y. Hu, N. Wada, K. Tsujimaru, M. Anpo, *Catal. Today*, **120**, 139 (2007).

[26] R. Tsumura, S. Higashimoto, M. Matsuoka, H. Yamashita, M. Che, M. Anpo, *Catal. Lett.*, **68**, 101 (2000).

[27] M. Matsuoka, T. Kamegawa, R. Takeuchi, M. Anpo, *Catal. Today*, **122**, 39 (2007).

[28] S. Higashimoto, Y. Hu, R. Tsumura, K. Iino, M. Matsuoka, H. Yamashita, Y.G. Shul, M. Che, M. Anpo, *J. Catal.*, **235**, 272 (2005).

[29] T. Kamegawa, R. Takeuchi, M. Matsuoka, M. Anpo, *Catal. Today*, **111**, 248 (2006).

[30] M. Anpo, J.M. Thomas, *Chem. Commun.*, 3273 (2006).

[31] H. Yamashita, K. Yoshizawa, M. Ariyuki, S. Higashimoto, M. Che, M. Anpo, *Chem. Commun.*, 435 (2001).

[32] T. Kamegawa, J. Morishima, M. Matsuoka, J.M. Thomas, M. Anpo, *J. Phys. Chem.*

C, **111**, 1076 (2007).

[33] H. Yamashita, S. Kawasaki, Y. Ichihashi, M. Harada, M. Takeuchi, M. Anpo, G. Stewart, M.A. Fox, C. Louis, M. Che, *J. Phys. Chem. B*, **102**, 5870 (1998).

[34] H. Yamashita, M. Honda, M. Harada, Y. Ichihashi, M. Anpo, T. Hirao, N. Itoh, N. Iwamoto, *J. Phys. Chem. B*, **102**, 10707 (1998).

[35] H. Yamashita, Y. Ichihashi, M. Harada, G. Stewart, M.A. Fox, M. Anpo, *J. Catal.*, **158**, 97 (1996).

[36] H. Yamashita, N. Kamada, H. He, K. Tanaka, S. Ehara, M. Anpo, *Chem. Lett.*, 855 (1994).

[37] M. Anpo, K. Chiba, *J. Mol. Catal.*, **74**, 207 (1992).

[38] R. Nakamura, A. Okamoto, H. Osawa, H. Irie, K. Hashimoto, *J. Am. Chem. Soc.*, **129**, 9596 (2007).

[39] T. Tanaka, H. Yamashita, R. Tsuchitani, T. Funabiki, S. Yoshida, *J. Chem. Soc.*, Faraday Trans. **1**, 2987 (1988).

[40] M. Matsuoka, T. Kamegawa, M. Anpo, in: G. Ertl, H. Kno¨ zinger, F. Schu¨ th, J. Weitkamp (Eds.), Handbook of Heterogeneous Catalysis, Wiley–VCH, 1065 (2008).

[41] M. Anpo, M. Matsuoka, in: K.D.M. Harris, P. Edwards (Eds.), Turning Points in Solid-State, Materials and Surface Science, RSC Publishing, 496 (2008).

[42] F. Amano, T. Ito, S. Takenaka, T. Tanaka, *J. Phys. Chem. B*, **109**, 10973 (2005).

[43] T. Tanaka, S. Takenaka, T. Funabiki, S. Yoshida, *Chem. Lett.*, 1585 (1994).

[44] M.J. Nash, S. Rykov, R.F. Lobo, D.J. Doren, I. Wachs, *J. Phys. Chem. C*, **111**, 7029 (2007).

[45] A.A. Lisachenko, K.S. Chikhachev, M.N. Zakharov, L.L. Basov, B.N. Shelimov, I.R. Subbotina, M. Che, S. Coluccia, *Top. Catal.*, **20**, 119 (2002).

[46] A. Siani, D.K. Captain, O.S. Alexeev, E. Stafyla, A.B. Hungria, P.A. Midgley, J.M. Thomas, R.D. Adams, M.D. Amiridis, *Langmuir*, **22**, 5160 (2006).

[47] M.F. Hazenkamp, G. Blasse, *J. Phys. Chem.*, **96**, 3442 (1992).

[48] S.Y. Chin, O.S. Alexeev, M.D. Amiridis, *Appl. Catal A: Gen.*, **286**, 157 (2005).

[49] A. Manasilp, E. Gulari, *Appl. Catal. B*, **37**, 17 (2004).

[50] T.V. Choudhary, D.W. Goodman, *Catal. Today*, **77**, 65 (2002).

[51] E. Groppo, C. Lamberti, S. Bordiga, G. Spoto, A. Zecchina, *Chem. Rev.*, **105**, 115 (2005).

[52] C. Murata, H. Yoshida, T. Hattori, *Chem. Commun.*, 2412 (2001).

[53] N.J. Turro (Ed.), Modern Molecular Photochemistry, Benjamin/Cummings, New York, (1978).

5.2. Preparation and Characterization of Unique Inorganic-Organic Hybrid Mesoporous Materials Incorporating Arene Metal Carbonyl Complexes

5.2.1. Introduction

Recently, inorganic–organic hybrid mesoporous materials (HMM) incorporating organic moieties such as $–CH_2–$ [1,2], –CH=CH– [2,3], $–C_6H_4–$ [4], $–(C_6H_4)_2–$ [5] within their silica frameworks have been developed and attracted much attentions for their applications in the field of catalysis, separation chemistry and many other fields. For now, various attempts have been made to functionalize the organic moieties within HMM. For example, HMM functionalized by sulfuric acid group have been synthesized [6,7] and applied as the solid acid catalysts for the esterification reaction [7]. Another example of the functionalization of HMM is their organometallic modification, enabling the direct incorporation of organometallic complexes such as arene metal carbonyls within the framework structures of HMM [8]. More recently, in addition to HMM, modification of microporous metal-organic frameworks (MOF) with arene metal carbonyl complexes has been reported [9]. The present work deals with the organometallic modifications of phenylene (ph = $–C_6H_4–$) or biphenylene (biph = $–(C_6H_4)_2–$) bridged hybrid mesoporous materials (HMM-ph or HMM-biph). Successful incorporation of arenetricarbonyl complexes such as [$–phM(CO)_3–$] (M = Cr, Mo, W) and [$–biphCr(CO)_3–$] within the organosilica framework of HMM-ph or HMM-biph by a simple chemical vapor deposition (CVD) method as well as their stability under thermovacuum treatment were investigated by various in situ spectroscopic methods.

5.2.2. Experimental

Phenylene- (ph = $–C_6H_4–$) and biphenylene-(biph = $–(C_6H_4)_2–$) bridged HMM (HMM-ph and HMM-biph) were synthesized by the method reported by Inagaki et al. using 1,4-bis(triethoxysilyl)benzene [4] and 4,4´-bis(triethoxysilyl)biphenyl [5],

respectively, in the presence of octadecyl-trimethylammonium chloride. Inorganic siliceous MCM-41 was synthesized using fumed silica in the presence of cetyltrimethylammonium bromide as precursors [10]. The HMM-ph and HMM-biph which incorporate arenetricarbonyl complexes such as [–phM$(CO)_3$–] (M = Cr, Mo, W) and [–biphCr$(CO)_3$–] were prepared by CVD treatments of HMM-ph or HMM-biph with $Cr(CO)_6$ at 398 K for 40 min, $Mo(CO)_6$ at 368 K or $W(CO)_6$ at 378 K for 120 min in vacuum. Hereafter, these samples are denoted as HMM-phM$(CO)_3$ or HMM-biphCr$(CO)_3$. MCM-41 deposited with $Cr(CO)_6$ or $C_6H_6Cr(CO)_3$ (denoted as $Cr(CO)_6$/MCM-41 and $C_6H_6Cr(CO)_3$/MCM-41) were prepared at 398 K and 343 K, respectively, by physical vapor deposition (PVD) method for 40 min in vacuum. The procedure of PVD method is essentially same as that of CVD method, while no chemical reaction proceeds between metal carbonyl complexes and substrate in the case of PVD treatment. Prior to the introduction of metal carbonyl compounds, HMM-Ph, HMM-biph and MCM-41 were degassed at 473 K for 2 h. After CVD or PVD treatments, samples were transferred to the cells for FT-IR or UV-vis measurements under nitrogen and the spectra were measured in vacuum at 298 K. The FT-IR spectra were recorded at room temperature with an FT-IR spectrometer (JASCO FT-IR 660 Plus) with self-supporting pellets of the samples in transmission mode at 4 cm^{-1} resolution. The diffuse reflectance UV-vis spectra were recorded at 298 K with a Shimadzu UV-2200A double-beam digital spectrophotometer. The powdered X-ray diffraction (XRD) patterns of the samples were obtained with Shimadzu XRD-6100 using Cu Kα radiation (λ = 1.5417 Å). CO-TPD (Temperature Programmed Desorption) experiments were carried out in a temperature range from 323 to 723 K with a heating rate of 5 K/min. The effluents were then analyzed using a quadrupole mass spectrometer (MQA100TS, Anelva).

5.2.3. Results and Discussion

Figure 5.2.1(a) shows the XRD pattern of HMM-ph. The XRD pattern of HMM-ph exhibits sharp peaks in the region of $2\theta < 10^{o}$ due to a two-dimensional hexagonal structure. Moreover, HMM-ph exhibits additional small sharp peaks in the region of $10^{o} < 2\theta < 50^{o}$, showing that the periodicity of the $O_{1.5}Si\text{-}C_6H_4\text{-}SiO_{1.5}$ units [4] exists within the wall of the mesoporous framework. HMM-ph was, thus, found to have a hexagonal structure with a lattice constant of 51.5 Å and crystal-like pore walls. Figure 5.2.2 shows the FT-IR spectra of HMM-ph observed after CVD treatment with $Cr(CO)_6$ at various temperatures. The HMM-ph treated with $Cr(CO)_6$ at 353 K shows two FT-IR peaks at 1991 and 2020 cm^{-1}. These peaks correspond well to the T_{1u} (1991 cm^{-1}) and E_g (2020 cm^{-1}) vibrational mode, respectively, of the physically adsorbed $Cr(CO)_6$ species on MCM-41 (Fig. 5.2.3(a)) [8] or SiO_2 [11], showing that $Cr(CO)_6$ species are physically adsorbed on HMM-ph after CVD treatment at 353 K. However, the CVD treatment at 398 K led to the drastic change in the FT-IR spectrum and the appearance of one sharp peak at 1981 cm^{-1} and a broad peak at 1940–1840 cm^{-1}, showing good agreement with the a_1 (1981 cm^{-1}) and e (1911, 1884 cm^{-1}) vibrational mode, respectively, of the $C_6H_6Cr(CO)_3$ complex physically deposited on MCM-41 (Fig. 5.2.3(b)) [8] or SiO_2 [11]. These results indicated that phenylene moieties within the HMM-ph frameworks react with $Cr(CO)_6$ during CVD treatment at 398 K to form $phCr(CO)_3$ complex (Eq.(1)).

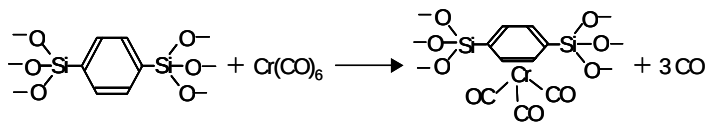

(1)

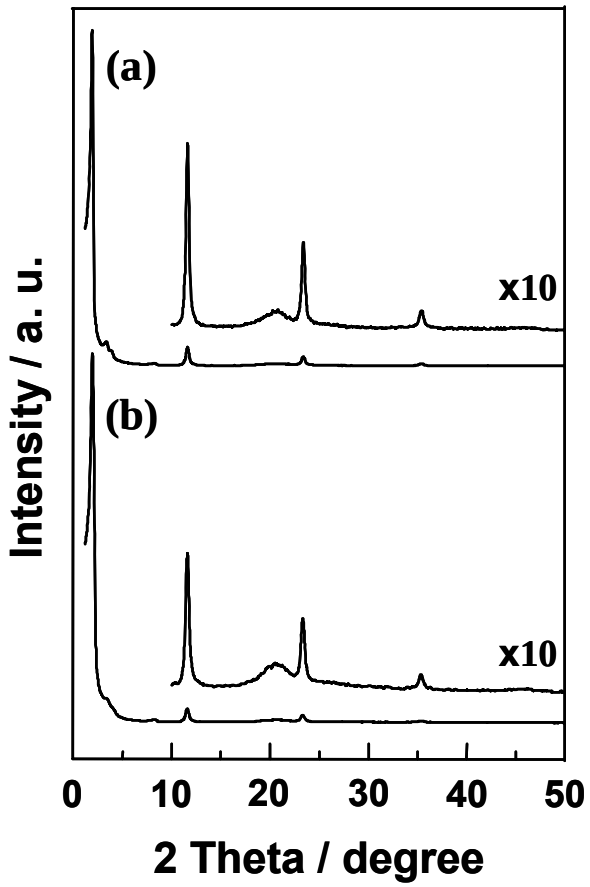

Figure 5.2.1. XRD patterns of (a) HMM-ph and (b) HMM-ph$Cr(CO)_3$.

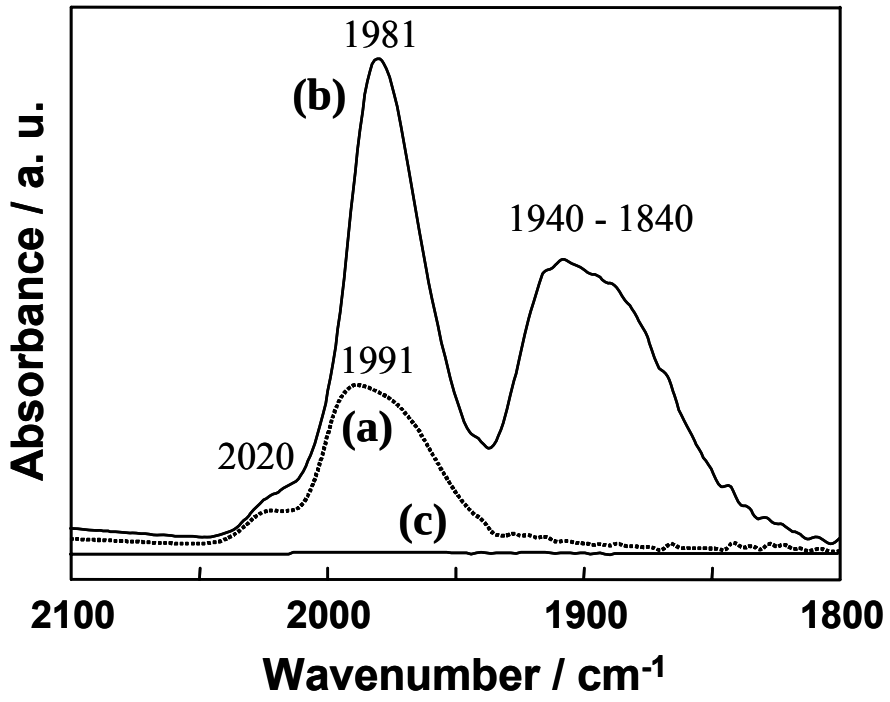

Figure 5.2.2. FT-IR spectra of (a) HMM-ph deposited with $Cr(CO)_6$ at 353 K, (b) HMM-ph$Cr(CO)_3$ and (c) HMM-ph. To obtain real spectra of Cr-compounds, the FT-IR spectrum of HMM-ph was subtracted from all observed spectra as background.

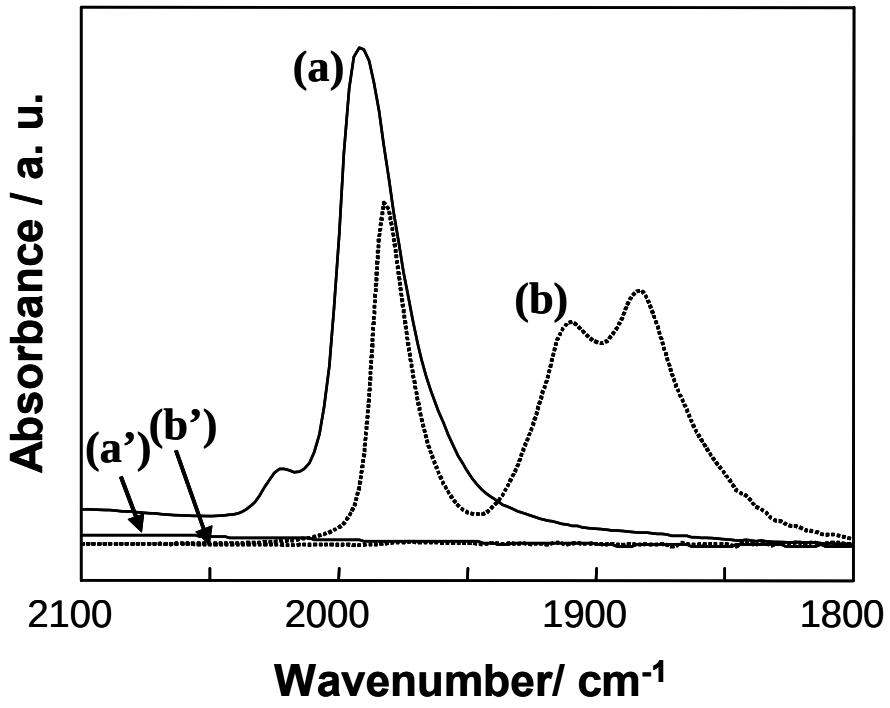

Figure 5.2.3. FT-IR spectra of (a, a′) $Cr(CO)_6$/MCM-41 and (b, b′) $C_6H_6Cr(CO)_3$/MCM-41 measured (a, b) before and (a′, b′) after evacuation at 373 K.

To obtain real spectra of Cr-compounds, the FT-IR spectrum of HMM-ph was subtracted from all observed spectra as background.

Figure 5.2.1(b) shows the XRD pattern of HMM-ph$Cr(CO)_3$. The XRD patterns were almost the same before and after CVD treatment so that the structure of HMM-ph and the covalently bonded network of the $O_{1.5}Si$-C_6H_4-$SiO_{1.5}$ units could be retained even after CVD treatment at 398 K. The BET surface area of HMM-ph and HMM-ph$Cr(CO)_3$ were determined to be 806 m^2/g and 771 m^2/g, respectively, supporting the fact that the framework of HMM-ph is maintained after the CVD treatment. Figure 5.2.4 shows the UV-vis spectra of HMM-ph and HMM-ph$Cr(CO)_3$. The intense band at around 276 nm observed for HMM-ph can be assigned to the π–π^* transition of framework phenylene moieties [12]. HMM-ph exhibits no absorption band in the wavelength region above 300 nm, while HMM-ph$Cr(CO)_3$ shows a absorption peak at around 320 nm and a long-tailed absorption beyond 400 nm. These peaks show good agreement with the UV-vis absorption bands of $C_6H_6Cr(CO)_3$, i.e., a charge transfer band from Cr to benzene ring at 315 nm and ligand field absorption of Cr above 400 nm, respectively [13], firmly supporting the formation of ph$Cr(CO)_3$ complex within the frameworks of HMM-ph [8]. Figure 5.2.5 shows the XPS spectrum of HMM-ph$Cr(CO)_3$ in the Cr 2p energy region. The $2p_{1/2}$ and $2p_{3/2}$ peaks can be observed at 586.0 and 576.5 eV, respectively, showing good agreement with those reported for $C_6H_6Cr(CO)_3$ ($2p_{1/2}$; 585.1 eV, $2p_{3/2}$; 576.1 eV) [14]. XPS investigations, thus, additionally supports the formation of the ph$Cr(CO)_3$ moieties within HMM-ph while the Cr exist as zero valent. The Cr loading of HMM-ph$Cr(CO)_3$ was determined to be 3.9 wt% as Cr metal, which shows that 15.0% of the phenylene moieties within HMM-ph were transferred into a ph$Cr(CO)_3$ complex [8]. Furthermore, the ratio of the number of CO molecules to that of Cr atoms within HMM-ph$Cr(CO)_3$ was determined to be 3.0 by chemical analyses, showing that almost all Cr atoms exist as ph$Cr(CO)_3$ complex within HMM-ph$Cr(CO)_3$.

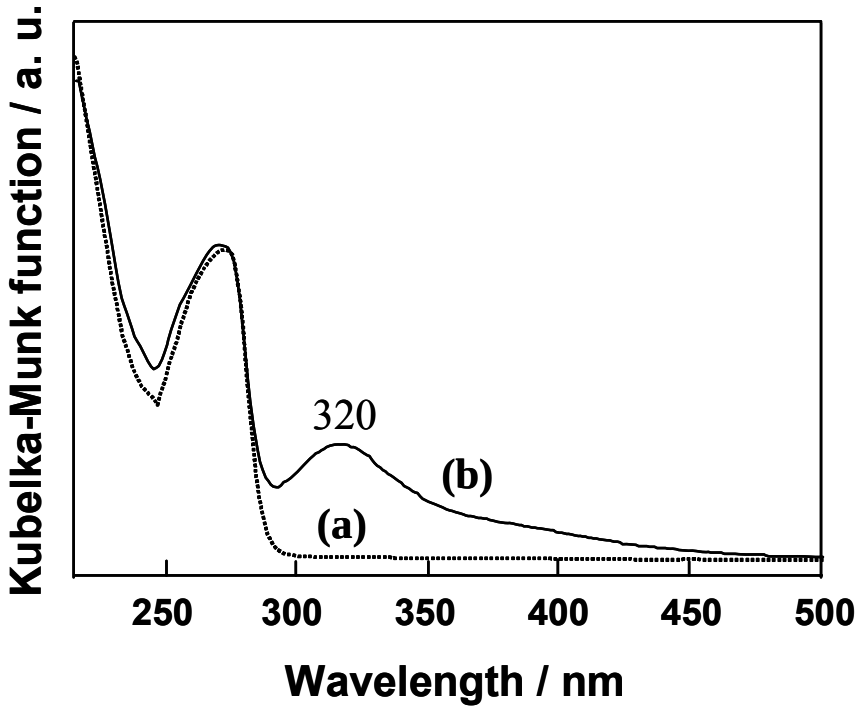

Figure 5.2.4. UV-vis spectra of (a) HMM-ph and (b) HMM-ph$Cr(CO)_3$.

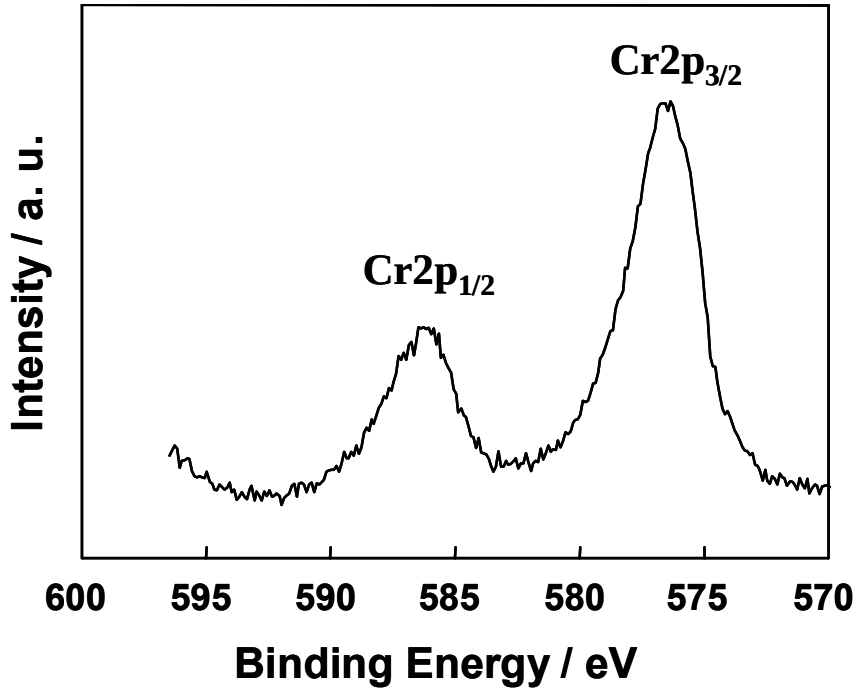

Figure 5.2.5. XPS spectrum of Cr 2p electrons excited from HMM-ph($Cr(CO)_3$.

The incorporations of $phMo(CO)_3$ and $phW(CO)_3$ complexes within the wall structures of HMM-ph were carried out by applying CVD treatments using corresponding metal carbonyls ($Mo(CO)_6$ and $W(CO)_6$). Figure 5.2.6 shows the FT-IR spectra of HMM-$phMo(CO)_3$ and HMM-$phW(CO)_3$ obtained after the CVD treatment with $M(CO)_6$ (M = Mo, W) at desired temperature. Typical FT-IR peaks due to the a1 (1981–1984 cm^{-1}) and e (1880–1920 cm^{-1}) vibrational mode of the arene-$M(CO)_3$ (M = Mo [15,16], W [16]) can be observed, showing that $phMo(CO)_3$ and $phW(CO)_3$ complexes can be also incorporated within HMM-ph through the reaction of the phenylene moieties of HMM-ph with $M(CO)_6$ (M = Mo, W). The Mo and W loading of HMM-$phMo(CO)_3$ and HMM-$phW(CO)_3$ were determined to be 1.0 wt% (as Mo metal) and 1.6 wt% (as W metal), respectively. The thermal stabilities of HMM-$phM(CO)_3$ (M = Cr, Mo, W) were also investigated by CO-TPD measurements. As shown in Fig. 5.2.7, the amount of desorbed CO increases above 473 K, passing through a maximum at temperature region between 583 K and 613 K and then decreasing at much higher temperatures. These results suggest that the $phM(CO)_3$ (M = Cr, Mo, W) complexes within HMM-ph exist stably even under thermovacuum treatment at 473 K and start to be decomposed at higher temperature. In fact, well-defined FT-IR spectra due to $phM(CO)_3$ (M = Cr, Mo, W) complexes can be observed for HMM-$phM(CO)_3$ (M=Cr, Mo, W) even after the thermovacuum treatment at 473 K (Fig. 5.2.6). These results show remarkable contrast to the desorption profiles of $Cr(CO)_6$ or $C_6H_6Cr(CO)_3$ complexes deposited on MCM-41 which are completely desorbed as low as 373 K in vacuum (Figs. 5.2.3 (a´), (b´)). Thus, it was found that the direct and stable incorporation of arene metal carbonyl complexes within highly ordered hybrid mesoporous materials could be achieved by applying simple CVD treatments.

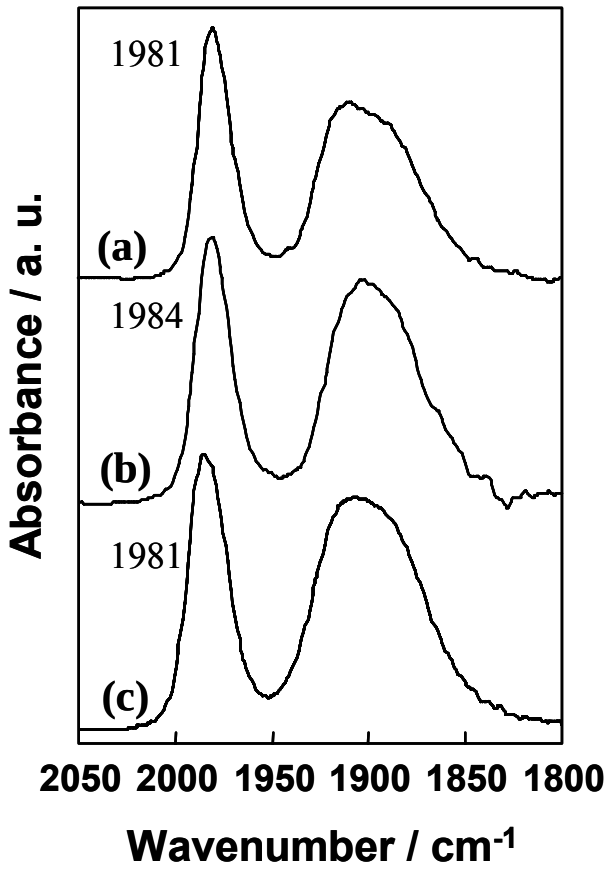

Figure 5.2.6. FT-IR spectra of (a) HMM-ph$Cr(CO)_3$, (b) HMM-ph$Mo(CO)_3$ and (c) HMM-ph$W(CO)_3$ measured after evacuation at 473 K. To obtain real spectra of Cr-compounds, the FT-IR spectrum of HMM-ph was subtracted from all observed spectra as background.

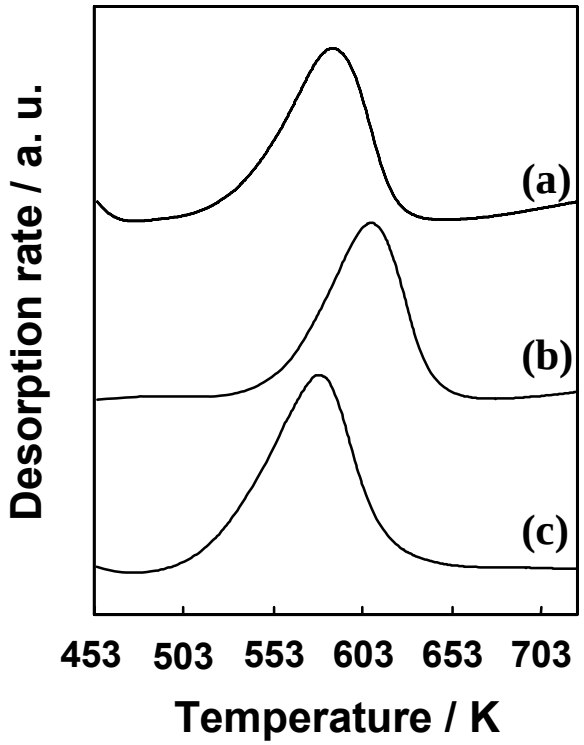

Figure 5.2.7. CO-TPD profiles of (a) HMM-phCr$(CO)_3$, (b) HMM-phMo$(CO)_3$ and (c) HMM-phW$(CO)_3$.

The HMM-biph$Cr(CO)_3$ was prepared by CVD treatment of HMM-biph with $Cr(CO)_6$ and its thermal stability was investigated. The XRD pattern of HMM-biph exhibits sharp peaks in the region of $2\theta < 5°$ due to a two-dimensional hexagonal structure as well as the additional small sharp peaks in the region of $6° < 2\theta < 40°$, showing that the periodicity of the $O_{1.5}Si\text{-}(C_6H_4)_2\text{-}SiO_{1.5}$ units exists within the wall of the mesoporous framework [5] (Fig. 5.2.8(a)). The XRD patterns were found to be almost the same before and after CVD treatment so that the structure of HMM-biph and the covalently bonded network of the $O_{1.5}Si\text{-}(C_6H_4)_2\text{-}SiO_{1.5}$ units could be retained even after CVD treatment at 398 K (Fig. 5.2.8). As shown in Fig. 5.2.9, HMM-biph$Cr(CO)_3$ exhibited typical two FT-IR bands at 1980 and 1940–1840 cm^{-1}, each corresponding to a_1 and e vibrational mode of arene-$Cr(CO)_3$ complex, respectively [16]. Furthermore, HMM-biph$Cr(CO)_3$ exhibits a long-tailed visible light absorption beyond 400 nm due to the ligand field absorption of Cr [13] (data not shown). These results show that biph$Cr(CO)_3$ complex was, thus, also prepared through the reaction of the biphenylene moieties of HMM-biph with $Cr(CO)_6$. Furthermore, it is clearly seen that these FT-IR bands due to biph$Cr(CO)_3$ complex exist stably even after thermovacuum treatment at 473 K. TPD result also showed that the complete desorption of CO from HMM-biph$Cr(CO)_3$ can be observed below 603 K (data not shown). It should be noted that the similar FT-IR spectra and CO-TPD profiles were obtained for $C_6H_6Cr(CO)_3$/MCM-41 prepared by PVD treatment for 40 min under the temperature range between 343 K and 393 K. The Cr loading of HMM-biph$Cr(CO)_3$ was determined to be 0.5 wt% as Cr metal. Thus, highly ordered HMM incorporating various arenetricarbonyl complexes have been successfully developed by a simple CVD method and their high thermal stabilities have been demonstrated. These novels HMM can be utilized in the development of unique heterogeneous catalysts since arenetricarbonyl complexes exhibit effective catalytic activity for such reactions as the hydrogenation of polyunsaturates into cis-unsaturated products [17].

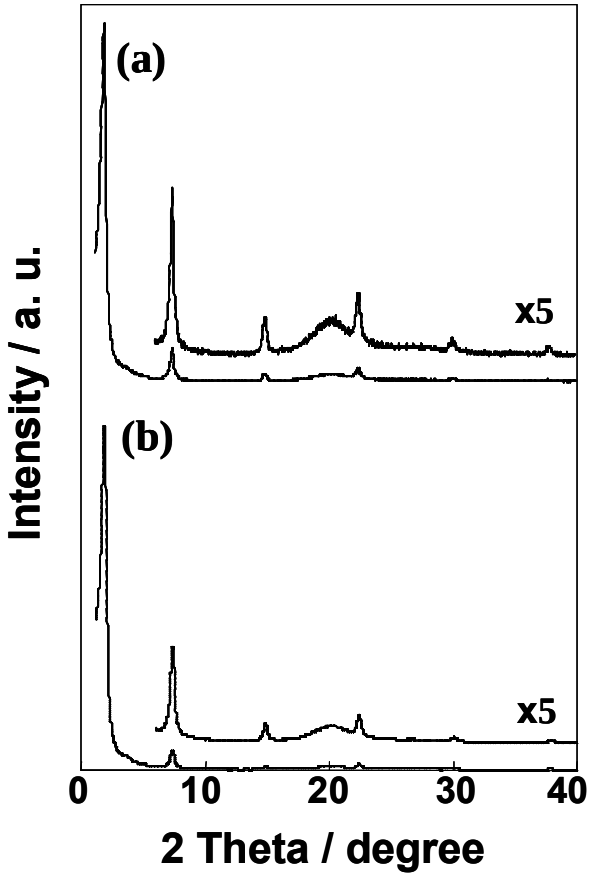

Figure 5.2.8. XRD patterns of (a) HMM-biph, (b) HMM-biphCr$(CO)_3$.

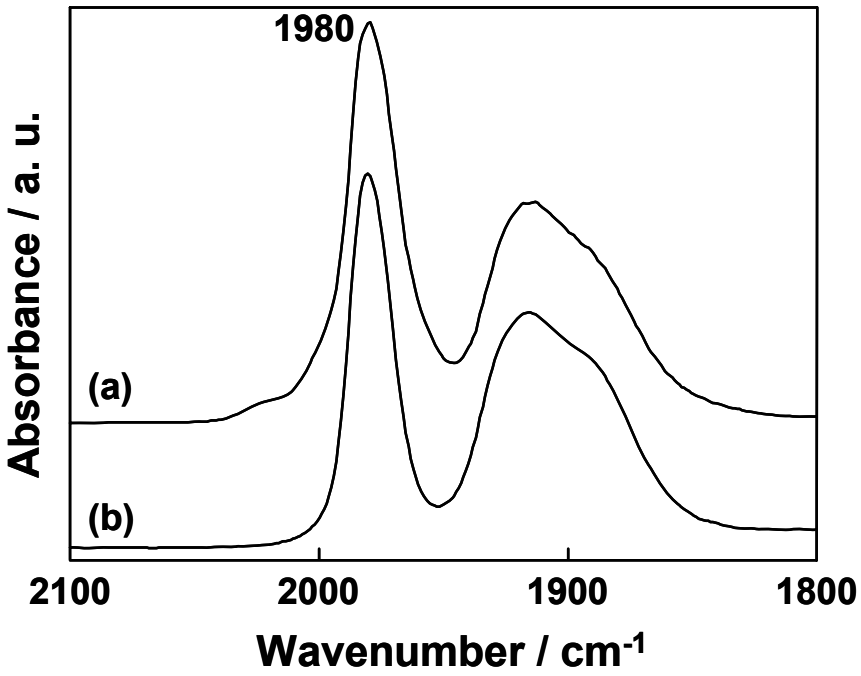

Figure 5.2.9. FT-IR spectra of HMM-biph$Cr(CO)_3$ measured (a) before and (b) after evacuation at 473 K. To obtain real spectra of Cr-compounds, the FT-IR spectrum of HMM-ph was subtracted from all observed spectra as background.

Finally, the catalytic activity of HMM-ph$M(CO)_3$ for the metathesis reaction of propylene was investigated in gas phase reaction. The metathesis reaction of propylene was hardly occurred on HMM-ph$Mo(CO)_3$ in the dark at 293 K. The HMM-ph$Mo(CO)_3$ in the presence of propylene under UV light irradiation induced the consumption of propylene and stoichiometric formation of ethane and butane even at 293 K, although HMM-ph$Cr(CO)_3$ does not exhibit any catalytic reactivities for this reaction. The turnover number for the reaction defined as the ratio of the number of consumed propylene molecules to the total number of Mo metal center included in the HMM-ph$Mo(CO)_3$ reached 13.7 after UV light irradiation, indicating that the metathesis reaction of propylene proceeded catalytically on HMM-ph$Mo(CO)_3$. After this reaction on HMM-ph$Mo(CO)_3$, the small amount of CO was also detected in gas phase. Therefore, these results suggested that the catalytic activity site is the coordinatively unsaturated Mo species formed partial desorption of CO under UV light irradiation.

The detailed characterization and reaction mechanisms of HMM-ph$M(CO)_3$ (M = Cr, Mo, W) and HMM-biph$Cr(CO)_3$, as well as their applications for heterogeneous catalysts are now underway.

5.2.4. Conclusions

Unique inorganic–organic hybrid mesoporous materials which incorporate various arene metal carbonyl complexes (ph$M(CO)_3$ (M = Cr, Mo, W) and biph$Cr(CO)_3$) within their mesoporous framework have been successfully prepared by simple CVD treatments of phenylene- or biphenylene-bridged mesoporous materials with corresponding $M(CO)_6$ (M = Cr, Mo, W). XRD investigations revealed that the mesoporous structures as well as the molecular scale periodicity were maintained even after the CVD treatment of HMM-ph and HMM-biph with $M(CO)_6$ (M = Cr, Mo, W). Thus formed arene metal complexes within inorganic–organic hybrid mesoporous materials were found to be stable even under thermovacuum treatment at 473 K,

showing remarkable contrast to the $C_6H_6Cr(CO)_3$ or $Cr(CO)_6$ complexes deposited on MCM-41 which can be easily desorbed by the evacuation treatment as low as 398 K. The metathesis reaction of propylene was catalytically proceeded on HMM-ph$Mo(CO)_3$ in heterogeneous system.

5.2.5. References

[1] S. Inagaki, S. Guan, Y. Fukushima, T. Ohsuna, O. Terasaki, *J. Am. Chem. Soc.*, **121**, 9611 (1999).

[2] B.J. Melde, B.T. Holland, C.F. Blanford, A. Stein, *Chem. Mater.*, **11**, 3302 (1999).

[3] T. Asefa, M.J. MacLachlan, N. Coombs, G.A. Ozin, *Nature*, **402**, 867 (1999).

[4] S. Inagaki, S. Guan, T. Ohsuna, O. Terasaki, *Nature*, **416**, 304 (2002).

[5] M.P. Kapoor , Q. Yang, S. Inagaki, *J. Am. Chem. Soc.*, **124**, 15176 (2002).

[6] Q. Yang, M.P. Kapoor, S. Inagaki, *J. Am. Chem. Soc.*, **124**, 9694 (2002).

[7] Q. Yang, M.P. Kapoor , N. Shirokura, M. Ohashi, S. Inagaki, J.N. Kondo, K. Domen, *J. Mater. Chem.*, **15**, 666 (2005).

[8] T. Kamegawa, T. Sakai, M. Matsuoka, M. Anpo, *J. Am. Chem. Soc.*, **127**, 16784 (2005).

[9] S.S. Kaye, J.R. Long, *J. Am. Chem. Soc.*, **130**, 806 (2008).

[10] C.F. Cheng, D.H. Park, J. Klinowski, *J. Chem. Soc., Faraday Trans.*, **93**, 193 (1997).

[11] G. Hunter , C.H. Rochester , A.G. Wilkinson, J. Paton, *J. Chem. Soc., Faraday Trans.*, **92**, 5093 (1996).

[12] K. Hamanishi, H. Shizuka, *J. Chem. Soc., Faraday Trans.*, **89**, 3007 (1993).

[13] H. Sun, Z. Chen, X. Zhou, *Inorg. Chim. Acta*, **355**, 404 (2003).

[14] S. Pignataro, A. Foffani, G. Distef ano, *Chem. Phys. Lett.*, **20**, 350 (1973).

[15] C.J. Breheny, J.M. Kelly, C. Long, S. O'Keefe, M.T. Pryce, G. Russell, M.M. W alsh, *Organometallics*, **17**, 3690 (1998).

[16] M.J. Aroney, R.M. Clarkson, R.J. Klepetko, A.F. Masters, R.K. Pierens, *J. Organomet. Chem.*, **393**, 371 (1990).

[17] R.A. Awl, E.N. Frankel, J.P. Friedrich, E.H. Pryde, *J. Am. Oil Chem. Soc.*, **55**, 577 (1978).

Chapter 6

General Conclusions

General Conclusions

In this thesis, in order to enhance the photocatalytic activity of bulk TiO_2 photocatalysts, a magnetron sputtering method has been applied to develop visible light-responsive TiO_2 photocatalysts with high performance. The photocatalytic activity of Vis-TiO_2 has been investigated by the oxidation of various organic compounds into CO_2. Furthermore, a unique photocatalytic system has been demonstrated where the visible light irradiation of a surface complex formed between benzyl alcohol and the surface hydroxyl group of the TiO_2 photocatalyst initiates the selective and efficient oxidation of benzyl alcohol into benzaldehyde. Moreover, in order to realize practical applications of TiO_2 photocatalysts, unique photoelectrochemical circuit systems have been constructed where a rod-type TiO_2 electrode and Pt electrode are connected through a silicon solar cell. The photocatalytic activity of the photoelectrochemical circuit system was examined by the decomposition of ethanethiol in water. In addition to semiconducting photocatalytic systems, single-site photocatalysts have been prepared within the framework of zeolites or mesoporous materials by various preparation methods such as hydrothermal, ion exchange and chemical vapor deposition (CVD) and applied for various highly selective photocatalytic reactions. Detailed and comprehensive characterizations of these photocatalysts were undertaken by such spectroscopic techniques as UV-vis, XAFS, XRD, XPS, SEM, TPD, FT-IR, and photoluminescence analyses. The main results of obtained from this research have been summarized according to chapter.

Chapter 2

Chapter 2 discusses the preparation of visible light-responsive TiO_2 thin films deposited on various kinds of anodized Ti-metal substrates by a radio-frequency magnetron sputtering (RF-MS) method. These Vis-TiO_2 thin film photocatalysts (Vis-TiO_2/P-Titanystar and Vis-TiO_2/N-Titanystar) showed high activity for the oxidation of

2-propanol in water under UV light irradiation while Vis-TiO_2/N-Titanystar showed higher activity than Vis-TiO_2/P-Titanystar. Furthermore, the photocatalytic activity of Vis-TiO_2/N-Titanystar was enhanced by Pt deposition using a RF-MS deposition method. The Pt-loaded Vis-TiO_2/N-Titanystar (Pt-Vis-TiO_2/N-Titanystar) acted as an efficient photocatalyst for the oxidation of methanol vapor under UV light irradiation even under a flow system. Moreover, it was found that Pt-Vis-TiO_2/N-Titanystar is an effective photocatalyst for the oxidation of various organic compounds in the gas phase or ammonia gas even under visible light irradiation ($\lambda > 420$ nm) at 293 K.

Chapter 3

Chapter 3 discusses the construction of photoelectrochemical circuit systems consisting of a rod-type TiO_2 electrode and a Pt electrode connected through a silicon solar cell and their application for the decomposition of methanethiol in water.

Chapter 3.1 focuses on the effect of the external bias as well as the calcination temperature of the rod-type TiO_2 electrode on the oxidation rate of ethanethiol. The photoelectrochemical circuit system efficiently oxidized ethanethiol in water into CO_2, while the reaction rate strongly depended on the calcination temperature of the rod-type TiO_2 electrode. It was also found that a negative bias applied to the rod-type TiO_2 electrode by a silicon solar cell enhances the oxidation rate of ethanethiol in water.

Chapter 3.2 focuses on the effect of various calcination treatments of the rod-type TiO_2 electrode on the photocatalytic activity. Calcination treatment in NH_3 at 773 K was particularly effective in increasing the photoelectrochemical performance and photocatalytic activity. Spectroscopic investigations have revealed that a dense and thick stoichiometric TiO_2 layer was formed on TE calcined in NH_3 at 773 K, showing the highest activity for the decomposition of ethanethiol.

Chapter 4

Chapter 4 deals with the selective photocatalytic oxidation of benzyl alcohol into

benzaldehyde with high efficiency and selectivity on a TiO_2 photocatalyst suspended in acetonitrile solution in the presence of O_2 under visible light irradiation. In order to elucidate the surface interaction between TiO_2 and benzyl alcohol, the effects of the calcination temperature and HF treatment of TiO_2 on the selective photocatalytic oxidation were investigated. It was confirmed that a surface complex formed by the interaction of benzyl alcohol with both the coordinately unsaturated Ti sites and surface OH groups absorb visible light, resulting in the selective photocatalytic oxidation of benzyl alcohol into benzaldehyde.

Chapter 5

Chapter 5 introduces the preparation of various zeolites or silicious mesoporous materials containing highly dispersed single-site metal oxides or organometalcarbonyl complexes as photocatalysts by various methods such as hydrothermal, ion-exchange or ligand exchange and their application for highly selective photocatalytic reactions.

Chapter 5.1 deals with the local structures of the transition metal oxides (Ti, V, Mo, Cr) incorporated into zeolite framework structures. Various in situ spectroscopic techniques such as ESR, UV-Vis, photoluminescence and XAFS (XANES and EXAFS) have revealed that metal oxide catalysts (Ti, V, Mo, Cr) which are incorporated into the frameworks or cavities of various zeolites exist in highly dispersed tetrahedral coordination states and act as efficient photocatalysts for the decomposition of NO into N_2 and O_2 as well as the reduction of CO_2 with H_2O to produce CH_4 and CH_3OH. Photoluminescence investigations revealed that the efficient interaction of the charge-transfer photo-excited complexes of these oxides, $(Me^{(n-1)+}–O^-)^*$, i.e., an electron-hole pair state with such reactant molecules as NO, CO_2 and H_2O plays a significant role in the photocatalytic reactions.

Chapter 5.2 discusses the preparation and characterization of arenetricarbonyl complexes incorporated within the framework structure of phenylene- or biphenylene-

bridged hybrid mesoporous materials (HMM-ph or HMM-biph) by chemical vapor deposition (CVD) treatment. Simple CVD treatment of $M(CO)_6$ (M = Cr, Mo, W) onto phenylene- or biphenylene-bridged organosilica mesoporous materials (HMM-ph, HMM-biph) led to the efficient formation of $C_6H_4M(CO)_3$ and $(C_6H_4)_2M(CO)_3$ complexes, respectively, which are directly fixed and incorporated within the framework structure of HMM-ph and HMM-biph having molecularscale periodicity in their pore walls. FT-IR investigations revealed that thus formed $C_6H_4M(CO)_3$ or $(C_6H_4)_2M(CO)_3$ complexes are thermally stable even under thermovacuum treatment at 473 K. It was also found that UV irradiation of HMM-ph or HMM-biph containing these organometalcarbonyl complexes initiates the metathesis reaction of propylene into ethylene and butadiene even at 293 K.

Chapter 6

The results and conclusions obtained in the various investigations covered in this thesis have been summarized in this final chapter.

ACKNOWLEDGEMENTS

The author, Tae-Ho Kim, would like to express his sincere gratitude to Professor Masakazu Anpo of the Department of Applied Chemistry, Graduate School of Engineering, Osaka Prefecture University, for his warm encouragement and invaluable instruction during the course of this study.

Sincere thanks are also extended to Professor Hiroshi Inoue and Professor Hiroshi Bandow of Osaka Prefecture University for their critical reading of the thesis and for their many useful suggestions leading to its improvement.

The author also wishes to thank Associate Professor Masaya Matsuoka and Assistant Professor Masato Takeuchi of Osaka Prefecture University, Professor Soo-Wohn Lee of the Sunmoon University, Lecturer Shinya Higashimoto of Osaka Institute of Technology, Assistant Professor Takashi Kamegawa of Osaka University for their helpful and stimulating suggestions and discussions during the present research. Also, sincere thanks are extended to Mrs. Sumiyo Ono for her helpful assistance in the English editing of the text.

Deep thanks are also extended to the author's colleagues, Mr. Masakazu Saito, Mr. Kazuhiro Uchihara, Ms. Jun Morishima, Mr. Motoki Kondo, Mr. Shohei Fukumoto, Mr. Masato Hozumi, Mr. Yusuke Sakai, Mr. Masaki Nakagawa, Mr. Tetsuji Watanabe, Mr. Kozo Ueda, Mr. Ryohei Tode for their help and experimental assistance.

Finally, the author would like to express his sincere gratitude to his parents, wife and son for their kind understanding and strong encouragement towards his research work.

Tae-Ho Kim
Sakai, Osaka
February, 2010

LIST OF PUBLICATIONS

1. Photocatalytic Oxidation of Ethanethiol on a Photoelectrochemical Circuit System Consisting of a Rod-Type TiO_2 Electrode and Silicon Solar Cell

T.-H. Kim, M. Saito, M. Matsuoka, S. Tsukada, K. Wada, M. Anpo, *Res. Chem. Intermed.*, **35**, 633-642 (2009).

2. The Design of Ti-,V-, Cr-Oxide Single-Site Catalysts within Zeolite Frameworks and their Photocatalytic Reactivity for the Decomposition of Undesirable Molecules –The role of their excited states and reaction mechanisms

M. Anpo, T.-H. Kim, M. Matsuoka, *Catal. Today*, **142**, 114-124 (2009).

3. Incorporation of Arene Metal Carbonyl Complexes within Inorganic-Organic Hybrid Mesoporous Materials by CVD Method

M. Matsuoka, T. Kamegawa, T.-H. Kim, T. Sakai, M. Anpo, *J. Nanosci. Nanotechnol.*, **10**, 314-318 (2010).

4. Effect of Surface Treatment on the Selective Photocatalytic Oxidation of Benzyl Alcohol into Benzaldehyde by O_2 on TiO_2 under Visible Light

S. Higashimoto, K. Okada, T. Morisugi, A. Nakagawa, M. Azuma, H. Ohue, T.-H. Kim, M. Matsuoka, M. Anpo, *Top. Catal.*, in press, (2010).

5. The Effect of Various Calcination Treatments on the Photocatalytic Activity of Rod-Type TiO_2 Electrode for the Oxidation of Ethanethiol

T.-H. Kim, M. Saito, M. Matsuoka, S. Tsukada, K. Wada, M. Anpo, *Submitted to Catal. Lett.*, (2010).

6. The Effect of Photocatalytic Activity of Visible Light-responsive TiO_2 Thin Films Photocatalysts on the Various Substrates Prepared by a RF Magnetron Sputtering Method

T.-H. Kim, M. Kitano, T. Kamegawa, Y. Ito, M. Takeuchi, M. Matsuoka, M. Anpo, *Submitted to Res. Chem. Intermed.*, (2010).

7. Investigations on the Reaction Mechanism of Photoelectrochemical Circuit System Consisting of a Rod-Type TiO_2 Electrode and Silicon Solar Cell

T.-H. Kim, M. Saito, M. Matsuoka, S. Tsukada, K. Wada, M. Anpo, *Submitted to Res. Chem. Intermed.*, (2010).

8. The Effect of Microwave Furnace Heating on the Superhydrophilicity of Visible Light-responsive TiO_2 Thin Films Prepared by an RF Magnetron Sputtering Method

T.-H. Kim, M. Matsuoka, M. Takeuchi, T. Mochizuka, M. Anpo, *Submitted to Res. Chem. Intermed.*, (2010).